MAGNETICALLY CHANNELLED FLOWS IN STELLAR SYSTEMS

A thesis submitted

for the degree of

Doctor of Philosophy

by

Kevin Pearson

Astronomy Group

Department of Physics and Astronomy

University of Leicester

January 1997

UMI Number: U084873

UMI®

Dissertation Publishing

UMI U084873

ProQuest®

Abstract

This thesis discusses the interaction of stellar magnetic fields with circumstellar material in a variety of situations. Chapter 2 examines models of young stellar objects where accretion from the surrounding disc is controlled by magnetic loop structures on the star. The models produce outflows at early times which are consistent with those observed for young objects and the resultant torque on the star spins it down on a timescale also consistent with observations. Chapter 3 presents models examining the consequences of the magnetic field of the secondary star in Cataclysmic Variables (CVs) for the outburst behaviour of dwarf novae. Resonance phenomena are identified and observational tests suggested along with upper limits for the magnetic fields of the secondaries in SU UMa and U Gem systems. Chapters 4 and 5 examine the general angular momentum evolution of CVs. Simulations of magnetic braking are produced which describe the evolution in different situations. The proposal of reduced magnetic braking in polar systems is examined. Simulations are carried out which suggest that the addition of a strongly magnetic primary actually increases the rate of angular momentum loss from the binary orbit.

Acknowledgments

I would like to thank my supervisor Andrew King for keeping me on the (academic) straight and narrow path during my 3 years to finish on time. I would also like to thank Graham Wynn for sparing time for almost daily arguments about the methodology and technical aspects of the HyDisc simulations and for occasionally letting me win some ! I am eternally grateful to my parents for all the support they have given me without which I wouldn't have even got near to starting a Ph.D. Acknowledgements must also be paid to the inhabitants of the Underpass whose levity prevented the seemingly inevitable insanity of impending thesis deadlines.

Contents

Chapter 1

Introduction

Magnetic fields are important to the structure and evolution of stars throughout their lifetimes. In the early formation phase the magnetic fields play an important role in removing angular momentum from the collapsing gas cloud out of which the star will form and in regulating the accretion of material by the central protostar. Magnetic fields are also thought to be implicated in the production of the jets and molecular outflows observed in these systems. In chapter 2 we shall consider a mechanism whereby a magnetic loop structure acts to bring the accretion phase to an end and also gives rise to the molecular outflows.

During its main sequence lifetime a star may exhibit a variety of phenomena associated with stellar activity. Taking the sun as a typical example of a main sequence star we observe a bewildering array of magnetic phenomena such as sunspots, coronal loops, prominences and flares. A star may also have its rotation slowed by magnetic braking. In a close binary system such as a Cataclysmic Variable (CV), consisting of a white dwarf (WD) accreting material from a late type main sequence companion, this braking can act to remove angular momentum from the stellar orbits causing the period to shorten. This magnetic field is also important in locking the 'polar' sub-class of CVs in synchronous rotation. In chapter 3 we shall investigate the effect of the secondary's magnetic field on the behaviour of the dwarf nova group of CVs.

When nuclear burning has ceased a star will usually end its life as a neutron star (NS) or WD depending on its mass. Magnetic WDs can have important effects on the accretion processes which occur in CVs. In non-magnetic systems, we shall see that an accretion disc of material forms around the WD. A strong magnetic field can prevent the formation of such a disc and lead to accretion occurring directly onto the WD close to the magnetic pole in strongly magnetic systems such as the polars. In chapters 4 and 5 we shall investigate the effect the magnetic fields of both stars in CVs have on the braking mechanism and consequent evolution of CVs from detached systems to synchronously locked polars. It is also possible for a truncated disc to be formed where the magnetic field is only strong enough to dominate the accretion stream close to the WD. In a NS a strong magnetic field can give rise to beamed radio signals and the star is observed as a pulsar. Neutron stars are the compact objects accreting material from a main sequence companion in low-mass X-ray binary systems (LMXBs) where the neutron star is analogous to the WD in CVs.

Accretion is a major source of energy in a variety of astrophysical situations. This mechanism, in which a central object liberates the potential energy of infalling material, is known to power many types of interacting binary systems and is also believed to be the source of the prodigious luminosity of active galactic nuclei (AGN). As material falls in towards the accreting object its gravitational potential energy is converted to kinetic. As the material settles onto the massive object the kinetic energy is released, usually in the form of electromagnetic radiation. This radiation can be a useful tool for determining the underlying details of the accretion mechanism and also the nature of the accreting object.

Knowledge of the physics of accretion is also important to the understanding of star formation. The details of our current understanding of this process are discussed in section 1.1 but, clearly, understanding how material can build up on a central object will have definite implications for star formation theory.

The potential energy released by an object of mass m falling (from infinity) on to

an accreting object of mass M and radius R is

$$E = \frac{GMm}{R} \qquad (1.1)$$

Hence, if the object is accreting material at a rate $\dot{M}$ the accretion luminosity is given by

$$L_{\text{acc}} = \frac{GM\dot{M}}{R}, \qquad (1.2)$$

assuming that all of the initial potential energy is finally released as electromagnetic radiation. It is clear from (1.2) that the effectiveness of accretion as an energy source is dependent upon the ratio $\frac{M}{R}$. The larger this ratio the greater the amount of energy that may be extracted for a given $\dot{M}$. For this reason, the most important situations in which accretion needs to be considered as an energy source are those where the central object is compact, *i.e.* either a white dwarf, a neutron star or a black hole.

The material accreted by a central object rarely conforms to the radial infall scenario tacitly assumed above. Often the material has sufficient angular momentum that its orbit around the central object avoids impact upon it. If sufficient material is orbiting the object, dissipation induces the formation of an accretion disc. Disc formation in a close binary system will be discussed in more detail in section 1.2.2 and disc evolution will be described in section 1.3. Anticipating the result that fluid elements in such a disc exhibit approximately Keplerian orbits we can calculate the disc luminosity. The binding energy of a Keplerian orbit just above the stellar surface is

$$E_{\text{grav}} = \frac{GMm}{2R}. \qquad (1.3)$$

Since the material initially has negligible binding energy it follows that, if the disc is in steady state (*i.e.* the mass lost through the inner edge of the disc is replaced by material added at the outer edge), the total luminosity of the disc is

$$L_{\text{disc}} = \frac{GM\dot{M}}{2R} = \frac{L_{\text{acc}}}{2} \qquad (1.4)$$

The remaining luminosity (the difference between (1.2) and (1.4)) must be released in some kind of boundary layer close to the star where the angular velocity decreases

from Keplerian to match that of the central object. An accretion disc is thus an efficient mechanism for extracting half the accretion energy over an extended region away from the surface of the accreting object.

Another consequence of the Keplerian motion of disc elements is in spin up of the accreting object. Since the material in the disc is orbiting much faster than the rotation rate of the central object (it would otherwise be on the verge of breakup) it will exert a torque on the accretor which attempts to bring it up to the Keplerian rotation rate at its surface.

1.1 Young Stars: T Tauris

In a series of papers Joy(1942, 1945 & 1949) reported the discovery of faint late-type stars in the Taurus-Auriga dark cloud with "emission lines resembling the solar chromosphere". They were associated with nebulae and were irregular and large amplitude variables. He named these stars after the brightest member of group, T Tauri. Ambartsumian (1947) discovered that these stars occurred in groups (T-associations) often near groups of OB stars (O-associations) and suggested that these were the low mass counterparts of the high-mass (and hence young) OB stars. Further evidence for this hypothesis came from Herbig (1977) who found that the radial velocities of a sample of 50 T Tauri stars in the Taurus Auriga cloud are consistent with the associated molecular cloud. This implies that some kinetic interaction must exist between the cloud and the stars and suggests that the stars were formed out of the cloud.

The criteria used to define T Tauri stars, whether the standard definition of Herbig (1962) or a more recent refinement (Bastian *et al.* 1983), are based largely on the optical spectra. However, modern astronomy has available to it a variety of observational windows and some properties that are common to T Tauri stars at these wavelengths are exhibited by stars which do not fulfil the optical criteria. Sources matching the Herbig (1962) criteria and which were discovered by H_α surveys are

classified as Classical T Tauri stars (CTTs). Sources discovered at other wavelengths but with an optical counterpart showing features typical of pre-main sequence stars are termed variously Weak-line T Tauri (WTT), naked T Tauri or post-T Tauri stars. For this reason the term T Tauri star is now reserved for *optically* observed objects and the term young stellar object (Strom 1972) is used to describe all young, pre-main sequence or newly forming stars.

1.1.1 Young Stellar Objects

Young stellar objects (YSOs) are classified according to their infrared spectra. In particular the parameter $\alpha = -\frac{d \log \nu F_\nu}{d \log \nu}$ evaluated longward of 2.2 μm is used.

Class I These sources have $\alpha > 0$ and a spectral energy distribution (SED) broader than a blackbody spectrum. They are almost invariably sources deeply embedded in molecular clouds with no optical counterpart.

Class II This class of sources also have an SED broader than a single blackbody but show $\alpha < 0$. There is a significant IR excess and also a UV excess described as 'veiling' of the absorption lines at the blue end of the spectrum. They are often visible optically as T Tauri stars and are generally less deeply embedded in molecular clouds.

Class III These objects have $\alpha < 0$ and have a spectrum close to that of a single-temperature black body with no IR excess. Optically these stars would be WTTs.

Given the relative density distribution through the molecular cloud of the classes it is thought that these also describe an evolutionary sequence. This will be discussed in section 1.1.2.

Another phenomenon common to YSOs but not mentioned previously is that of outflows. These fall into two classes: the *jets* which are well collimated and visible
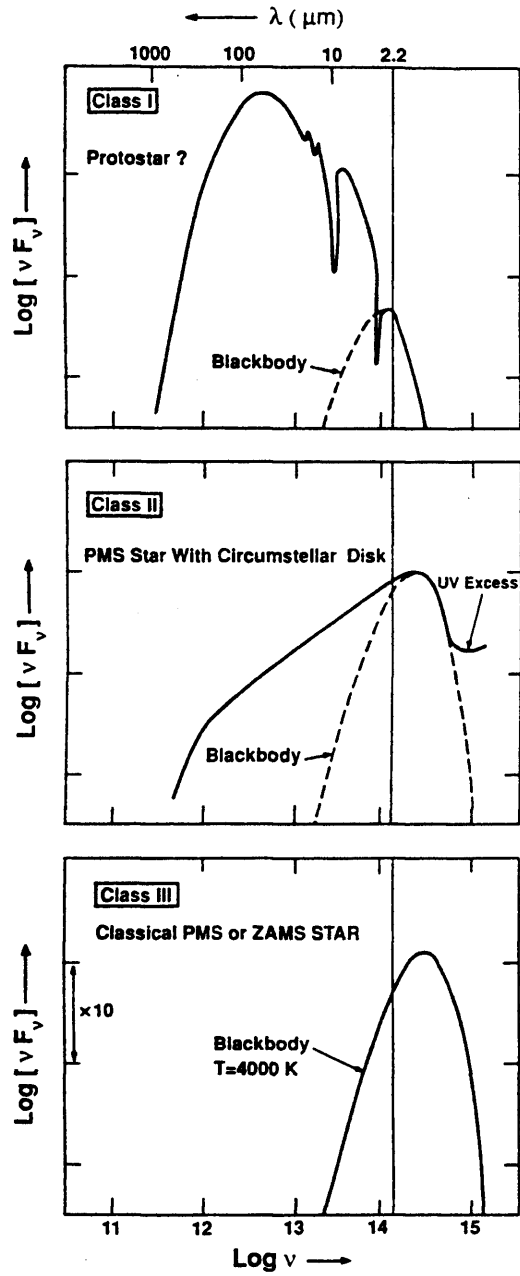
Figure 1.1: Typical spectra for the three classes of Young Stellar Object from Lada (1991).

in the optical and the *molecular outflows* which are more poorly collimated and detected by radio observations. The jets carry typical mass loss rates of $\sim$ (0.05–2) $\times$ 10^{-8} $M_{\odot}$ y^{-1} (Mundt, Brugel & Bührke 1987) with velocities of 100–300 km s^{-1} whilst the molecular outflows have higher mass loss rates of $\sim$ 10^{-7} $M_{\odot}$ y^{-1} (Lada 1985) at typical velocities of 10–30 km s^{-1}. The similarity between the momentum in both types of outflow has led to the suggestion that the jets and molecular outflows might be intimately connected with perhaps the jets driving the molecular outflows (Bence & Padman 1996). These outflows are typical of Class I & II YSOs.

1.1.2 The Formation of an Isolated Low-Mass Star

By counting the numbers of objects in each of the YSO classes described above it is possible (assuming that they do indeed describe an evolutionary sequence) to determine the amount of time spent in each class. From studies of the Taurus region Kenyon *et al.* (1990) determined the embedded phase lasts 1–2 $\times$ 10^5 y whilst from the ρ Ophiuchi cloud Wilking, Lada & Young (1989) determined it to last for 1–4 $\times$ 10^5 y. The following T Tauri phase lasts 2–3 $\times$ 10^6 y (Bodenheimer 1992). These figures are subject to uncertainty, however, because the surveys are probably incomplete.

Examining the specific angular momentum of objects in Table 1.1 we see that any theory of star formation also needs to explain how angular momentum is removed throughout the evolution.

The primary criterion for the formation of a star is that the self-gravity of a region of the cloud should be enough to overcome the gas pressure and any rotational and magnetic effects supporting it. This leads to the concept of the Jeans mass, which is the minimum mass a cloud of given density and temperature must have in order to be unstable against gravitational collapse. It can be shown that in regions where

Object	$\frac{J}{M}$ (cm^2 s^{-1})
Molecular cloud ($\sim$ 1 pc)	10^{23}
Molecular cloud core ($\sim$ 0.1 pc)	10^{21}
Jupiter (orbit)	10^{20}
T Tauri star	5×10^{17}
Present Sun	10^{15}

Table 1.1: Characteristic values of specific angular momentum adapted from Boden-heimer (1992).

supporting factors are rotation and gas pressure the Jeans mass is given by

$$M_{\rm J} = \left(\frac{\frac{R_g T}{\mu} + 0.2\Omega^2 R^2}{0.4G} \right)^{\frac{3}{2}} \left(\frac{4}{3}\pi\rho \right)^{-\frac{1}{2}} \tag{1.5}$$

where R_g is the gas constant, T is the temperature of the gas, μ is the mean molecular weight, Ω is the angular velocity of the rotation, R is the radius of the assumed spherical region under consideration, ρ is the density and G is the gravitational constant. If the main support for the cloud region is a uniform magnetic field then the magnetic Jeans mass is

$$M_{\rm J} = \frac{BR^2}{\sqrt{3.6G}} \tag{1.6}$$

where B is the strength of the magnetic field in Gauss (Bodenheimer 1992).

For typical interstellar values ($T \approx 100$ K, $n \approx 10$ cm^{-3} and $B \approx 3$ μG) the thermal Jeans mass is $10^4 M_\odot$ and the magnetic Jeans mass is $\sim 2 \times 10^4 M_\odot$

Combining the relative distribution of the classes of YSO with their spectral characteristics, the times determined above and the angular momentum and Jeans mass considerations we arrive at the modern picture of the processes involved in the formation of an isolated, low-mass star as described by Bodenheimer (1992).

1. Starting from typical conditions for a molecular cloud the frozen-in magnetic

field transfers much of the angular momentum out of the cloud to the surrounding inter-stellar medium in which it is anchored on a timescale $t_{am} \sim 5 \times 10^6 y$.

2. The cloud cools and material becomes less and less tightly coupled to the field as the degree of ionization drops. Neutral particles are able to drift inwards to form a molecular cloud core on a timescale $t_{diff} \sim 10^7$ y. The density in this region rises to the point that it is observable in NH_3.

3. The magnetic field becomes unimportant in the now largely neutral core and the mass in the dense region exceeds the thermal Jeans mass. The region collapses conserving angular momentum on close to the free-fall timescale $t_{ff} \sim 10^5$–10^6 y.

4. A stellar core and a disc form as material with higher angular momentum approaches equilibrium. The core and disc are surrounded by an optically thick infalling envelope. The protostar becomes an infrared source and is observable as a Class I YSO.

5. As the protostar accretes a bipolar outflow begins, becoming visible along the rotational poles.

6. Infall stops either due to the bipolar flow or because the available material is exhausted, and the core emerges as a visible T Tauri Class II YSO. The disc gives rise to an infra-red excess. The star continues to accrete slowly and contracts towards the main sequence (MS).

7. Disc evolution occurs and mass moves inwards as angular momentum is transferred outwards. The disc is depleted either through accretion by the central star or potentially by proto-planets or swept away by the outflow. The star is visible as a Class III YSO as it approaches the MS.

This evolution is summarised in figure 1.2.

The reason for considering the formation of low and high-mass stars separately is clear if we consider two timescales from Lada (1991). The free-fall timescale for a
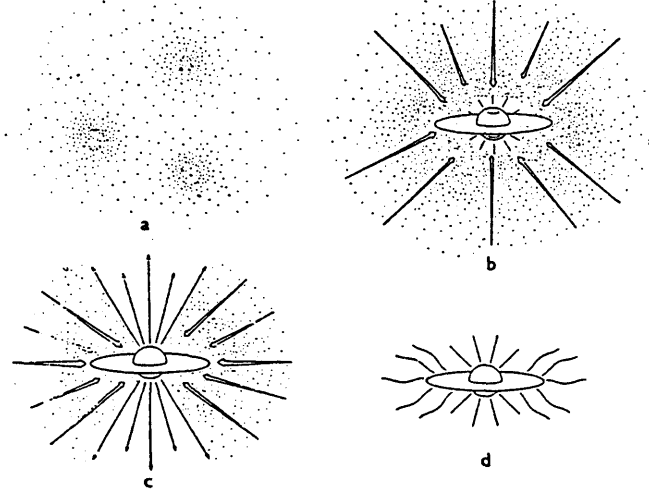
Figure 1.2: Stages in the formation of an isolated, low-mass star from Shu, Adams & Lizano (1987).

molecular cloud can be shown to be

$$t_{\mathrm{ff}} = \sqrt{\frac{3\pi}{32 G \rho}} \sim 4 \times 10^5 \text{ y} \qquad (1.7)$$

for number densities $\sim 10^4$ cm^{-3} typical of a cloud core. The timescale for evolution once a stellar object has formed is

$$t_{\mathrm{KH}} \approx \frac{G M_*^2}{R_* L_*} \qquad \sim 10^4 \text{ y} \qquad \text{for } M_* = 50 M_\odot \qquad (1.8)$$

$$\sim 3 \times 10^7 \text{ y} \quad \text{for } M_* = M_\odot \qquad (1.9)$$

This shows that for high mass stars the star begins nuclear burning and settles on to the main sequence before the termination of cloud infall. Low-mass stars are also less disruptive to the environment from which they form, whereas any theory of the formation of high-mass stars would need to include interactions with other stars forming in the same region.

1.2 Cataclysmic Variables

1.2.1 Binary systems

It is believed that the majority of stars belong to binary systems. Binary systems are important since they reveal more of their physical characteristics, particularly their dimensions, than other astronomical objects. It is often possible to determine the relative masses of the stars in such systems, and if the system eclipses it is possible to determine the absolute masses and dimensions of the binary. The separation of the stars a is fixed by the orbital period P, which is usually directly observable via time-resolved spectroscopy or photometry, using Kepler's law

$$4\pi^2 a^3 = G(M_1 + M_2)M_\odot P^2 \qquad (1.10)$$

where the masses of the two stars M_1 and M_2 are given as multiples of the solar mass.

The importance of accretion in binary star systems becomes more apparent when their evolution is considered. In particular, we shall consider a scenario which gives rise to the formation of a CV. Since the components of a binary are likely to have different masses they will evolve at different rates as the more massive (primary) star uses up its hydrogen fuel more quickly. As this star goes through its red giant phase its tenuous outer layers may well engulf the companion star, causing the period of the binary to shorten and helping to expel the outer envelope as the star eventually ends as a white dwarf. This process is termed common envelope evolution. It is possible for the orbital period to shorten further through angular momentum losses driven by winds from the companion star or gravitational radiation. Ultimately the period may become so short that the white dwarf star is able to strip material gravitationally from the envelope of the companion star. This process is called Roche-lobe overflow.

An alternative mode of accretion in binary systems is via a wind. If during some stage of evolution one of the stars undergoes mass-loss in the form of a wind then

it is possible for accretion to occur if the companion captures some of the expelled material.

1.2.2 Structure

Cataclysmic Variables (CVs) are a class of binary systems consisting of a white dwarf primary which is accreting material from (usually) a late-type, main sequence companion via Roche-lobe overflow. The eponymous Edouard Roche was a 19th century French mathematician who first considered the problem of a test particle moving in the potential of two massive bodies in orbit about each other in the context of the disruption of planetary satellites. The problem is also known as the restricted three body problem as the third body, the test particle, is assumed to have negligible mass. The orbits are assumed to be circular, which in the case of a CV is usually a very good approximation as the timescale for circularization due to tidal effects is much shorter than the mass transfer timescale. The analysis also assumes that the bodies can be treated as point masses which is also a good approximation for binary stars.

Any gas flow in the region of the two stars is governed by the Euler equation

$$\rho \frac{\partial \mathbf{v}}{\partial t} + \rho \mathbf{v} . \bigtriangledown \mathbf{v} = - \bigtriangledown P + \mathbf{f} \tag{1.11}$$

where ρ is the density, P is the gas pressure, $\mathbf{v}$ is the velocity field, and $\mathbf{f}$ the external force density. It is convenient to write this equation in a frame rotating with the binary so that the stars are stationary. In this frame (1.11) becomes

$$\frac{\partial \mathbf{v}}{\partial t} + (\mathbf{v} . \bigtriangledown) \mathbf{v} = - \bigtriangledown \Phi_R - 2\omega \wedge \mathbf{v} - \frac{1}{\rho} \bigtriangledown P \tag{1.12}$$

where $\omega = \frac{2\pi}{P_{orb}}$ is the orbital frequency. The term $-2\omega \wedge \mathbf{v}$ is the Coriolis force per unit mass and $- \bigtriangledown \Phi_R$ includes the effect of both gravitational and centrifugal forces. The function Φ_R, known as the Roche potential, is thus given by

$$\Phi_R(\mathbf{r}) = - \frac{GM_1 M_\odot}{|\mathbf{r} - \mathbf{r_1}|} - \frac{GM_2 M_\odot}{|\mathbf{r} - \mathbf{r_2}|} - \frac{1}{2}(\omega \wedge \mathbf{r})^2 \tag{1.13}$$

where r_1 and r_2 are the position vectors of the centres of the two stars.

It is extremely useful to consider the equipotential surfaces of Φ_R and particularly their sections in the orbital plane. These are plotted in figure 1.3. However, it should be recalled that not all of the forces which act on the gas, in particular the Coriolis force, are included in Φ_R. The shapes of its equipotentials are determined by the mass ratio $q = M_2/M_1$, although the same general features are always present. Insight can be gained by considering the motion of a test particle in the Roche potential at various positions in figure 1.3. When the particle is at a large distance from the binary ($r \gg a$), the equipotentials are seen to be circular, and the potential corresponds to that of a point mass at the centre of mass of the system. There are also circular sections close to the centres of the two stars. In these positions the gravitational attraction of the nearer star dominates the potential. Moving outwards from the centres of the stars the equipotentials become more and more distorted from circular. The last equipotential surrounding each star separately forms a figure of eight shape known as the Roche lobes. In 3-dimensions these lobes have a dumbbell shape. The point at which the two lobes join is known as the inner Lagrangian point L_1. The two lobes can be thought of as two deep potential valleys which communicate via a saddle point at L_1. A test mass around L_1 will find it easier to cross from one Roche lobe to the other rather than travel up the potential gradient and escape from the binary altogether.

In a cataclysmic variable it is believed that the dwarf secondary fills its Roche lobe and is consequently distorted from spherical. Perturbations in the envelope of the secondary near to L_1 will cause material to flow into the Roche lobe of the primary. Such perturbations are always present provided *e.g.* by pressure forces. This process of mass transfer will continue as long as the secondary remains in contact with the Roche lobe.

The complex form of Φ_R and the distorted shape of the Roche lobes means that an accurate calculation of an effective radius of the secondary star R_2 needs to be carried out numerically. Several, analytic forms for R_2 exist, however, which produce
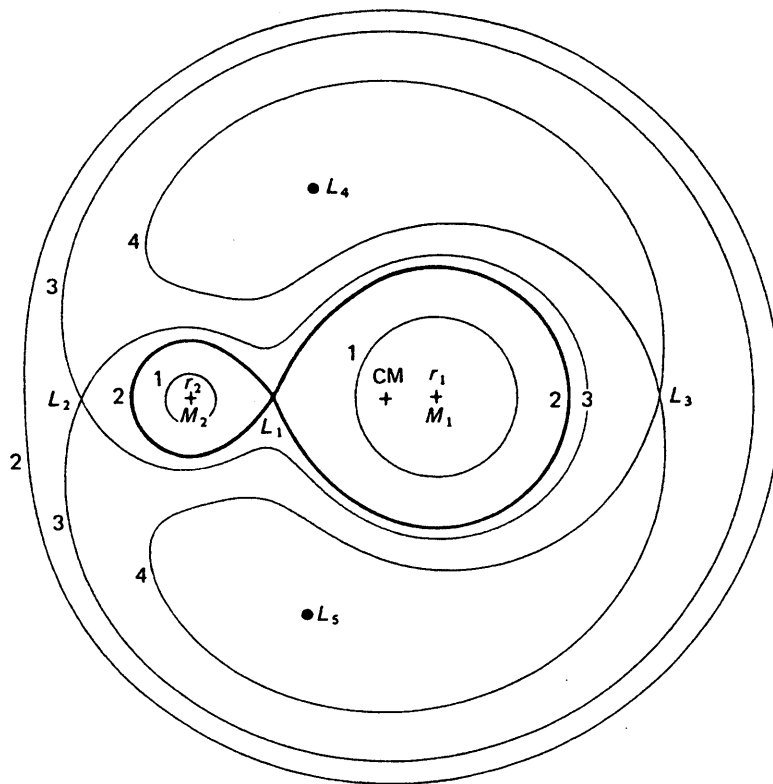
Figure 1.3: Roche equipotentials in the plane from Frank, King & Raine (1992).

good fits. A useful result can be obtained by combining the formula of Paczynski (1971)

$$\frac{R_2}{a} = 0.462 \left(\frac{q}{1+q} \right)^{1/3}, \quad q \lesssim 0.8 \tag{1.14}$$

with (1.10) to give the mean density of a Roche lobe filling star

$$\bar{\rho} = \frac{3M_2}{4\pi R_2^3} \simeq 1.15 \times 10^5 P_{\mathrm{hr}}^{-2} \ \mathrm{kg \ m^{-3}}. \tag{1.15}$$

If we assume that the star has a similar structure to an isolated main sequence star of low mass we can incorporate the homology relation $R_2/R_\odot \simeq M_2$ then we can derive an expression for the mass of the secondary star purely in terms of the binary period

$$M_2 \simeq 0.11 P_{\mathrm{hr}}. \tag{1.16}$$

The fate of the material once it has traversed the L_1 point depends upon the strength of the magnetic field of the WD primary. We will consider first the situation where the primary does not possess a magnetic field strong enough to influence the flow of transferred material.

Accretion Disc Formation

In determining the trajectory of the gas after it leaves L_1 we recall that, at L_1, the gas was orbiting with the rest of the secondary at the binary frequency $\omega = \frac{2\pi}{P_{\mathrm{orb}}}$, and that pressure forces were the cause of the mass transfer. Hence, if we split the velocity of the gas into its components perpendicular to $(v_\perp)$ and parallel to $(v_\parallel)$ the line of centres we have

$$v_\perp \sim b\omega \tag{1.17}$$

and

$$v_\parallel \gtrsim c_s \tag{1.18}$$

where b is the distance of the L_1 point from the primary and c_s is the sound speed in the envelope of the secondary. If we apply the approximate formula of Plavec and Kratochvil for b

$$\frac{b}{a} = 0.500 - 0.227 \log q \tag{1.19}$$

we can deduce

$$v_\perp \sim 100 M_1^{\frac{1}{3}}(1+q)^{\frac{1}{3}} P_{\text{day}}^{-\frac{1}{3}} \text{km s}^{-1}. \tag{1.20}$$

This is much larger than any conceivable sound speed, given that a normal stellar envelope temperature ($\lesssim 10^4$ K) implies $c_s \sim 10$ kms^{-1}. This result shows that the flow through L$_1$ is supersonic and will become even more so as the gas falls through the primary's potential. As a result the pressure forces in the equation of motion can be neglected and the trajectory becomes ballistic. Elements of the gas can now be considered by the motion of test particles. Given also that the velocity acquired during free fall is much larger than the initial $v_\parallel$ the motion will be insensitive to the exact initial conditions.

If we consider the particle to be released at rest (in the frame rotating with the binary) from L$_1$ the resulting orbit will be nearly elliptical and lie in the orbital plane. The presence of the secondary causes this orbit to precess, and consequently the stream of transferred material will intersect itself. Shocks are formed at this intersection which cause the dissipation of energy. However, the angular momentum of the material is still close to its high initial value and so the gas adopts the orbit of lowest energy for given angular momentum *i.e.* a circular orbit. The material will thus initially form a ring of radius R_{circ} which has the same specific angular momentum as it did at L$_1$. R_{circ} is thus determined by

$$(G M_1 M_\odot R_{\text{circ}})^{\frac{1}{2}} = b^2 \omega \tag{1.21}$$

Combining this with (1.10) and (1.19) gives

$$\frac{R_{\text{circ}}}{a} = (1+q)[0.500 - 0.227 \log q]^4 \tag{1.22}$$

The stages in the formation of an accretion disc are shown in figure 1.4.

An obvious condition for (1.22) to hold is that $R_{\text{circ}} > R_1$. However, a more precise and stringent condition is that the minimum distance of the stream from the white dwarf R_{min} should exceed R_1. This will be important when we discuss the magnetic cataclysmic variables.
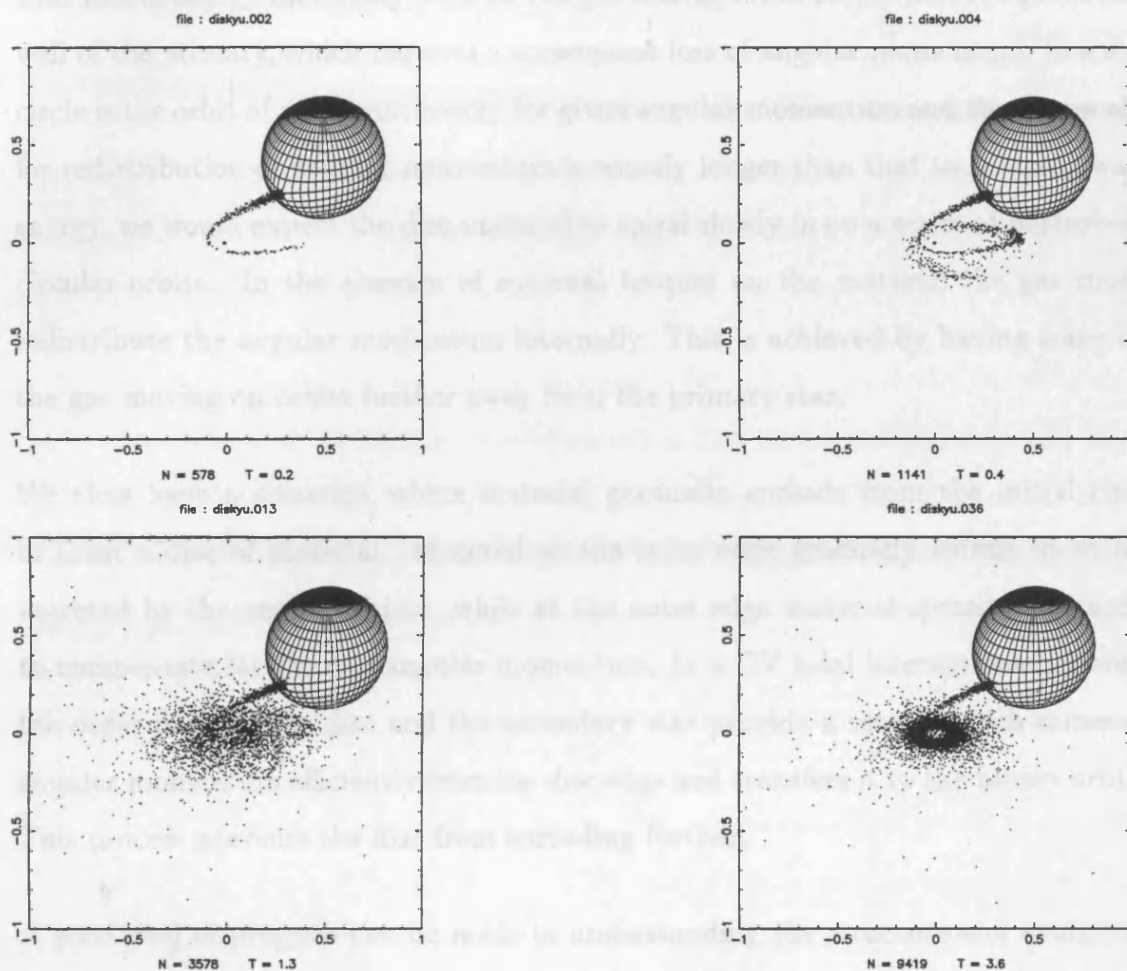
Figure 1.4: (Top Left) Mass transfer begins and the stream has too much angular momentum to be accreted directly and starts to orbit the star. (Top Right) The stream intersects itself and begins to dissipate kinetic energy. (Bottom Left) Dissipation continues and (Bottom Right) a ring forms as material circularizes which spreads under viscosity to form a disc.

Further evolution of the ring is driven by internal interactions between gas elements in the form of collisions, shocks and viscous interactions etc.. These interactions will convert some of the ordered bulk motion of the material in the ring into disordered internal heat energy. This energy will gradually be radiated away and lost to the gas. This loss of energy inevitably leads to the gas sinking more deeply into the potential well of the primary, which requires a consequent loss of angular momentum. Since a circle is the orbit of minimum energy for given angular momentum and the timescale for redistribution of angular momentum is usually longer than that to radiate away energy, we would expect the disc material to spiral slowly in on a series of perturbed circular orbits. In the absence of external torques on the material the gas must redistribute the angular momentum internally. This is achieved by having some of the gas moving on orbits further away from the primary star.

We thus have a situation where material gradually spreads from the initial ring to form a disc of material. Material at the inner edge gradually spirals in to be accreted by the central object, while at the outer edge material spreads outwards to compensate for the lost angular momentum. In a CV tidal interactions between the outer parts of the disc and the secondary star provide a torque which removes angular momentum efficiently from the disc edge and transfers it to the binary orbit. This process prevents the disc from spreading further.

A good deal of progress can be made in understanding the structure and evolution of accretion discs without recourse to the detailed atomic and plasma physics of the constituent gas. As accretion discs are common to both CVs and YSOs an outline of accretion disc theory will be given in section 1.3.

An alternative to the scenario depicted above for CVs occurs if the magnetic field of the primary is strong enough to dominate the flow of material. The strength of the WD field can be used to define a magnetospheric radius R_{mag} at which the the magnetic pressure of the field

$$P_{\mathrm{mag}} = \frac{B^2}{2\mu_0} \tag{1.23}$$

is greater than the ram pressure of the gas

$$P_{ram} = \rho v^2 \qquad (1.24)$$

i.e. where the field strength is great enough to dominate the gas motions. If $R_{min} <$ R_{mag} it is clear that the stream from L_1 will crash into the magnetic field before it is able to complete a single orbit. The gas will then be directed along the magnetic field lines to be accreted close to the magnetic poles of the WD. It is possible, however, that higher multipoles of the field may dominate close to the WD surface, causing accretion to occur away from the (dipolar) magnetic poles. This form of accretion occurs in the polar subgroup of CVs.

If $R_{min} > R_{mag}$ we would expect the stream to be able to orbit the the WD and since, probably, $R_{circ} > R_{mag}$ we would expect a disc to form. This disc will then spread in the same way as in the non-magnetic systems until the radius of the inner edge of the disc $R_{in} = R_{mag}$ (assuming, of course, $R_{mag} > R_1$) where the magnetic field will again dominate the motion of the gas and direct it on to the white dwarf. This form of truncated disc accretion is believed to occur in DQ Her and possibly some other weakly magnetic CVs.

The work of Wynn & King (1995) suggests that an intermediate group of systems proposed by Hameury, King & Lasota (1986) may exist where the magnetic field is not strong enough to prevent the gas from passing the minimum approach distance from the WD on its orbit. However, the magnetic field may extract so much energy from the gas as it passes through the magnetic field that effective disc formation is prevented since the orbit of the gas decays so quickly that accretion occurs after only a few orbits. These authors suggested that this explained the apparent relation $P_{spin} \sim 0.1 P_{orb}$ observed for many members of the intermediate polar subgroup of CVs. A graph of P_{spin} v P_{orb} is plotted in figure 1.5
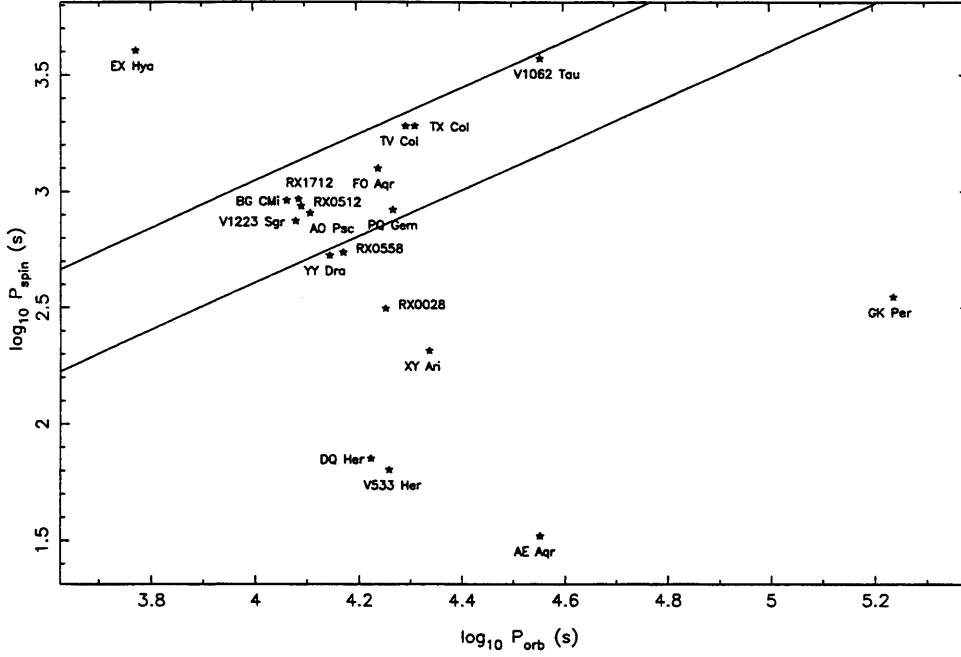
Figure 1.5: A graph of P_{spin} v P_{orb} for the intermediate polar group of CVs showing the apparent relation $P_{\text{spin}} \sim 0.1 P_{\text{orb}}$ by Wynn (1996, priv. comm.).

1.2.3 Taxonomy

Cataclysmic variables derived their name from their most striking feature: that they undergo cataclysmic increases in their brightness. The variety of phenomena which these systems exhibit has led to the introduction of several sub-classes.

Classical Novae

As material is accreted by the WD the amount of hydrogen in the surface layer increases and eventually a situation is reached where the temperature and pressure are sufficient to initiate nuclear burning. Since the WD is made of degenerate material the pressure exerted by the material is very insensitive to increasing temperature and a thermonuclear runaway is initiated as the energy released by nuclear burning increases the temperature which in turn increases the energy generation rate. The degeneracy is eventually lifted by this process and much of the surface layer is blown off explosively. The amount of energy released is enough to raise the brightness of the system by ~ 12 magnitudes. It is these explosive events which made previously

too faint systems observable to the astronomers of antiquity and gave rise to the term nova. It is thought that nova explosions occur from time to time in most or all CVs. Systems which have been observed to undergo such an outburst are called old novae. The recurrence time for nova explosions is at least 10^4 yr and may be much larger in some cases.

Dwarf-Novae

Dwarf novae also undergo regular 'outbursts' of increased luminosity ($\sim$ 2–5 magnitudes). However, the short recurrence time of weeks to a few months and smaller luminosity increases makes it extremely unlikely that the same mechanism is at work here as in classical novae. The outbursts are thought to be caused by a sudden increase in the amount of material deposited on the white dwarf. The mechanism giving rise to these increases in accretion is thought to lie in an instability in the mass-transfer process. There are currently two suggested theories for where the instability can arise. In the first the actual accretion disc structure becomes unstable at a critical surface density. In the second the instability is thought to arise in the mass-transfer rate. These will be discussed further in chapter 3.

Dwarf novae are further split into 3 subgroups

Z Cam These stars show protracted phases of constant luminosity around 0.7 magnitudes less than maximum brightness. During these phases outbursts cease for tens of days to years.

SU UMa As well as typical dwarf nova outbursts these stars also show superoutbursts. Here the system can achieve a brightness around 0.7 magnitudes greater than an ordinary outburst. Superoutbursts last $\sim$ 5 times longer than normal outbursts.

U Gem This group consists of all those dwarf novae which do not fall into the previous two groups.

Recurrent Novae

Recurrent novae are, by definition, systems previously identified as classical novae which have been found to repeat their eruptions. Given a steady mass transfer rate from the secondary the rate of deposition of material on the white dwarf is constant giving rise to regular outbursts. The distinction between recurrent and dwarf novae is clear spectroscopically as recurrent novae show shells of material ejected at high velocities from the explosions.

Novalikes

Novalikes include all the CVs which do not show outbursts. This paradoxical statement given the definition of a CV can be understood when it is realised that this group contains pre-nova and post-nova systems as well as perhaps Z Cam systems that are in such a long standstill that we have been unable to observe an outburst as yet. This class also includes the YY Scl (anti-dwarf novae) systems which show occasional reductions in brightness from an approximately constant maximum magnitude.

The magnetic systems discussed above are also included in the group. They are split into the high field polars and weaker intermediate polars (IPs) of which the DQ Her stars are a subset. The presence or not of a truncated disc in the IPs is matter of ongoing debate. However, it is clear that the field in the polars is strong enough to disrupt disc formation entirely. Material overflowing L_1 is rapidly forced to follow the fieldlines of the WD and is accreted in a restricted region around its magnetic poles. This gives rise to localised heating and the production of X-rays. The evolution and structure of the magnetic CVs will be discussed in more depth in chapter 4.

1.2.4   Observational Characteristics

Photometry

Given the short orbital periods of CVs (~few hours) and hence their small orbital separation ($\sim R_{\odot}$), eclipsing systems are not uncommon amongst CVs. When we couple this with the relative disparity in size between the components a good deal of information on the fundamental properties of the binary can be obtained from optical photometry. Rather than having a sharp ingress and egress to WD eclipse, CV light curves often show shallower slopes of variable gradient which are interpreted as arising from a disc. The light curves also show a broad hump having phase coverage $\lesssim 0.5$. This arises from the bright spot at the edge of the disc where the stream impacts upon it. Further evidence for this interpretation comes from the observation of flickering with amplitude 0.01–0.2 magnitudes and timescale ~ 60 s.

Spectroscopy

Optical and IR spectroscopy show emission lines of low-ionization states of the common elements: HI, HeI, HeII, FeII, CaII and OI along with a blend of CIII, OII and NII. In the UV more highly ionized species are observed: Ly_{α}, HeII, CII–CIV, NIII–NV, OI, OIII, OV, MgII, AlIII, and SiII–IV. Because of the variation of conditions through the disc lines are often formed at different positions: some in the disc atmosphere, some in the outer regions and some at the bright spot. The fact that these lines are present even during eclipse and show double peaked line profiles distinctive of rotation indicate that they come from the disc. The formation of these profiles is shown in figure 1.6. The Keplerian velocities of the disc material are ~ 1000 km s^{-1} which compares to a sound speed (typical of the thermal velocities) $\lesssim 10$ km s^{-1}. As a result the lines are Doppler broadened. As material in the disc comes towards the observer the line is blue shifted and that moving away red shifted. The end result is a profile similar to that shown in the figure. The distance between the peaks gives an estimate of the disc radius.
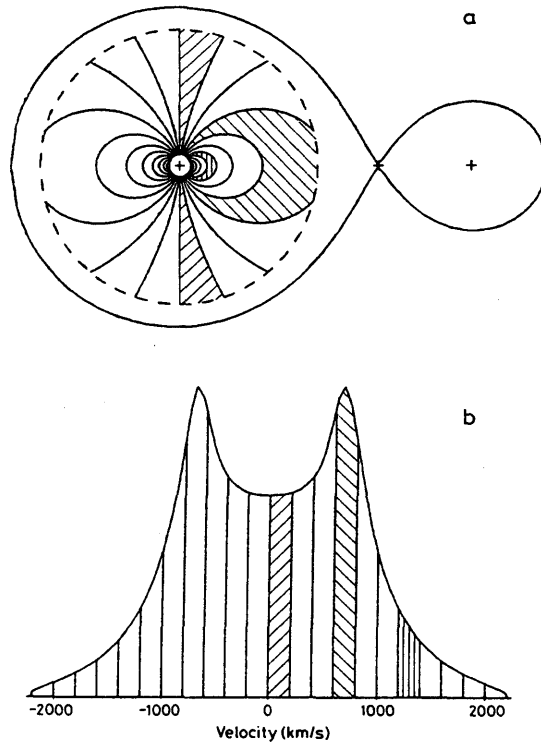
Figure 1.6: (a) Loci of constant radial velocity in a Keplerian disc in a binary with $q = 0.15$ viewed at quadrature. (b) Velocity profile of emission lines from the disc. Emission in the shaded velocity ranges originate in the corresponding shaded regions of the disc. From Horne & Marsh (1986).

UV spectroscopy with IUE shows some evidence of P Cyg profiles for systems with high mass transfer rates and $i \lesssim 65°$ which are indicative of mass-loss in the form of a wind from the disc.

Infrared

Infrared is the best window in the spectrum for determining information about the cool secondary stars which are drowned out at higher frequencies. There is, however, some interference with the cool outer regions of the disc. IR photometry can reveal significant ellipsoidal variation. This phenomenon arises from the varying projected surface area of a Roche-lobe filling star seen by an observer at different phases. Observations of polars are often show polarisation in the IR arising from the stream.

X-rays

Despite their rapid rotation the likely X-ray production of the dwarf secondary stars is unlikely to be large enough to supply the observed X-ray luminosity (L_x) of CVs. From disc theory we would expect there to be a boundary layer close to the star. In this region the velocities of the gas elements are slowed from their Keplerian velocities to match the rotation rate of the star. If the latter is much lower than Keplerian, this gives rise to shocks and localised heating of the disc material to a temperature characteristic of X-ray production. In dwarf novae, for example, hard (0.1–5 keV) X-rays are seen in quiescent phases whereas those in the soft (10-30 eV) band are rarely observed. L_x is variable on a timescale of minutes by factors of 2–10. This suggests that the accreted material is inhomogeneous.

In magnetically channelled accretion flows X-rays are expected in three separate regimes. As the accreted column of material is slowed and shocked we would expect to observe hard X-ray bremsstrahlung. Near-relativistic electrons in the flow will give rise to cyclotron emission as they spiral about the fieldlines. The column is optically thick to the low harmonics but thin to the higher ones. Approximately

50% of the X-rays that are emitted by the column are either reflected by the WD ($E \gtrsim 30$ keV) or absorbed, thermalised and re-emitted with an approximately black-body spectrum in soft X-rays or UV. Polars, however, show much more soft X-ray flux than would be expected from this picture. This can arise if the accretion column is composed of clumps or 'blobs' of material proposed by Kuijpers & Pringle (1982) some of which have sufficient density and momentum to penetrate into the WD atmosphere. The hard X-rays produced by this process will then be thermalised and re-emitted in the soft X-ray region (Frank, King & Lasota 1988).

Further evidence for this blobby accretion process comes from the observation that the X-ray light curves are surprisingly noisy for all types of magnetic CVs. This noise can be modelled successfully for the polars by the arrival of small numbers of blobs. The polar system EF Eridani also shows a dip in the X-ray light curve interpreted as eclipsing of the accretion region by the stream. There is a corresponding IR dip at this phase, probably caused by free-free absorption, which increases strongly with wavelength. However, the IR does not show the wavelength dependence expected for free-free absorption by a homogeneous medium. Rather it is consistent with a scenario where the material is clumped into optically thick blobs separated by more tenuous optically thin plasma.

1.3   Accretion Physics

Accretion of material is important in a wide variety of astrophysical situations from the formation of stars and planets to providing the power source for active galaxies. The processes which occur are often similar, allowing a good deal of insight to be gained from a single theoretical approach. In the later parts of this thesis we shall be considering young T Tauri stars and Cataclysmic Variable binaries, and in the following discussions we shall concentrate on the aspects of accretion theory which are of particular relevance to them. The derivation of the equations governing the evolution and structure of accretion discs are very long and are dealt with in several

textbooks *e.g.* Frank, King & Raine (1992). Thus, rather than developing the theory in detail, we shall highlight important aspects.

The essential condition for the formation of an accretion disc is the presence of a large body of fluid with high specific angular momentum moving in the gravitational potential of a central object. In T Tauri stars the angular momentum is supplied by the vast size of the gas cloud out of which the star is being formed. In CVs the angular momentum is supplied by material leaving the secondary with approximately the same specific angular momentum as the secondary in its orbit.

Starting from the equations of conservation of mass and angular momentum one can derive simple relations which govern the time evolution of a disc:

$$R\frac{\partial \Sigma}{\partial t} + \frac{\partial}{\partial R}(R\Sigma v_{\rm R}) = 0 \tag{1.25}$$

and

$$\frac{\partial \Sigma}{\partial t} = \frac{3}{R}\frac{\partial}{\partial R}\left\{R^{\frac{1}{2}}\frac{\partial}{\partial R}(\nu\Sigma R^{\frac{1}{2}})\right\} \tag{1.26}$$

where R is the distance of the point under consideration from the disc centre, Σ is the surface density of the gas, $v_{\rm R}$ is the radial drift velocity of the disc material and ν is the viscosity. Given a solution for the disc it is possible to calculate $v_{\rm R}$. This enables us to define a timescale for viscous interactions to significantly alter the disc

$$t_{\rm visc} \sim \frac{R}{v_{\rm R}}. \tag{1.27}$$

By looking for a steady state solution (*i.e.* $\frac{\partial}{\partial t} = 0$) of these equations coupled with appropriate boundary conditions it is possible to derive a set of equations describing the structure of a steady state thin disc. The thin disc approximation is that the scale height of the disc $H \ll R$, which can be shown to amount to the restriction that the Keplerian speed in the disc is hypersonic. The disc is, however, optically thick so that the continuum spectrum is close to a blackbody. Thus $\tau = \rho H \kappa = \Sigma \kappa \gg 1$. The steady disc equations are

$$\rho = \frac{\Sigma}{H}; \tag{1.28}$$

$$H = \frac{c_s R^{\frac{3}{2}}}{(GM)^{\frac{1}{2}}}; \tag{1.29}$$

$$c_s = \frac{P}{\rho}; \tag{1.30}$$

$$P = \frac{\rho kT}{\mu m_p} + \frac{4\sigma T^4}{3c}; \tag{1.31}$$

$$\frac{4\sigma T^4}{3\tau} = \frac{3GM\dot{M}}{8\pi R^3}\left[1 - \left(\frac{R_*}{R}\right)^{\frac{1}{2}}\right]; \tag{1.32}$$

$$\tau = \Sigma\kappa = \tau(\Sigma, \rho, T); \tag{1.33}$$

$$\nu\Sigma = \frac{\dot{M}}{3\pi}\left[1 - \left(\frac{R_*}{R}\right)^{\frac{1}{2}}\right]; \tag{1.34}$$

$$\nu = \nu(\rho, T, \Sigma...). \tag{1.35}$$

There are two terms above without explicit equations: the optical depth τ in (1.33) can be calculated using a suitable expression for the opacity κ such as Kramers' opacity; the viscosity ν in (1.35) is, however, more problematical.

The origin of viscosity in discs is unknown given that the gas flow is likely to involve turbulence. The turbulent eddies will be characterised by the size λ_{turb} and turnover velocities v_{turb} of the largest components. On dimensional grounds, then, we might expect $\nu_{turb} \sim \lambda_{turb}v_{turb}$. Since λ_{turb} must be less than H and v_{turb} is almost certainly less than c_s (else shocks would thermalise much of the energy) we can write,

$$\nu = \alpha c_s H \tag{1.36}$$

where all our ignorance of the viscous processes is now contained in the Shakura-Sunyaev α-prescription with $\alpha \lesssim 1$. This parameterisation is usually taken as a constant value and, although there is no physical reason why this must hold, useful results can still be obtained as the power to which α appears in the disc solutions is small (Frank, King & Raine 1992). This type of prescription also describes cases in which viscosity is magnetic in origin, eg. Hawley & Balbus (1991) and Tout & Pringle (1992b).

1.3.1 The Interaction of Magnetic Fields with Discs

Given the presence of discs and magnetic fields in so many different astrophysical situations it is clearly important to understand how they interact. In general, however, the interaction of a magnetic field with a plasma is extremely complex, requiring the time-dependent solution of Maxwell's equations and a treatment of magnetic reconnection events. In this magnetohydrodynamic (MHD) problem the magnetic field determines the dynamics of the plasma elements and the motions of the plasma result in a change in the magnetic field structure. The problems which result are discussed by Priest (1982) and Dendy (1990) amongst others.

This MHD approach shows that any external field applied to a plasma is 'frozen-in' *i.e.* the magnetic flux through any volume element is constant. The effect of this in a disc system is for the initially dipolar field lines to be deformed and dragged round by the bulk motion of the fluid. The consequent winding-up which would result is relieved when it is energetically favourable for the magnetic field to reconfigure itself closer to its initial dipolar configuration via a reconnection event. Formally the force *density* acting on a plasma can be expressed as

$$\mathbf{f} = -\nabla P - (\nabla - \hat{\mathbf{b}}\frac{\partial}{\partial s}) \left(\frac{B^2}{2\mu_0} \right) + \frac{1}{R} \left(\frac{B^2}{\mu_0} \right) \hat{\mathbf{n}} \qquad (1.37)$$

where $\hat{\mathbf{b}}$ is the local field direction, R the radius of curvature of the deformed field line and $\hat{\mathbf{n}}$ the normal to the field line. The second term acts like a magnetic pressure which acts to drive the fluid away from high field regions. The third term is a tension in the deformed field lines where the field attempts to straighten itself and thus exerts a force on the plasma. This gives us the force on the plasma for a given field configuration. It is not, however, a full solution to the coupled field-fluid equations.

An alternative approach which is extremely easy to implement numerically seeks to exploit the inhomogeneities in the flow which were mentioned above. Drell, Foley & Ruderman (1965) developed a treatment of a conductor moving in a magnetic field which experiences a diamagnetic drag force. If much of the mass in the accretion

flow is concentrated into these 'blobs' we can successfully follow their progress with

a simple addition to the equations of motion without the need to resort to full MHD.

There are several mechanisms which may give rise to the formation of blobs. Firstly, the intrinsically turbulent nature of the flow in an accretion disc will almost certainly give rise to compressions and rarefactions of the fluid. Blobs may also be formed via the Rayleigh-Taylor instability if an accretion stream is held up by a magnetic field. Although the field may have sufficient pressure formally to hold up the flow it will be unstable to droplets forming at the fluid-field interface. Blobs may also be formed, in the case of a CV, via instabilities in the mass-transfer process. Perturbations in the atmosphere of the secondary are unlikely to allow a homogeneous stream of material to pass through L_1, instead the stream is likely to be broken up into discrete packets. Indeed the cooling curve of matter subjected to irradiation by the accreting component has prominent minima, suggesting that thermal instabilities will cause blobs to form.

Details of both these approaches will be discussed as they are used in the appropriate chapters. It is worth bearing in mind, however, that these approaches coincide for strong fields *i.e.* where the trajectory of material is essentially directed along field lines.

1.4 The Simulations

The extension of the analytic treatment of single particle orbits in the spherical potential of the white dwarf to the treatment of many particles in the full Roche potential of the binary system clearly requires numerical treatment. By such numerical means the picture of disc formation and evolution presented in the previous sections can be expanded to include the viscous forces between gas elements and allows study of the velocity, dissipation and angular momentum structure of the resulting accretion flow. The numerical approach adopted for this many-particle model involved the use of the particle simulation code HyDisc which was first written to study the

superoutburst behaviour of the SU Ursae Majoris group of CVs (Whitehurst 1988a). This was developed and tested extensively by Whitehurst (see Whitehurst (1987) for detailed discussion) and first applied to magnetic CVs by Wynn (1993). This section will provide a brief overview of HyDisc. We shall discuss the adaptations made to the code to model the peculiar situations to which we have applied it in the appropriate chapters.

1.4.1 HyDisc

Whitehurst (1987) deals with the design, implementation and testing of HyDisc in considerable detail, so we shall simply to provide a summary of the important features of the code.

Most generally HyDisc treats the accretion flow as if composed of many discrete particles, each of which carry mass and angular momentum. These particles are moved in the potential well of the binary system according to appropriate equations of motion, and allowed to interact with each other at intervals, in a way which simulates viscosity. All of this motion and particle interaction takes place in the *computational zone* which is set up in the frame co-rotating with the binary, and is defined by:

1. The radius of the primary $r = R_1$. Any particle crossing this radius is assumed to be accreted by the white dwarf.

2. The boundary of the secondary $s = R_L$, where s is the distance from the centre of mass of the secondary and R_L defines the Roche lobe radius of the secondary star. Any particle crossing this boundary is assumed to be re-accreted by the secondary.

3. The escape radius $r = R_{esc}$, at which the particle is assumed to have escaped the system altogether (usually $\sim$ 5–10 separations).

Particles are injected into the computational zone through the L_1 point on the Roche lobe of the secondary. The input stream has initial conditions (in the co-rotating frame), such that the stream speed is typical of the sound speed in the atmosphere of the secondary, and has a direction which is in the plane of the binary orbit and lies a little ahead of the primary when viewed from the L_1 point.

Once in the computational zone each particle is subject to the forces governed by the equations of motion (the field equations), and the particle-particle interactions which determine the artificial viscosity. To evolve the particle motions in a computationally efficient manner each particle is allotted a timestep (after which the short-range viscous forces will be applied) from the allowed set

$$\Delta t_i = 2^{-i} \Delta t \quad \text{where } i = 0, 1, 2...$$
(1.38)

here Δt is the largest allowed timestep. This method enables the computationally efficient advancement of the system (as opposed to the highly inefficient application of the smallest timestep to all particles) by moving each particle through its timestep Δt_i according to the field equations and then allowing all concurrent particles to interact simulating pressure and viscous forces. It is these viscous interactions which determines the particle's timestep. As far as such interactions are concerned the particles are infinitely compressible, and neighbours separated by a distance r can be regarded as exerting a pressure force upon each other through their common surface area A_p. Assuming that the particles consist of an ideal gas the pressure force over this area will be given by $P = \rho_p c_s^2$, where ρ_p is the mean density, and c_s is the isothermal sound speed. Since $A_p \sim r^2$ we have a pressure acceleration

$$a_p \sim c_s^2 / r.$$
(1.39)

In addition to this pressure term viscous forces come about from the collisions between the particles. Considering the collision of two particles separated by a distance r and closing with a supersonic line-of-centres velocity $-u$, a shock front will develop between the particles decelerating them through u in a time $t_{coll} \sim |r/u|$. This implies an average repulsive acceleration

$$a_v \sim u^2 / r.$$
(1.40)

From (1.39) and (1.40) the total acceleration between the particles is given by

$$a = \begin{cases} C^2/r + Qu^2/r & u < 0 \\ C^2 & u \geq 0 \end{cases}$$

here Q is in fact the coefficient of restitution of the collision, so $0.5 \leq Q < 1.0$ for inelastic, non-penetrative collisions. Any energy dissipated during the collisions is assumed to be immediately radiated through the upper and lower surfaces of the disc (thus implying that the disc is thin).

The time t_{coll} is termed the collision time and it is this which determines the particle's timestep, effectively the time between collisions. For each interaction HyDisc selects the particle pair whose interaction has the greatest effect on the simulation. This means selecting the pair with the shortest interaction time (*i.e.* strongest collision) or when no particles are approaching the nearest neighbours (which apply the strongest pressure forces). This is achieved in HyDisc by the introduction of a 'chaining mesh' on the computational zone, whose grid cells have a size r_v, which is the effective range of the viscous and pressure forces. Thus any neighbour in the effective range must lie in the same cell, or one of the 26 (8 if the 2-D version of the code is used) adjacent cells to the particle in question. Since the particles are stored in a *linked list*, *i.e.* a chain of particles in which each particle knows the whereabouts of the next member of the chain, all particles within r_v can be quickly located (it was for the simple implementation of such linked lists that HyDisc was coded in 'C' rather than FORTRAN). The free parameter r_v (along with Q) is one of the main methods of control the user has over the particle viscosity.

1.4.2 The equations of motion

The movement of each particle over its particular timestep requires the equations of motion to be determined in the HyDisc coordinate system. This system is a set of cartesian coordinates centred on the white dwarf in a frame co-rotating with the binary as shown in figure 1.7. Since the masses represented by the particles are negligible compared to the mass of either star, the equations of motion are those of
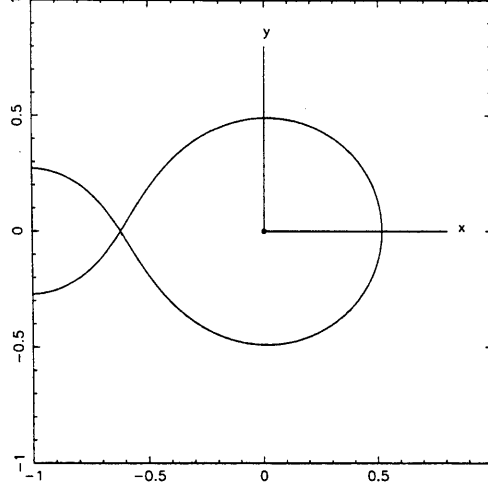
Figure 1.7: A portion of the HyDisc computational zone indicating the orientation of the x and y axes. In the diagram the orbital motion of the secondary is anti-clockwise.

the restricted three body problem. Remembering that pressure forces are dealt with elsewhere (1.12) can be written as

$$\ddot{\mathbf{r}} = -\frac{GM_1 M_\odot (\mathbf{r} - \mathbf{r_1})}{|\mathbf{r} - \mathbf{r_1}|^3} - \frac{GM_2 M_\odot (\mathbf{r} - \mathbf{r_2})}{|\mathbf{r} - \mathbf{r_2}|^3} - 2(\mathbf{\Omega} \wedge \mathbf{v}) - \mathbf{\Omega} \wedge \mathbf{\Omega} \wedge \mathbf{v} \qquad (1.41)$$

For a system of separation A with the secondary centred on a point at a distance D_2 from the centre of mass along the x-axis, and the primary similarly centred at a distance D_1, we find the equations of motion as

$$\ddot{x} = 2\dot{y}\Omega + x\Omega^2 + D_1\Omega^2 - \frac{GM_1 M_\odot x}{R^3} - \frac{GM_2 M_\odot (x + A)}{S^3} \qquad (1.42)$$

$$\ddot{y} = -2\dot{x}\Omega + y\Omega^2 - \frac{GM_1 M_\odot y}{R^3} - \frac{GM_2 M_\odot y}{S^3} \qquad (1.43)$$

$$\ddot{z} = -\frac{GM_1 M_\odot z}{R^3} - \frac{GM_2 M_\odot z}{S^3} \qquad (1.44)$$

where we have written $R^3 = |\mathbf{r_1} - \mathbf{r}|^3$ and $S^3 = |\mathbf{r_2} - \mathbf{r}|^3$. HyDisc employs a simplified set of dimensionless equations by means of the scalings $A = 1$ and $\Omega = 1$.

If

$$\mu = \frac{M_1}{(M_1 + M_2)} \tag{1.45}$$

we have that $D_2 = \mu$ and $D_1 = 1 - \mu$, and from Kepler's third law $GM_1 M_\odot = \mu$ and $GM_2 M_\odot = 1 - \mu$. Making these transformations (1.42),(1.43) and (1.44) simplify to

$$\ddot{x} = 2\dot{y} + x + 1 - \mu - \frac{\mu x}{R^3} - \frac{(1 - \mu)(x + 1)}{S^3} \tag{1.46}$$

$$\ddot{y} = -2\dot{x} + y - \frac{\mu y}{R^3} - \frac{(1 - \mu)y}{S^3} \tag{1.47}$$

$$\ddot{z} = -\frac{\mu z}{R^3} - \frac{(1 - \mu)z}{S^3} \tag{1.48}$$

which are the required, dimensionless field equations of the particles in the co-rotating frame of the binary.

Chapter 2

Young Stellar Objects

2.1 Introduction

Two of the outstanding problems in the study of YSOs are the low rotation rate of T Tauri stars (an order of magnitude less than breakup) and the production of bipolar outflows. The outflows themselves fall into two categories: the optical jets which are well collimated and have typical velocities of 100–300 km s^{-1} and the molecular outflows which are less well collimated and have typical velocities in the range 10–30 km s^{-1}. The typical mass loss rates for the jets are ~ 0.05–2×10^{-8} M$_\odot$ y^{-1} (Mundt, Brugel & Bührke 1987) and for the molecular flows are $\sim 10^{-7}$ M$_\odot$ y^{-1} (Lada 1985).

King & Regev (1994, hereafter KR) proposed that the low rotation rates and molecular outflows could be explained simultaneously given the presence of a magnetic loop structure on the central star in a T Tauri-disc system. The loop was assumed to interact with the disc material via a magnetic drag force. This approach to magnetic field-disc interactions had proved useful in explaining the properties of the Intermediate Polar (IP) sub-class of Cataclysmic Variable (CV) systems. They predicted an equilibrium spin rate for the star putting the corotation radius approximately at the edge of the loop. In their paper KR presented an analytical treatment of the

problem and some single particle simulations and suggested that subsequently N-body simulations could prove fruitful. In this chapter we shall examine such N-body simulations.

This work differs from previous descriptions of disc-magnetic field interaction (eg. Pudritz & Norman 1986; Wardle & Königl 1992; Lovelace, Romanova & Contopoulos 1992) in that the field in this investigation is generated by and anchored in the star. The influence of the field is also sharply localised to the very inner edge of the disc since it is confined to the volume around a specific point on the stellar surface. The cited authors all follow the scheme of a poloidal field threading much of the disc. This field is either generated by the disc itself or is taken to be the interstellar field. We do not attempt to model the detailed disc structure; rather we attempt to assess the feasibility of a scheme which directly couples the angular momentum problem of T Tauris and the generation of outflows.

The disc material is modelled as gas blobs behaving diamagnetically in the presence of the loop following the scheme of Drell, Foley & Ruderman (1965) . These authors showed that the timescale for a diamagnetic object of mass m, orbiting in a magnetic field B to lose energy as it crosses field lines is

$$t_{\mathrm{drag}} = \left(\frac{\mu_0}{4\pi}\right) \frac{c_A m}{B^2 l^2} \tag{2.1}$$

where l is a typical length scale for the object. There is a minimum conductivity condition for this equation to hold which is

$$\sigma > \frac{c^2}{2\pi l c_A}. \tag{2.2}$$

KR showed that this reduces to a condition on the length scale of the blobs

$$l \gtrsim 10^{-5} \frac{N_{\mathrm{n}}}{N_{\mathrm{e}}} \frac{\rho_{-7}^{\frac{1}{2}} T_3^{\frac{1}{2}}}{B_{-1}} \text{ m.} \tag{2.3}$$

where N_{n} and N_{e} are the number densities of neutrals and electrons, ρ_{-7} is the density in units of 10^{-7} kg m^{-3}, T_3 is the temperature is units of 1000 K and B_{-1} is the magnetic field strength in units of 0.1 T. This is satisfied for all realistic parameters and we define a drag coefficient $k = t_{\mathrm{drag}}^{-1}$ for the blobs. We write the

drag force per unit mass as

$$\mathbf{f}_{\text{drag}} = -k[\mathbf{v}' - (\mathbf{v}'.\hat{\mathbf{b}})\hat{\mathbf{b}}] \tag{2.4}$$

where $\mathbf{v}'$ and $\mathbf{b}$ are the blob velocity and field direction in the frame rotating with the field.

2.2 The Simulation

The code used was an adapted version of HyDisc (Whitehurst 1988b). This was originally written to study the accretion processes in CVs (Whitehurst 1988a). The major changes were the addition of an extra term in the long-range force calculation to simulate the drag by the loop and the removal of the gravitational contribution of the secondary star. A calculation of the angular momentum exchanged during the star-particle interaction was also added so that the consequent spin evolution could be followed. Since the long range forces are calculated separately from the short range we can easily calculate the angular momentum exchanged between the star and the particle. Since angular momentum is conserved by gravitation any change in the particle's angular momentum will have resulted from the magnetic field terms in the equations of motion. A similar calculation has been carried out using HyDisc for IPs (Wynn & King 1995).

The particles were injected during the first 10 y of the simulation with a Gaussian spread in axial distance from the central star and at a random phase on circular Keplerian orbits. The disc plane was made coincident with the stellar equator. During this period the spin rate was held constant. A low-radius cutoff was introduced to prevent particles from being injected where they would feel a significant initial force from the loop. This prevented large numbers of particles being artificially ejected from the system in an initial burst. A random contribution, appropriate to the local disc temperature was added to each of the velocity components. A small Gaussian displacement out of the disc plane was also allowed. The temperature variation in

the disc used to calculate the sound speed and hence the pressure force between particles was calculated analytically according to

$$T(R) = \left\{ \frac{3GM\dot{M}}{8\pi R^3 \sigma} \left[1 - \left(\frac{R_*}{R}\right)^{\frac{1}{2}} \right] \right\}^{\frac{1}{4}} \qquad (2.5)$$

(Frank, King & Raine 1992). A more accurate method would be to use the mid-plane temperature rather than the photospheric value but given the relative slight effect of pressure in a thin disc the error introduced is negligible. Also the mid-plane temperature is in general only slightly larger than the effective temperature given by (2.5) (cf Frank et al. 1992). A reference distance of 3 stellar radii was chosen as a height that might reasonably be regarded as being just outside the accretion boundary layer and at which temperature estimates have been made (Basri & Bertout 1989). This reduces (2.5) to

$$T(R) = T(3R_*) \left\{ \frac{27}{1 - \frac{1}{\sqrt{3}}} \left(\frac{R_*}{R}\right)^3 \left(1 - \left[\frac{R_*}{R}\right]^{\frac{1}{2}} \right) \right\}^{\frac{1}{4}} \qquad (2.6)$$

Particles were removed from the simulation by testing when they crossed two boundary radii. When crossing inside the radius of the central star they were removed as accreted material. On crossing an outer boundary they were tested for positive total energy and removed as escaped material. The escaping particles fell into two classes: material ejected by gaining energy directly from the rotation of the central object via the magnetic loop and material achieving escape speeds from purely thermal interactions. This latter component is an artefact of the simulation, since in order to keep the run-time to a manageable length we have modelled only the inner regions of the disc. As a consequence material at the outer edge of the simulation was still hot enough to evaporate from the system some particles in the tail of the Maxwell-Boltzmann distribution. In reality the rest of the disc material orbiting at larger radii would keep this evaporating material in the disc. Similar numbers of particles evaporate when no loops are present, confirming the cause as thermal evaporation, rather than ejection after collision with particles that have been hit by the loop. For

the parameters used in section 3, the difference between the escape and Keplerian speeds at the outer edge of the simulation is 2 561 ms^{-1}. Assuming the disc material to be an ideal gas the sound speed at this radius is 491 ms^{-1}. The ratio between these two quantities is $\sim$ 5.2 which implies that a small but noticeable fraction of the particles are able to escape by thermal interactions alone. We have not attempted to model the detailed structure of the disc; rather, we have used the disc to provide an appropriate supply of particles to the star and to act potentially as a barrier against ejection of material close to the plane. The two escaping components were separated by flagging all those particles which felt a non-zero force from the magnetic loop.

The loop was modelled as open radial field lines emanating from a point on the surface of the star. As noted above the diamagnetic drag acts to remove energy as the blob crosses the field lines. This results in the blobs tending to slide along the field lines although motion across field lines can still occur. Centring the loop in either the northern or southern hemisphere will consequently produce motions out of the disc plane.

Following the spirit of KR the strength of the field was made Gaussian in both spherical polar angles and had a radial cutoff given by $1 - \tanh((r - r_0)/w)$. This gives an expression for the drag coefficient k as

$$k = k_0 \frac{\exp -\{\frac{1}{2}[(\frac{\phi-\phi_0'}{\sigma_\phi})^2 + (\frac{\theta-\theta_0}{\sigma_\theta})^2]\}}{1 + \exp\{2(\frac{r-r_0}{w})\}} \qquad (2.7)$$

where (r,θ,ϕ) is a general point in spherical polar coordinates, (r_0,θ_0,ϕ_0') is the time-dependent (due to the stellar rotation) position of the loop centre and w,σ_θ and σ_ϕ are constants regulating the speed of decrease of k from k_0 on moving away from the central point.

Figure 2.1 is a diagram showing contours of constant $\frac{k}{k_0}$ in the plane defined by $\phi = \phi_0'$ for the parameters used in the first simulation. Similar contours exist in the plane $\theta = \theta_0$. These contours are not the same as the field lines, which as noted above, diverge radially from the surface at the point (R,θ_0,ϕ_0'). Clearly this is not a full description of the geometry found in a magnetic loop: such a structure is
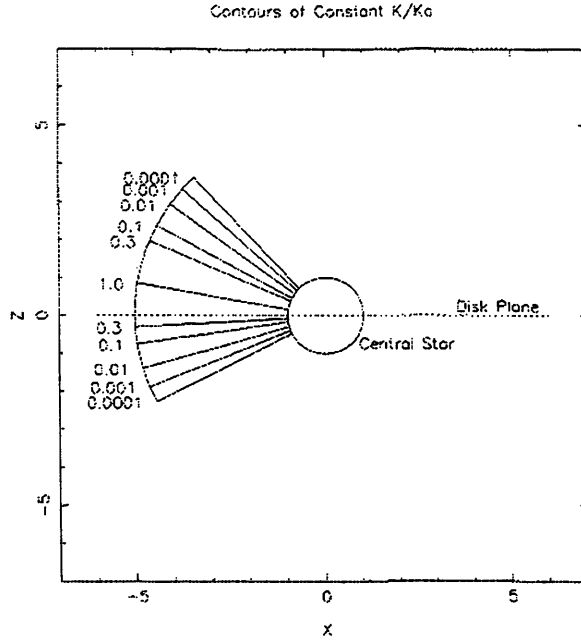
Figure 2.1: The contours of constant $\frac{k}{k_0}$ in the plane defined by $\phi = \phi_0'$ for the parameters used in the first simulation.

extremely complex. However, this description is sufficiently accurate to decide the plausibility of the scenario.

We can now evaluate the terms in equation (2.4).

$$\hat{\mathbf{b}} \equiv \frac{1}{|\mathbf{b}|} \begin{pmatrix} b_x \\ b_y \\ b_z \end{pmatrix} = \frac{1}{|\mathbf{b}|} \begin{pmatrix} x - R\cos\phi'\sin\theta_0 \\ y - R\sin\phi'\sin\theta_0 \\ z - R\cos\theta_0 \end{pmatrix} \qquad (2.8)$$

and

$$\mathbf{v}' \equiv \begin{pmatrix} \dot{x}' \\ \dot{y}' \\ \dot{z}' \end{pmatrix} = \begin{pmatrix} \dot{x} \\ \dot{y} \\ \dot{z} \end{pmatrix} - \begin{pmatrix} \dot{x}_{\text{loop}} \\ \dot{y}_{\text{loop}} \\ \dot{z}_{\text{loop}} \end{pmatrix} \qquad (2.9)$$

where x, y, z are the cartesian co-ordinates of the particle in the frame defined in section 1.4.1 and R is the radius of the star. A little thought about the geometry of the rotation produces

$$\dot{x}_{\text{loop}} = -r_{\text{p}}\omega \sin\phi_{\text{p}} \sin\theta_p \qquad (2.10)$$

$$\dot{y}_{\text{loop}} = r_{\text{p}}\omega \cos\phi_{\text{p}} \sin\theta_p \qquad (2.11)$$

$$\dot{z}_{\text{loop}} = 0 \tag{2.12}$$

where $(r_{\text{p}}, \theta_{\text{p}}, \phi_{\text{p}})$ is the position of the particle in polar co-ordinates. If we write,

$$D = \frac{(\mathbf{v'} \cdot \mathbf{b})}{|\mathbf{b}|^2} \tag{2.13}$$

we end with the components of the acceleration produced by the drag force

$$\ddot{x} = -k[\dot{x}' - Db_x] \tag{2.14}$$

$$\ddot{y} = -k[\dot{y}' - Db_y] \tag{2.15}$$

$$\ddot{z} = -k[\dot{z}' - Db_z] \tag{2.16}$$

which were added to (1.46),(1.47) and (1.48) after the removal of the secondary's gravitation. The full equations of motion thus become

$$\ddot{x} = 2\dot{y} + x - \frac{x}{r_{\text{p}}^3} - k[\dot{x}' - Db_x] \tag{2.17}$$

$$\ddot{y} = -2\dot{x} + y - \frac{y}{r_{\text{p}}^3} - k[\dot{y}' - Db_y] \tag{2.18}$$

$$\ddot{z} = -\frac{z}{r_{\text{p}}^3} - k[\dot{z}' - Db_z]. \tag{2.19}$$

The value of k has implications for the size of the blobs represented by the particles. The spatial variation of k given by (2.7) represents the variation of the magnetic field strength in the loop. If we assume a typical value for B of 0.3 Tesla and take $c_A \sim c$ (2.1) becomes

$$k_0 = \frac{3.00 \times 10^{-3} l^2}{m} \text{ s}^{-1}. \tag{2.20}$$

Representing the blob as a sphere with constant density gives

$$l = \frac{5.73 \times 10^{-3}}{k_0 \rho} \text{ m.} \tag{2.21}$$

Typical accretion stream densities are 10^{-7} kg m^{-3} (KR) and so the typical length scale is

$$l = \frac{5.73 \times 10^4}{k_0} \text{ m.} \qquad (2.22)$$

In order to study the spin behaviour, the moment of inertia of the central star was artificially reduced so that evolution could take place on a practical timescale. This does not affect the quantitative results of the simulation as long as the viscous timescale in the disc is still shorter than the spin evolution timescale.

In general, as the simulation had to follow a spin change over a complete order of magnitude, the factor reducing the moment of inertia had itself to be reduced before the equilibrium value was reached. This was necessary to achieve sufficient resolution to define the equilibrium spin value.

2.3 Results

A run was carried out for a 1 M$_\odot$, 2 R$_\odot$ star spinning with an initial period of 45 792 s (0.53 days). This compares to the breakup rate of 28 327 s. The loop extended to 4 R$_*$ above the stellar surface and had a k_0 value of 1.99×10^{-3} s^{-1}. This implies from (2.22) that the blobs had a length scale of 2.88×10^7 m. The other loop parameters were $\theta_0 = 1.4$, $\phi_0 = 3.1415$, $\sigma_\theta = \sigma_\phi = 0.15$, $w = 10^{-10}$. The outer boundary for removal of particles was at a radius of 23.2 AU. The computation was carried out using 10^4 particles. A reference temperature of 3 000 K was used for $T(3R_*)$ in (2.6) (Basri & Bertout 1989). The simulation took a total of 23.9 CPU days.

The spin rate is plotted against time in figure 2.2. The equilibrium rate is 2.9 days (250 560 s)which compares with the expected value of 3.67 days (316 705 s, equation (13) of KR).

The speed in the z-direction (corrected for the escape speed) for particles ejected

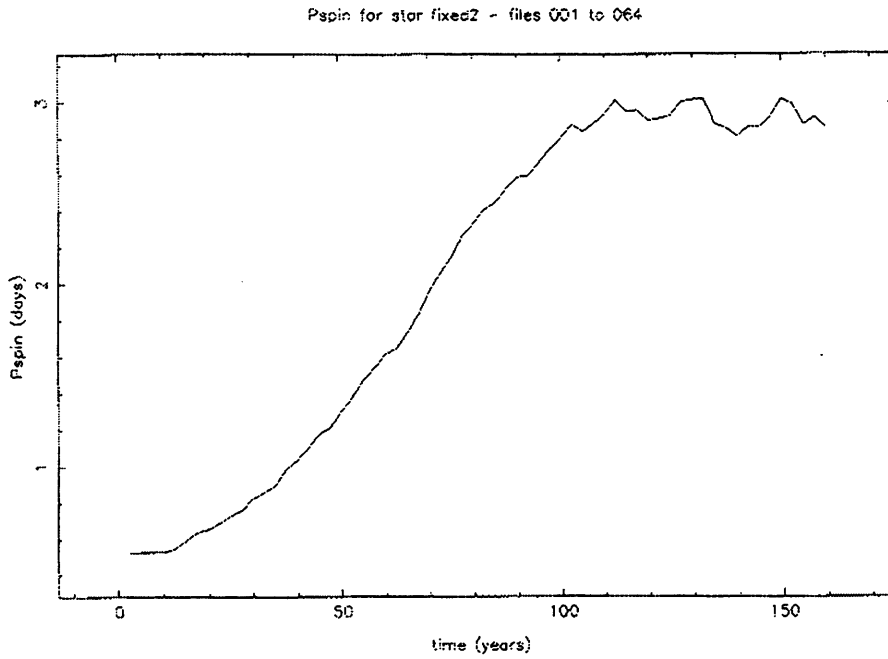Pspin for stor fixed2 - files 001 to 064

Figure 2.2: A graph of spin period against time for the first HyDisc simulation.

from the system by the loop is plotted in figures 2.3 and 2.4. Figure 2.4 has the subset of particles ejected after 70 y. It can be seen that the particles ejected later during spin evolution have lower speeds.

The particle velocities are plotted after 37.5 y in figures 2.5, 2.6 & 2.7 in the x-y, x-z and y-z projections respectively, and after 160 y in figure 2.8. Figures 2.5 2.6 & 2.7 have had the particles with $r < 1$ removed to avoid swamping the diagrams with the Keplerian velocities of the particles close in. The dotted line in figure 2.8 marks the co-rotation radius and the vector (r_0, θ_0, ϕ_0') is indicated. The simulation was scaled in such a way that 1 unit corresponds to 4.64 AU.

The number of particles ejected, accreted and hit by the loop is plotted in figure 2.9. Comparing this to figure 2.2 provides an insight into the ejection mechanism. At early times, when the spin period is short, virtually all the particles hit by the loop subsequently escape. At this stage the particles are being hit by the loop well outside the co-rotation radius and are consequently given an injection of angular momentum by the star. As the spin period increases towards the equilibrium value more of the particles will have higher velocities than the rotating loop when they interact. These particles will be slowed by the loop and tend to accrete onto the
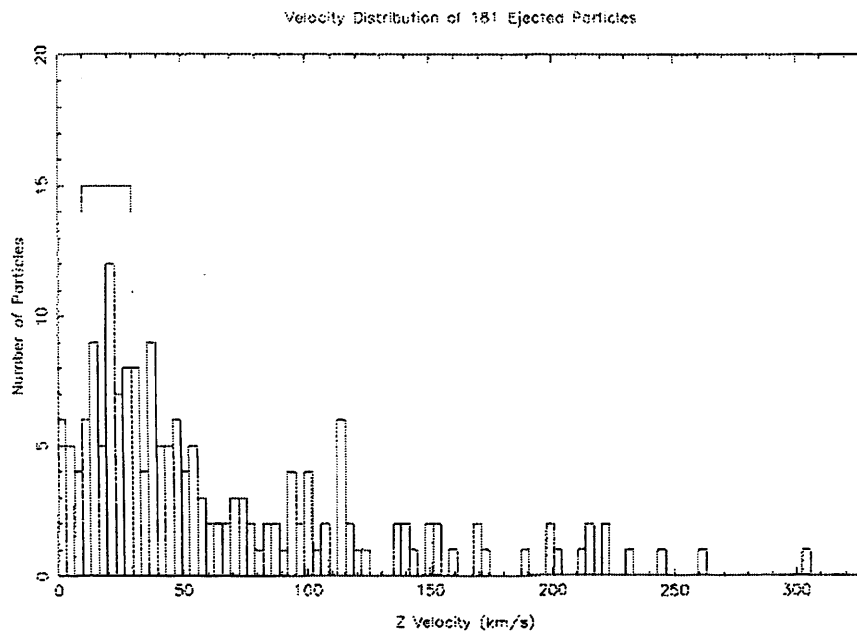
Figure 2.3: The z-velocity histogram for all the particles ejected by the loop during the first simulation.
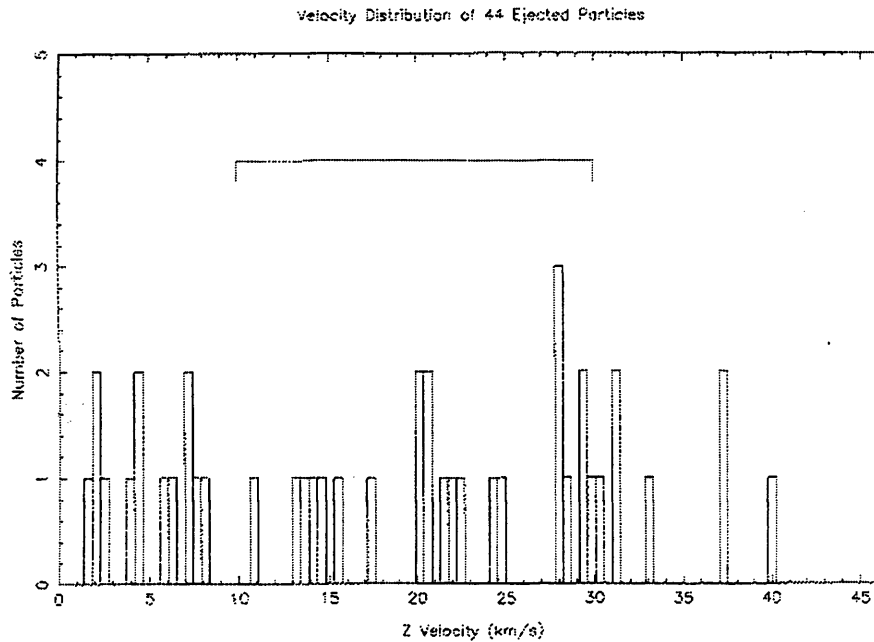

Figure 2.4: The z-velocity histogram for the particles ejected by the loop after 70 y during the first simulation.

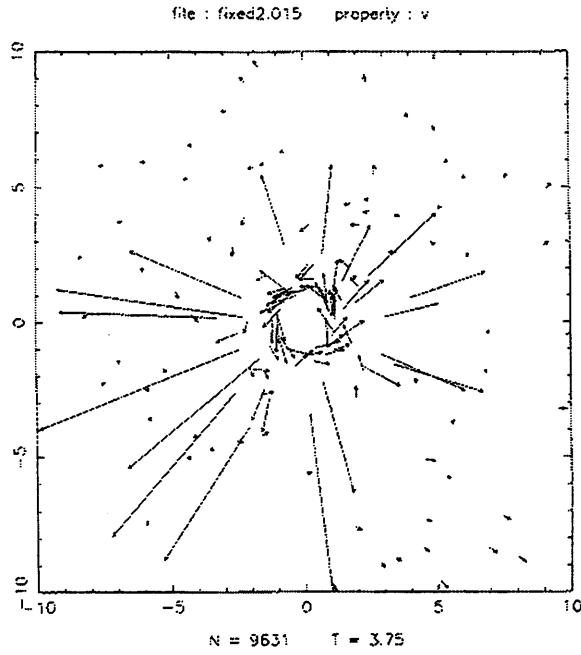file : fixed2.015   property : v

N = 9631   T = 3.75

Figure 2.5: Velocities of particles with $r \geq 1$ in the x-y projection plotted after 37.5 y. The axes are marked in multiples of the dimensionless HyDisc unit equivalent to 4.64 AU. The velocity vectors were all scaled to aid clarity. This scaling factor was kept constant in figures 2.6 & 2.7.
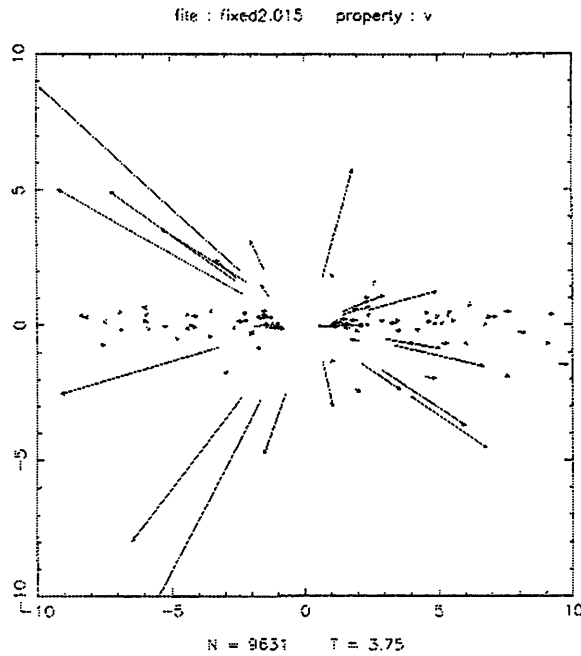
file : fixed2.015   property : v

N = 9631   T = 3.75

Figure 2.6: Velocities of particles with $r \geq 1$ in the x-z projection plotted after 37.5 y.

file : fixed2.015   property : v

N = 9631   T = 3.75
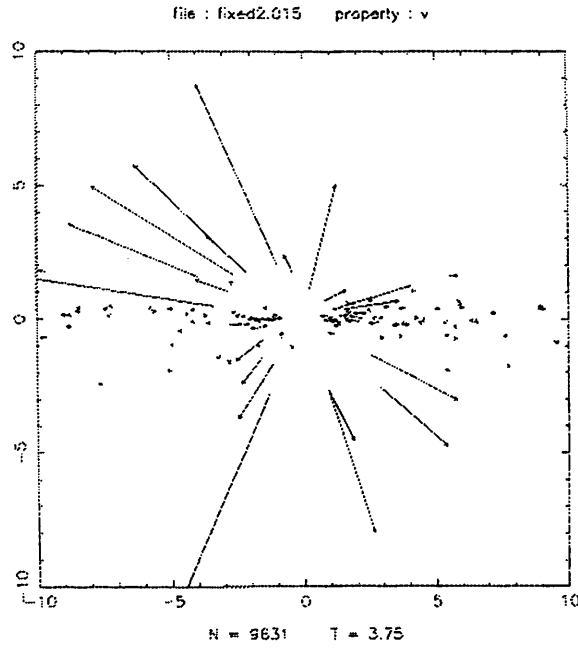
Figure 2.7: Velocities of particles with $r \geq 1$ in the y-z projection plotted after 37.5 y.

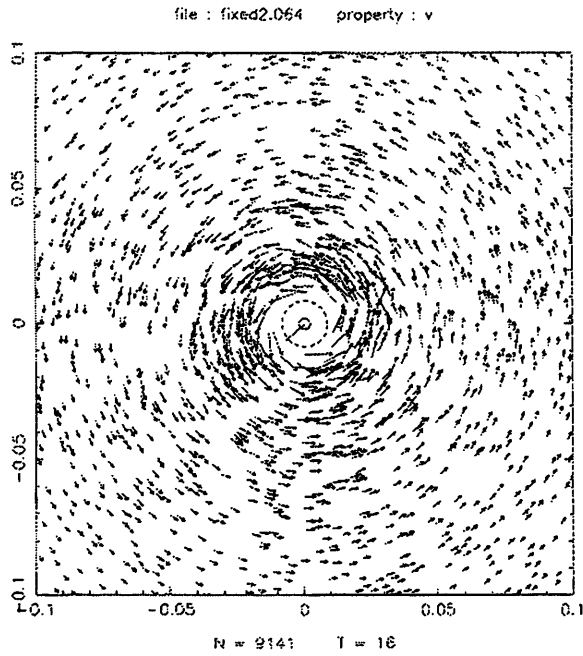file : fixed2.064   property : v

N = 9141   T = 16

Figure 2.8: Velocities of particles in the x-y projection plotted after 160 y. The dotted line shows the corotation radius and the vector (r_0, θ_0, ϕ_0) is marked.

number of particles accreted, escaped and hit by field for star fixed2 — files 001 to 064
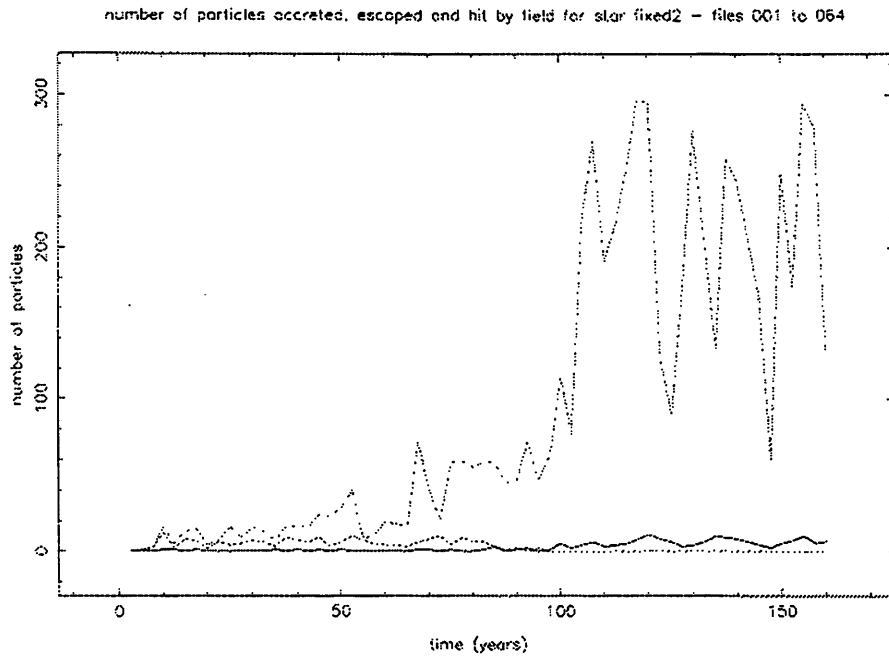

Figure 2.9: The number of particles ejected by the loop (dashed line), accreted (solid) and hit by the loop (dot-dashed) during the first simulation.

central star, increasing its angular momentum. Equilibrium is reached when the angular momentum gained from slowed and accreting particles is balanced by the angular momentum given to slowly moving particles. Clearly this will occur when the spin rate of the star matches the speed of the loop closely to the Keplerian velocity at the outer edge of the loop, ie. when the co-rotation radius is approximately at the edge of the loop. It can be seen from (2.4) that the force on a particle is proportional to the speed of the particle across the field lines. This explains why the particles ejected at later times, when the spin rate is slower, have lower speeds. Figure 2.9 also shows that in the equilibrium state the spin down torque is provided by many small interaction where particles are not gaining enough energy to escape but are being nudged back out into the disc.

To convert from the simulated spin evolution timescale to the real timescale requires a knowledge of the true mass represented by each particle and the effective mass used by HyDisc. This in turn requires a knowledge of the accretion rate at the inner edge of the disc. We assume that the measured values of $\sim 10^{-7}$– 10^{-8} M$_\odot$ y^{-1} (Basri & Bertout 1989) correspond to a system where spin equilibrium has been reached. Consider HyDisc accreting n_{eqm} particles of notional mass M_h over T_{eqm}

years with the moment of inertia of the star reduced by a factor R_{eqm}. If the true accretion rate of the system is $\dot{M}_{acc}$ per year then each HyDisc particle represents a mass of

$$M_{part} = \frac{\dot{M}_{acc} t_{eqm}}{n_{eqm}} \qquad (2.23)$$

where t_{eqm} is the true time over which the simulation is running.

Since HyDisc is using an effective mass for the purposes of the spin calculation of $R_{eqm} M_h$ then the true timescale over which the simulation runs is

$$t_{eqm} = \frac{n_{eqm} R_{eqm} M_h}{\dot{M}_{acc} t_{eqm}} T_{eqm} \qquad (2.24)$$

$$= \left[\frac{n_{eqm} R_{eqm} M_h}{\dot{M}_{acc}} T_{eqm} \right]^{\frac{1}{2}} \qquad (2.25)$$

Now, since the mass represented by each particle is constant, the true timescale over which equilibrium was established (t_{evol}) is

$$t_{evol} = \frac{n_{eqm} R_{evol} M_h}{\dot{M}_{acc} t_{eqm}} T_{evol} \qquad (2.26)$$

which becomes by (2.25)

$$t_{evol} = \left[\frac{n_{eqm} M_h}{\dot{M}_{acc}} \right]^{\frac{1}{2}} \frac{R_{evol}}{R_{eqm}^{\frac{1}{2}}} \frac{T_{evol}}{T_{eqm}^{\frac{1}{2}}} \qquad (2.27)$$

Given $n_{eqm} = 142$, $R_{eqm} = R_{evol} = 5 \times 10^{11}$, $\dot{M}_{acc} = 5 \times 10^{-8}$ M$_\odot$ y^{-1}, $M_h = 10^{15}$ kg, $T_{eqm} = 60$ y and $T_{evol} = 90$ y this yields $t_{evol} = 9.8 \times 10^3$ y.

The mass outflow rate during the evolution phase is given by

$$\dot{M}_{out} = \frac{n_{ej,evol} M_{part}}{t_{evol}} \qquad (2.28)$$

$$= \frac{n_{ej,evol}}{t_{evol}} \left(\frac{\dot{M}_{acc} t_{eqm}}{n_{eqm}} \right) \qquad (2.29)$$

$$= \left(\frac{n_{ej,evol}}{n_{eqm}} \right) \left(\frac{R_{eqm}}{R_{evol}} \right) \left(\frac{T_{eqm}}{T_{evol}} \right) \dot{M}_{acc} \qquad (2.30)$$

from equations (2.25) and (2.26) where $n_{ej,evol} = 181$ is the total number of particles ejected during the evolution phase. With the above parameters this gives $\dot{M}_{out} = 4.3 \times 10^{-8}$ M$_\odot$ y^{-1}.
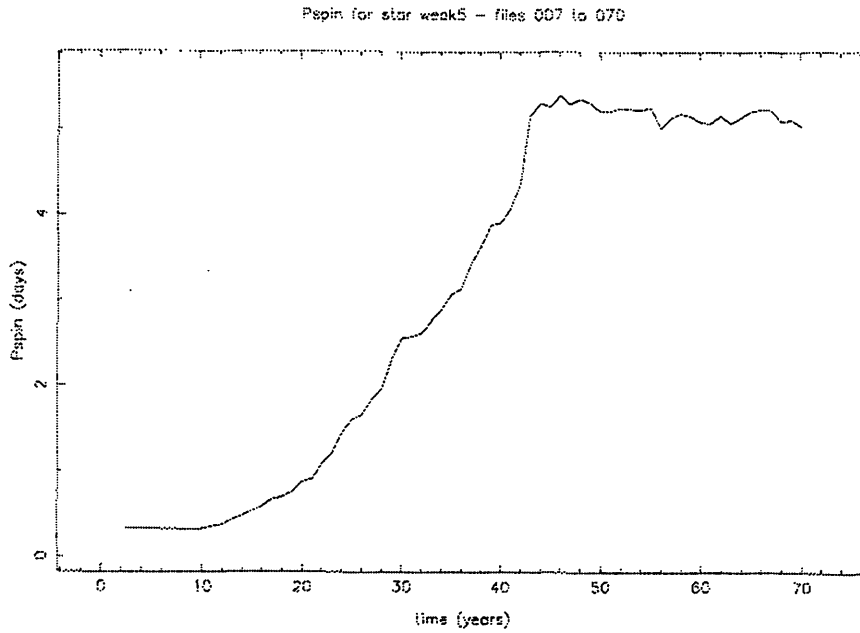
Figure 2.10: A graph of spin period against time for the second HyDisc simulation. The value of R was reduced after 43.6 y.

A second simulation used similar parameters to the first except the loop extended to a height of 6.4 R_* above the T Tauri surface and had a k_0 value of 1.99×10^{-4} s^{-1}. The implied length scale of the blobs is 2.88×10^8 m. The initial spin rate was at the breakup value and the value of R was reduced from 1.0×10^{12} to 2.5×10^{11} after 43.6 years.

The spin-rate is plotted against time in figure 2.10. The equilibrium value is close to the typical value of 5.2 days for a 2 $R_\odot$ T Tauri (Bertout 1989) and compares to the predicted value of 6.60 days. The velocity distribution of the ejected particles is plotted in figure 2.11. Given $n_{ej,evol} = 124$, $n_{eqm} = 84$, $R_{eqm} = 2.5 \times 10^{11}$, $R_{evol} = 1.0 \times 10^{12}$, $T_{eqm} = 24$ y, $T_{evol} = 33$ y we have $t_{evol} = 1.23 \times 10^4$ y and $\dot{M}_{out} = 1.51 \times 10^{-8}$ $M_\odot$ y^{-1}.

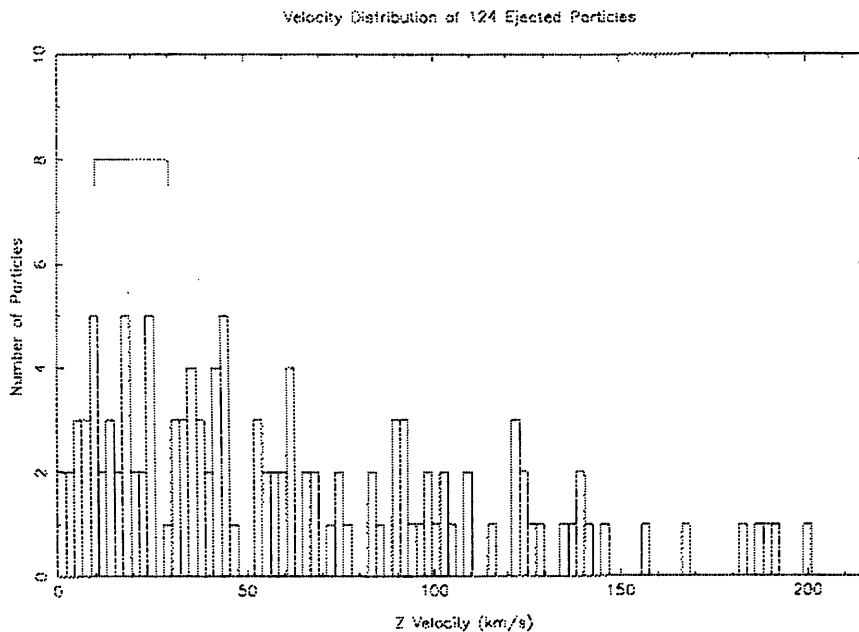Velocity Distribution of 124 Ejected Particles

Figure 2.11: The z-velocity histogram for all the particles ejected by the loop during the second simulation.

2.4 Conclusions

We have shown that the molecular outflows and braking mechanism in YSOs can be explained by a single, simple cause. In this scenario the outflows occur as the result of a magnetic structure rotating at the stellar spin period accelerating material at larger radii to escape speeds. The outflows must be collimated by some mechanism such as a suitable containing cavity (see KR) although this is not an essential part of the model. As a first approximation such a cavity would act to destroy the x and y velocities, then, provided that it is sufficiently wide (~ 0.1 pc), the particles z-velocities are typically an order of magnitude larger than that needed for escape ($V_{esc}(0.1pc) = 0.3$ km s^{-1}). The z-velocities are comparable to, although somewhat larger than, those of the observed outflows. Both of the mass outflow rates are also comparable to those observed although somewhat smaller. We would expect, in reality, the interaction between the outflow and the cavity to be complex; it would not be unreasonable, however, to assume that the entrainment mechanism would both increase the mass in the outflow and decrease its speed, bringing the results into more exact agreement with the observations.

In contrast to KR we find that the ejection of material comes to a halt as the star approaches its equilibrium value. At equilibrium the spin-down torque is provided by a large number of interactions with particles being nudged back into the disc. The timescale for spin-down is somewhat less that for the embedded phase of YSOs. This is consistent with an outflow phenomenon being more typical of Type I YSOs than T Tauris. It would be expected, however, from this model that those T Tauris with outflows should have higher spin rates than those without since these systems will still be at the ejection phase of the spin evolution. Exceptions to this might arise if the supply of material from the disc is exhausted before the star has come to equilibrium.

Whilst we chose parameters for the loop which ensured a significant value of k close to the disc plane, this model is not limited to a special choice of loop parameters. We would expect the central star to possess many loop structures scattered over its surface at any given time, and it is not unreasonable to expect that at least one of these will be sufficiently close to the equator to interact with the disc. More quantitatively, for the parameters used in the simulations the angle subtended in the $\phi = \phi_0'$ plane by the $\frac{k}{k_0} = 0.01$ contour (see figure 2.1) is 0.910 radians. Assuming that the loops are uniformly distributed in latitude this gives a probability for any given loop to cross the disc plane of 0.290. Hence, to be 99% confident that the plane is crossed by at least one loop, we would require $\sim$ 13 loops to be present at any one time.

This mechanism implies that there should be no long-term coherence in the periodicity in the light from these systems (which might be expected were a dipolar field invoked, cf. Cameron & Campbell (1993)) since magnetic loops are transitory and likely to be scattered essentially randomly over the star. However, it does suggest that short-lived periodicities with timescales of days or weeks might be present. As the loops are created and destroyed the phase and amplitude of the light curve will change, but the period of the light curve will remain unchanged (the timescale of any spin evolution being long). Such short-term variations are observed and generally

ascribed to photospheric spots (Bouvier & Bertout 1989); this is evidence that stellar activity is indeed present. The bright spot observed on the young star DF Tauri (Bouvier & Bertout 1989) might be explained if material was being channelled to the foot-points of a loop.

A more thorough investigation could include a detailed description of the magnetic loop field geometry. It could also focus on young Type I YSOs and follow the collapse of the cloud core, the consequent spin-up being counteracted by ejection via rotating magnetic structures.

Chapter 3

The Implications of the Secondary's Magnetic Field for Dwarf Novae

3.1 Introduction

The most widely accepted model for DN outbursts is the disc instability model. In this model the mass transfer rate from the secondary is taken to be constant and the amount of material in the accretion disc gradually increases over time. It can be shown (eg. Meyer & Meyer-Hofmeister 1981; Cannizzo 1993) that at a critical surface density the disc becomes unstable and deposits a large amount of material on the WD in a sudden burst. This deposition of material occurs fairly regularly and although the time between outbursts is not constant, the mean recurrence time is a stable quantity for a given system.

In a recent paper Meyer-Hofmeister, Vogt and Meyer (1996, hereafter MVM) considered the effect that the presence of a magnetic field on the secondary star would have on the outburst behaviour of dwarf novae in the context of the disc instability

model. They added a term to the equations governing the disc in a standard outburst code. No structure was assumed for the field (which was assumed to be the result of magnetic activity on the secondary) and its strength was described solely by a mean field "at the position of the disc". They suggested that observed periodicities in the the recurrence time of SS Cygni and SS Aurigae could be explained by the changing strength of the secondary's field as it exhibited magnetic cycles.

Clearly one would like to lift the restriction to a mean field. Accordingly, similar systems have been modelled in three dimensions with versions of HyDisc. The interaction has been modelled in two ways. In the first, the material is assumed to be broken up into the form of blobs which interact diamagnetically with the magnetic field. In the second the disc material is allowed to drag the magnetic field out of its initially dipolar configuration and the effect on the motion of the magnetic tension (see equation (1.37)) is examined.

MVM gave a brief review of the evidence for the presence of magnetic field on the secondary some of which is summarised below along with evidence from other sources.

From the theoretical viewpoint the presence of a secondary magnetic field is necessary to supply the magnetic braking of the secondary, generally accepted as a driving mechanism for the orbital evolution of CVs above the period gap (Verbunt & Zwaan 1981; Mestel & Spruit 1987). A significant secondary field is also necessary in order to lock the primary in synchronous rotation in polar systems.

Observational evidence for magnetic secondaries has come from several sources. Maceroni *et al.* (1990) discuss evidence for the presence of magnetic fields in a wide variety of binary systems. Studies of the pre-CV V471 Tau (Applegate & Patterson 1987) have yielded direct evidence for the presence of star spots (and by implication a reasonably strong secondary field). There are also indications for the presence of a magnetic field in Algol (Ottmann 1994) and also from radio emissions in EM Cyg. Bianchini (1990) discusses the evidence for the presence of solar-type activity cycles in the secondary stars in CVs, as do Baliunas & Vaughn (1985) and Baliunas (1990).

Such activity cycles would also indicate the presence of a significant secondary field. Typical estimates of the surface field strength of $B \sim 0.1$ T (Marcy 1984) give rise to magnetic moments $\mu \sim 10^{30}$–10^{31} A m^2 (King, Frank & Whitehurst 1990).

3.2 The Simulations – The 'Blob' Model

These simulations tackle the problem with a different approach from MVM. Whereas their code solved the equations for the disc structure as a whole HyDisc is a particle code which follows the individual motions of particles which make up the disc. This makes it prohibitively time-consuming to attempt to model in detail the formation and gradual evolution of the disc between outbursts, given that the system would need to be modelled the over several hundred orbital periods. Further, it can be shown that for a reasonable viscosity prescription for a disc the code should be run with a grid size which ensures roughly one particle per cell. Given that HYDISC has a fixed choice of grid size for any given simulation and the amount of material in the disc increases this condition would clearly be violated (this could be remedied by using a code with an adaptive grid). As a result we cannot give a quantitative description of the effect that the field has on the recurrence time. Instead the blob model has been applied to the system in two situations. In order to demonstrate the effect of the magnetic field on the recurrence time the system was modelled with a constant overflow rate but a choice of grid size which gave an artificially high viscosity. This causes the disc to evolve more rapidly, enabling us to determine qualitatively the effect of a magnetic secondary on the recurrence time. The system has also been modelled with a configuration close to that at outburst by injecting a large initial burst of particles. The true ratio of overflow rate to disc mass is uncertain. Hence, simulations have been conducted where the initial burst rapidly decays to a small overflow rate, appropriate to a ratio of overflow rate to disc mass which assumes no accretion or other losses from the disc. In this situation, once the disc has formed we can examine the effect on the disc dynamics and energy dissipation patterns of the field and any observational consequences.

HyDisc does have the advantage of enabling us to specify relatively easily a detailed magnetic field structure. In this situation the dipole axis has been chosen to coincide with the spin axis although this choice is arbitrary. Doppler tomograms can also be produced from the data which may be compared with observation.

3.2.1 Transformations for a Rotating Dipole

In order to calculate the drag force for an arbitrarily oriented, rotating, three-dimensional dipolar field we require the field strength and direction at any point. We can determine these by first choosing a convenient coordinate frame in which to calculate the field strength and direction. We then transform the coordinates of the particle into this frame and calculate the required quantities. We can then transform the fieldline vector back to the original HyDisc frame.

Consider a Cartesian frame (x_p, y_p, z_p) such that the z_p-axis lies along the magnetic axis and the x_p-axis is chosen so that the particle lies in the x_p-z_p plane. The fieldline on which the particle lies is therefore also contained in the x_p-z_p plane. We can thus determine the local field direction

$$\hat{\mathbf{b}}_p = \hat{\mathbf{y}}_p \wedge \frac{\nabla f}{|\nabla f|} \tag{3.1}$$

where

$$f = \frac{r}{\sin^2 \theta} = \frac{(x_p^2 + z_p^2)^{\frac{3}{2}}}{x_p^2} \tag{3.2}$$

is a function whose level surfaces are the field lines. Combining (3.1) and (3.2) we have the components of the field direction

$$\hat{\mathbf{b}}_p = \frac{1}{\left[\left(\frac{3r}{x_p} - \frac{2r^3}{x_p^3}\right)^2 + \left(\frac{3r z_p}{x_p^2}\right)^2\right]^{\frac{1}{2}}} \begin{pmatrix} \frac{3r z_p}{x_p^2} \\ 0 \\ \frac{2r^3}{x_p^3} - \frac{3r}{x_p} \end{pmatrix} \tag{3.3}$$

where r is the distance of the particle from the origin.

In order to convert from the HyDisc coordinate system described in section 1.4.2 we first translate the origin from the WD to the centre of the secondary. The particle

coordinates are now

$$
\mathbf{s} \equiv \begin{pmatrix} x_s \\ y \\ z \end{pmatrix} = \begin{pmatrix} x+1 \\ y \\ z \end{pmatrix}. \tag{3.4}
$$

We will now transform to the (x_p, y_p, z_p) frame via three rotations about a coordinate axis. Firstly we rotate about the z-axis by the angle $\phi = \phi_0 + \omega_b t$, where ω_b is the rotation frequency of the star as measured in the rotating frame, to the frame (x_{dp}, y_{dp}, z_{dp}) such that the magnetic pole lies in the $x_{dp} > 0$, $z_{dp} > 0$ quadrant of the x_{dp}-z_{dp} plane. The new coordinates may be expressed as

$$
\begin{pmatrix} x_{dp} \\ y_{dp} \\ z_{dp} \end{pmatrix} = \begin{pmatrix} \cos\phi & \sin\phi & 0 \\ -\sin\phi & \cos\phi & 0 \\ 0 & 0 & 1 \end{pmatrix} \begin{pmatrix} x_s \\ y \\ z \end{pmatrix}. \tag{3.5}
$$

From this system we rotate about the y_{dp}-axis by the angle m, the co-latitude of the magnetic pole, to the coordinate frame (x_D, y_D, z_D) such that the z_D-axis lies along the magnetic axis. A similar transformation matrix to (3.5) will determine the new coordinates

$$
\begin{pmatrix} x_D \\ y_D \\ z_D \end{pmatrix} = \begin{pmatrix} \cos m & 0 & -\sin m \\ 0 & 1 & 0 \\ \sin m & 0 & \cos m \end{pmatrix} \begin{pmatrix} x_{dp} \\ y_{dp} \\ z_{dp} \end{pmatrix}. \tag{3.6}
$$

Finally, we rotate about the z_D-axis by the angle θ_p to the (x_p, y_p, z_p) frame where the particle lies in the x_p-z_p plane. These coordinates may be expressed as

$$
\begin{pmatrix} x_p \\ y_p \\ z_p \end{pmatrix} = \begin{pmatrix} \cos\theta_p & \sin\theta_p & 0 \\ -\sin\theta_p & \cos\theta_p & 0 \\ 0 & 0 & 1 \end{pmatrix} \begin{pmatrix} x_D \\ y_D \\ z_D \end{pmatrix} \tag{3.7}
$$

where we can determine θ_p from

$$
\cos\theta_p = \frac{x_D}{r_{\mathrm{ax}}} \tag{3.8}
$$

$$
\sin\theta_p = \frac{y_D}{r_{\mathrm{ax}}} \tag{3.9}
$$

$$
r_{\mathrm{ax}} = (x_D^2 + y_D^2)^{\frac{1}{2}}. \tag{3.10}
$$

Expressions for x_D and y_D can be determined from (3.5) and (3.6)

$$x_D = (x_s \cos\phi + y \sin\phi)\cos m - z \sin m \qquad (3.11)$$

$$y_D = y \cos\phi - x_s \sin\phi. \qquad (3.12)$$

We can now derive the transformation matrix T such that

$$\hat{\mathbf{b}}_p = T\,\hat{\mathbf{b}} \qquad (3.13)$$

by combining equations (3.5), (3.6) and (3.7). This gives

$$T = \begin{pmatrix} \cos\phi\cos m\cos\theta_p & \sin\phi\cos m\cos\theta_p & -\sin m\cos\theta_p \\ -\sin\phi\sin\theta_p & +\cos\phi\sin\theta_p & \\ & & \\ -\cos\phi\cos m\sin\theta_p & -\sin\phi\cos m\sin\theta_p & \sin m\sin\theta_p \\ -\sin\phi\cos\theta_p & +\cos\phi\cos\theta_p & \\ & & \\ \cos\phi\sin m & \sin\phi\sin m & \cos m \end{pmatrix}. \qquad (3.14)$$

This matrix also allows us to transform s into the new frame so that we can calculate the field strength at the particle's position. Now that we have the elements of T we can transform $\hat{\mathbf{b}}_p$ back to the HyDisc frame by calculating the inverse matrix T^{-1} via the standard equation

$$T^{-1} = \frac{\text{adj}T}{\Delta T}. \qquad (3.15)$$

When implemented in HyDisc the following procedure was adopted for determining k and $\hat{\mathbf{b}}$. Firstly, x_D and y_D were calculated via (3.11) and (3.12) enabling $\cos\theta_p$ and $\sin\theta_p$ to be determined via (3.8), (3.9) and (3.10). With all the elements of T now known the position of the particle with respect to the secondary star was transformed to the (x_p, y_p, z_p) frame and the field strength determined from the standard dipole formula

$$B = B_s \left(\frac{R_2}{s}\right)^3 \left(1 + 3\left(\frac{z_p}{s}\right)^2\right)^{\frac{1}{2}}. \qquad (3.16)$$

where B_s is the surface field of the secondary at the magnetic equator and R_2 is the radius of the secondary. The local field direction given by (3.3) was then transformed back to the HyDisc frame using T^{-1} whose components were calculated from (3.15).

3.2.2 Application to U Gem

The simulations were carried out with parameters appropriate to U Geminorum with $M_1 = 1.26 M_\odot$, $M_2 = 0.581 M_\odot$ and $P_{\rm orb} = 4.25^{\rm h}$ (Ritter & Kolb 1995). The magnetic simulations were carried out with $k \propto B$ at each point in the dipole field and a value at L_1 of $k_{\rm s} = 4.11 \times 10^{-5} {\rm s}^{-1}$. From (2.1) we have

$$B^2 = \left(\frac{\mu_0}{4\pi}\right) \frac{m c_{\rm A} k}{l^2}. \tag{3.17}$$

Assuming a spherical blob of constant density

$$m \sim \rho l^3 \tag{3.18}$$

so (3.17) becomes

$$B^2 \sim \left(\frac{\mu_0}{4\pi}\right) \rho l c_{\rm A} k. \tag{3.19}$$

If we set $l \sim H$, the scale height of the disc, and use

$$c_{\rm A} = \frac{B}{(\mu_0 \rho)^{\frac{1}{2}}} \tag{3.20}$$

the relation becomes

$$B \sim \frac{(H\rho^{\frac{1}{2}})\mu_0^{\frac{1}{2}}}{(4\pi)} k. \tag{3.21}$$

From thin disc theory (eg. Frank, King and Raine 1992) we have

$$H\rho^{\frac{1}{2}} = (9.46 \times 10^3)\alpha^{-\frac{9}{20}} \dot{M}_{13}^{\frac{17}{40}} M_1^{-\frac{1}{16}} R_8^{\frac{3}{16}} f^{\frac{17}{10}} \; {\rm kg}^{\frac{1}{2}} \; {\rm m}^{-\frac{1}{2}} \tag{3.22}$$

where α is the Shakura-Sunyaev viscosity parameter, $\dot{M}_{13}$ is the mass transfer rate in units of 10^{13} kg s^{-1}, M_1 is measured in solar masses, R_8 is the distance from the primary in units of 10^8m and f is a function which is close to unity in this context. Combining (3.21) and (3.22) and assuming $\dot{M} = 10^{14.1}$ kg s^{-1} (MVM), $\alpha = 0.1$ and a disc radius $R_{\rm d} = 0.125a$ (see figure 3.4) we can deduce the field strength at

Trace of blob tracks

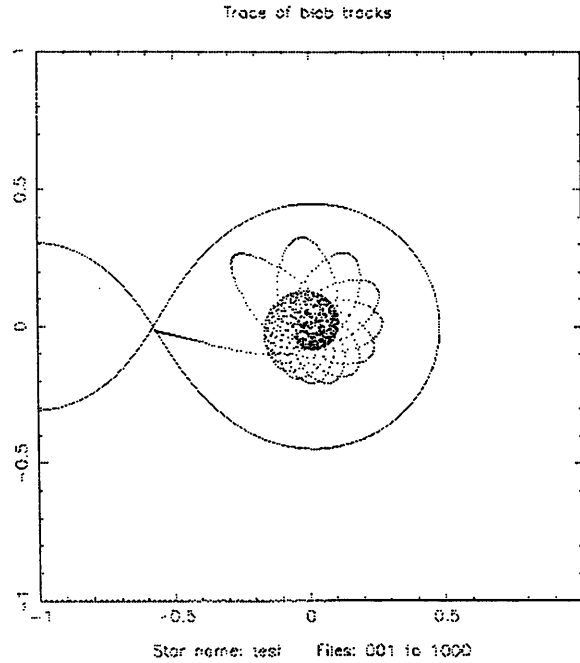Star name: test   Files: 001 to 1000

Figure 3.1: A single particle simulation showing the effect of the magnetic field in gradually removing energy from the particle orbit. The axes are marked in binary separations and the WD at the origin and the primary's Roche lobe are also plotted.

the edge of the disc along the line of centres to be 3.02×10^{-4} T. The magnetic moment of the secondary star is thus $\sim 3 \times 10^{30}$ A m^2. This is a fairly reasonable field strength for the secondary. The weak dependence of (3.22) on R shows that k does in fact deviate slightly from the dependence implied by a true dipole but the error introduced is negligible.

The effect of the secondary's field was first examined for single particles. Figure 3.1 shows the particle track when the code was run with the U Gem parameters. The effect of the magnetic field is clear as the orbiting particle gradually loses energy and moves to smaller orbits and is eventually accreted by the WD. The stronger the field the more rapidly the particle loses energy and is accreted.

To investigate the effect on the recurrence time the code was run with a constant mass transfer rate of 300 particles per period and a disc was allowed to form gradually. The resulting density profile of the discs at different stages of the evolution can be seen in figure 3.2. The dotted line marks the critical surface density at which the disc becomes unstable. It can be seen that the effect of the magnetic field has been to
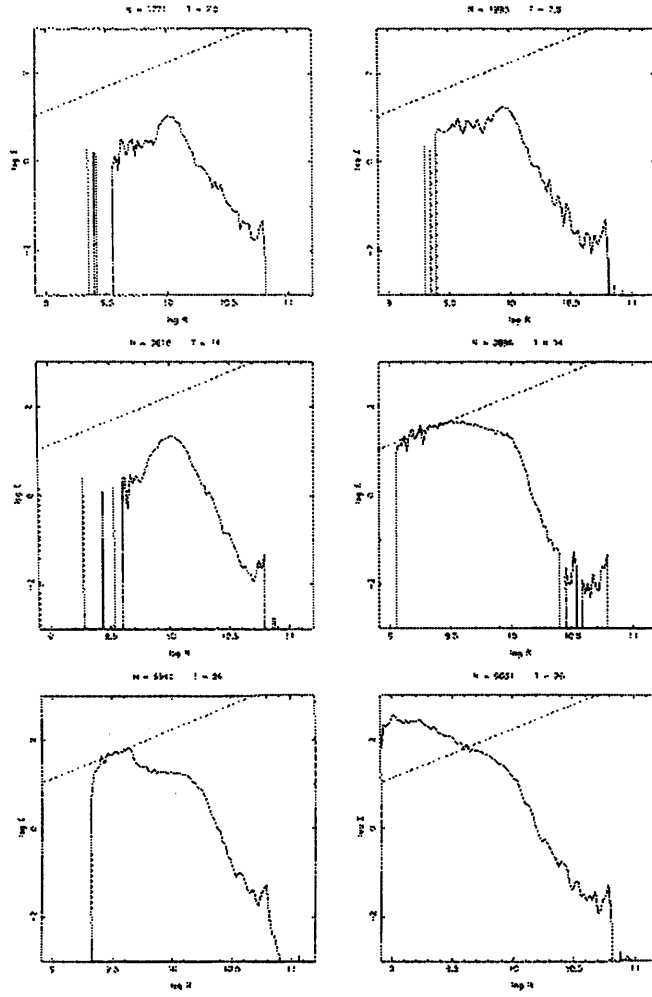
Figure 3.2: A log-log plot of the surface density against radius for the simulations (non-magnetic on the left) after 7.5, 14 and 26 orbital periods. The dotted line marks the critical surface density above which the disc becomes unstable and an outburst will result.

make the disc more centrally condensed. This causes the disc to reach the instability line more quickly, confirming the results of MVM.

In order to simulate the system close to outburst the code was run with an initial short burst of high mass transfer creating a disc containing ~ 10000 particles. The mass transfer rate was then decreased to give a recurrence time of 118^d assuming no mass loss from the system (Ritter & Kolb 1995) (ie. $10000 \times \frac{4.25^h}{188^d} \approx 15$ particles per period). The viscous dissipation pattern in the disc (figures 3.3&3.4), the pattern of energy dissipated by the magnetic drag (figure 3.5) and Doppler tomograms (figure 3.6&3.7) have all been plotted for the simulations.
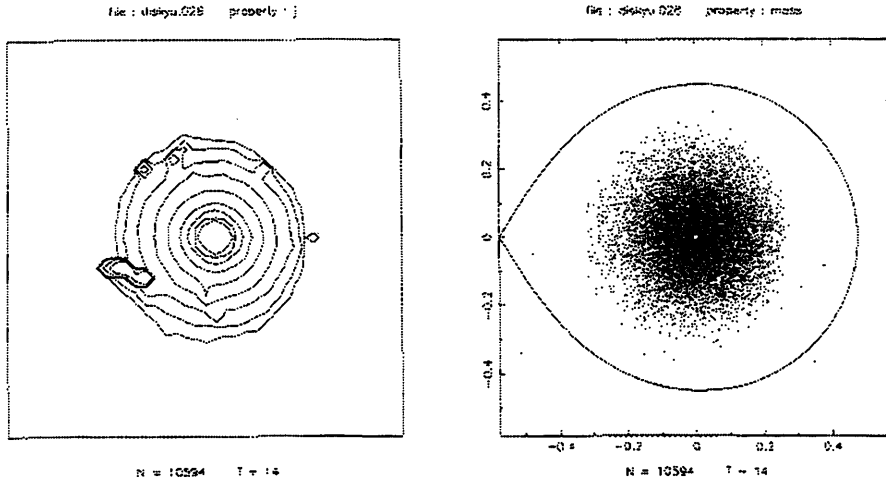
Figure 3.3: A contour plot (the contour levels following a logarithmic progression) of the energy dissipated by viscosity in the non-magnetic simulation after 14 orbital periods with the mass distribution for comparison.
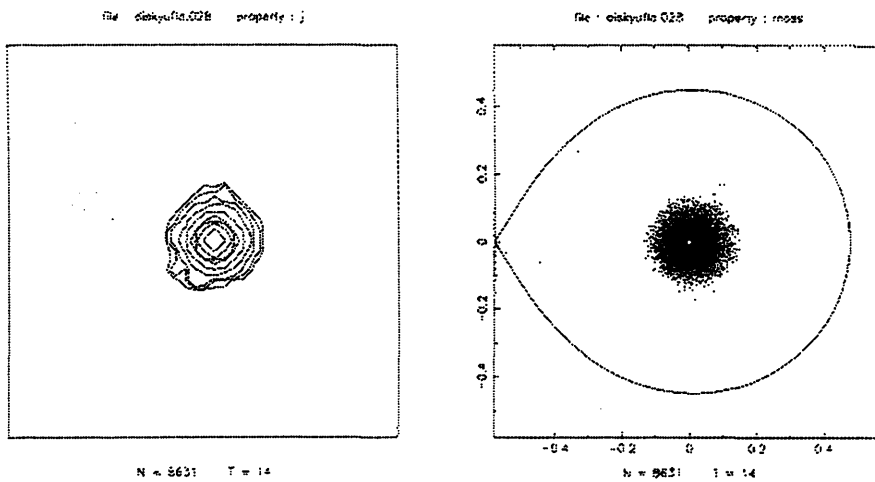

Figure 3.4: A contour plot of the energy dissipated by viscosity in the magnetic simulation after 14 orbital periods with the mass distribution for comparison.
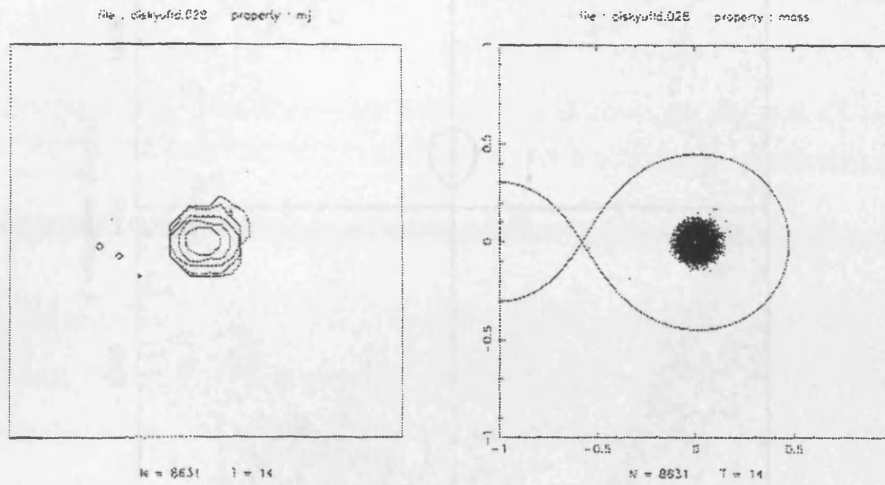
Figure 3.5: A contour plot of the energy dissipated by the magnetic drag force in the magnetic simulation after 14 orbital periods with the mass distribution for comparison.
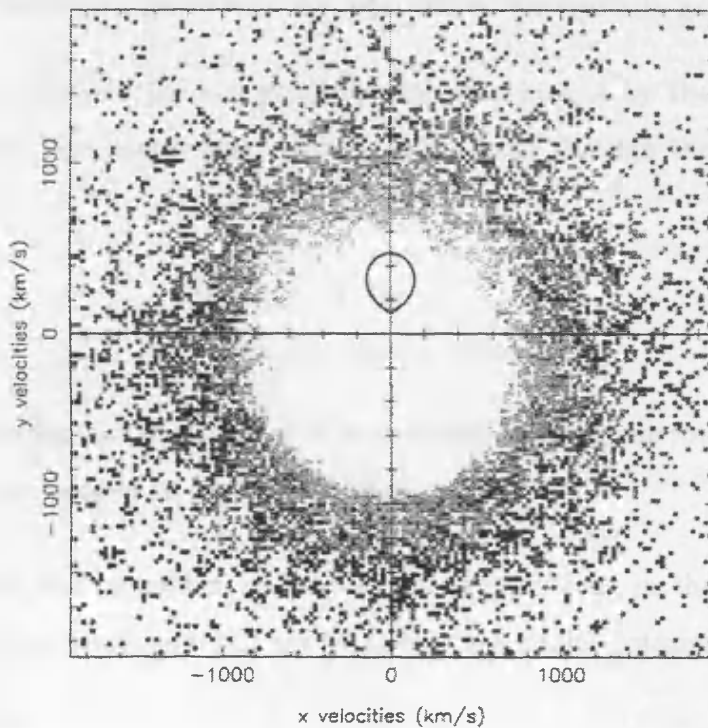
Figure 3.6: Doppler tomogram of the non-magnetic simulation assuming an inclination of 69.7° (Ritter and Kolb 1995) with the particle positions weighted by the mean energy dissipated per particle in the local cell of the viscosity grid. The stream is not visible as the discrete nature of the simulations has become apparent there.
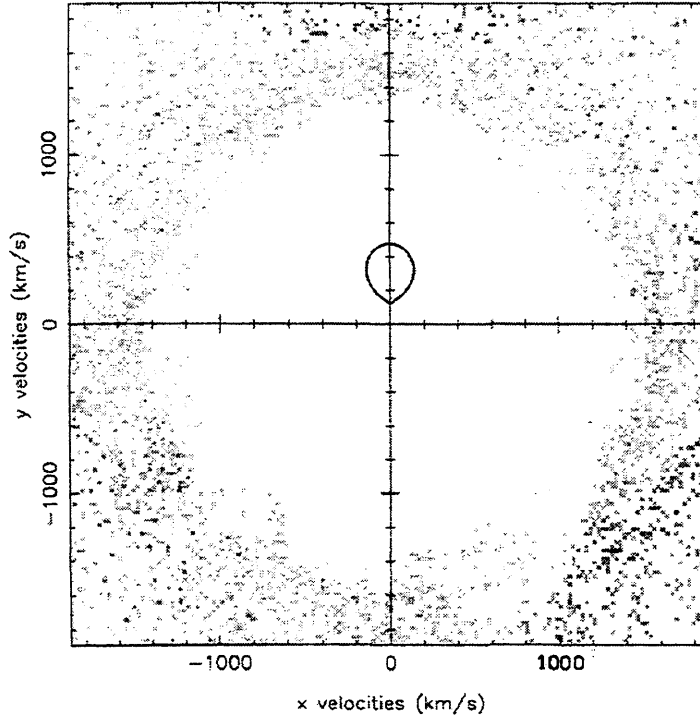
Figure 3.7: Doppler tomogram of the magnetic simulation weighted by the mean energy dissipated per particle in the local cell of the viscosity grid.

In order to calculate the energy dissipation rate caused by the magnetic field we consider, first, the energy lost by the particle orbit through the work done by the drag force,

$$\dot{E}_{\text{part}} = \mathbf{F}.\mathbf{v}_{\text{in}} \tag{3.23}$$

$$= -mk(\mathbf{v} - (\mathbf{v}.\hat{\mathbf{b}})\hat{\mathbf{b}}).\mathbf{v}_{\text{in}} \tag{3.24}$$

where it is important to note that $\mathbf{v}$ is measured in the frame rotating with the field and $\mathbf{v}_{\text{in}}$ is the velocity in the inertial frame.

If we restrict our attention initially to particle motions in the orbital plane the reaction on the secondary will try to change the stellar rotation about the z-axis. Then with

$$E_2 = \frac{1}{2}I\omega_z^2 \tag{3.25}$$

we have

$$\dot{E}_2 = I\omega_z\dot{\omega}_z \tag{3.26}$$

$$= \omega_z T_z \tag{3.27}$$

where,

$$T_z = (\mathbf{r} \wedge \mathbf{F})_z \tag{3.28}$$

is the torque exerted by the particle on the secondary about the rotation axis. The energy dissipated by the interaction is then the sum of (3.24) and (3.27) summed for all particles. Similar equations to (3.27) exist for rotation about the other axes but given $\omega_x = \omega_y = 0$ we are justified in neglecting these terms.

The crude estimate of $\dot{M}$ to M_{disc} almost certainly overestimates the mass in the disc as some material will inevitably have accreted by the primary or been swept up by the secondary star. This will give rise to too few particles in the stream and a consequent overestimate of the mass represented by each particle. This will in turn produce an overestimate of the energy dissipation rates. In order to overcome this we have normalised the dissipation rates so that the non-magnetic simulation has a typical quiescent DN Luminosity of 10^{25} W. The total energy dissipation rate after 14 orbital periods for the magnetic simulation was 7.6×10^{25} W from viscous interactions and 1.13×10^{25} W from the magnetic drag. The magnetic drag force dissipated more energy in the disc than did the viscosity in the non-magnetic simulation, and dissipation due to viscosity in the magnetic simulation is close to an order of magnitude greater. The fact that the disc in the magnetic simulations is smaller but contains a similar amount of mass to the non-magnetic case is a result of the higher viscous dissipation rate.

3.3 The Simulations – The Restricted MHD Model

In the treatment of the previous section we have assumed that the material everywhere is broken up into 'blobs'. This is very likely to be true for material in the stream which has just left the L_1 point. It is less likely, however, once the material reaches the disc as the blobs may well amalgamate with the material already there and lose their identity. In this situation a more appropriate treatment might be to

apply equation (1.37) to the motion. In order to use this we specify a fixed, but distorted, field shape.

Following the approach of MVM the interaction is assumed to occur through bending of the magnetic fieldlines by the disc material. The important component of equation (1.37) is the magnetic tension which will act to oppose the azimuthal motion with a force density

$$\mathbf{f} = \frac{1}{R}\left(\frac{B^2}{\mu_0}\right)\mathbf{e}_\phi \tag{3.29}$$

As the gas orbits the WD it will drag the magnetic fieldlines with it until $B_\phi \sim B_z$ (Aly & Kuijpers 1990; Wang 1996) when instabilities induce reconnection events. If we assume that the fieldlines bend in the region of the disc plane where the field is weak we can make the approximation $R \sim H$.

Since the particles represent mass elements of gas we can write the acceleration due to the magnetic tension (3.29) as

$$\mathbf{a} = \frac{\mathbf{F}}{m} = -\frac{B^2}{\mu_0 H \rho}\hat{\mathbf{e}}_\phi. \tag{3.30}$$

It is clear that this requires a knowledge of the density in the region of the particle. This can be deduced from the particle distribution. If we assume that azimuthal symmetry is a good approximation we can write

$$\rho(R) = \frac{N m_\mathrm{p}}{2\pi R \Delta R H(R)} \tag{3.31}$$

where N is the number of particles in a bin of width ΔR at a distance R from the white dwarf and m_p is the mass associated with each particle. If this equation was used directly with the particle distribution it is possible that sharp fluctuations in the potential could occur because of the discrete nature of the particles. This was avoided by regularly performing a spline fit to the profiles every $t_\mathrm{visc} \sim 0.02$ periods. Examination of (3.30) and (3.31) shows that the most poorly-known quantity H conveniently cancels from the acceleration. Since we know the spatial variation of B, it is also apparent that each simulation can now be characterised by the magnetic field strength at the L_1 point and the particle mass m_p, through the ratio $\frac{B_{L_1}^2}{m_\mathrm{p}}$. Since we do not know accurately either the mass of the disc or the ratio of the mass

overflow rate to disc mass we cannot specify m_p *a priori.* However, since m_p does not appear elsewhere in the equations of motion, it is possible to determine m_p and hence B for each set of simulations by normalising the energy dissipation rate to a value determined from observations. Equations (3.30) and (3.31) were added to the long-range equations of motion.

As the particle moves through the magnetic field of the secondary it will again gradually lose energy. As before the energy dissipation rate is given by the rate of working of the magnetic tension

$$\dot{E}_{\text{part}} = \mathbf{F}.\mathbf{v} \qquad (3.32)$$

where we can calculate $\mathbf{F}$ from (3.30) and (3.31) and $\mathbf{v}$ is the velocity with respect to the field. As we have implicitly assumed that the field is always on the point of reconnection any torque by the disc material on the field lines will immediately result in a reconnection event. The reaction on the secondary's rotation of this interaction is therefore negligible. This malleable, reconnecting field contrasts sharply with the rigid field used in the blob models. The true interaction must lie somewhere between these two extremes.

Rather than show again the effect on the recurrence time of the removal of angular momentum by the field, the simulations carried out using this method were in the configuration close to outburst.

3.3.1   U Gem

Simulations were carried out with the same parameters appropriate to U Gem used above.

Simulations were run in the absence of any secondary field and with $\frac{B_{Li}^2}{m_p}$ of 1.95×10^{-18} T^2 kg^{-1} and 1.95×10^{-20} T^2 kg^{-1}. Figure 3.8 shows the density contours for the simulations whilst the positions of the particles are plotted in figure 3.9. The viscous dissipation pattern in the disc (figure 3.10) and the pattern of energy dissipated by
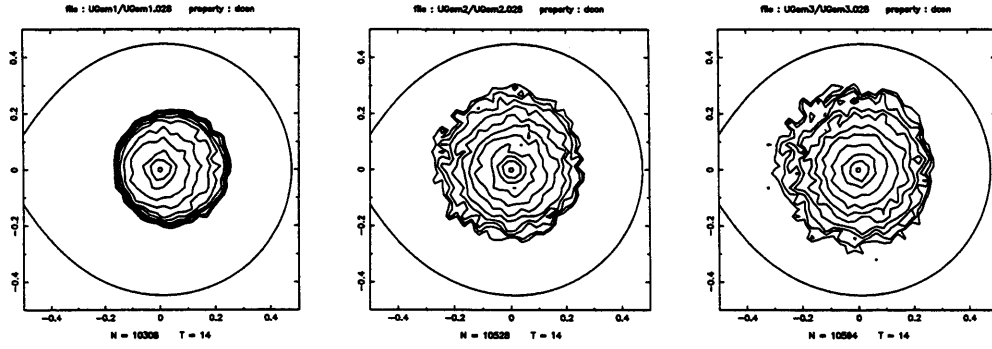
Figure 3.8: Contour plots of the particle density for the high-field (left), low-field (centre) and non-magnetic (right) simulations of U Gem. The contours are scaled logarithmically from the peak in each diagram. Subsequent three panel plots will maintain the same plotting order.
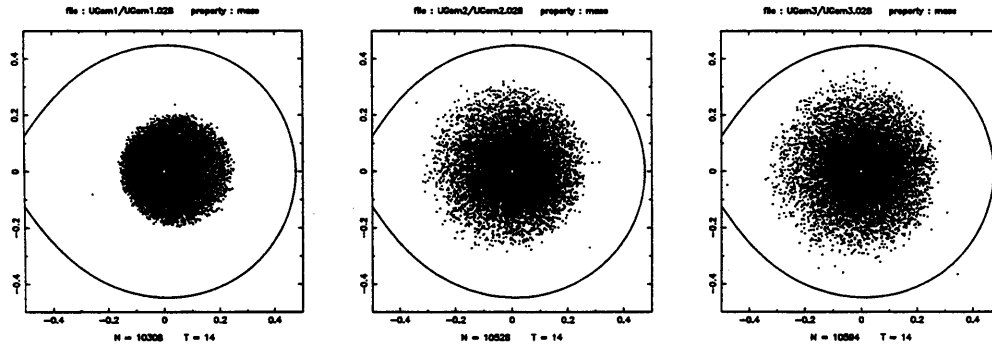

Figure 3.9: A plot of the particle positions for the three simulations of U Gem.

the magnetic interaction (figure 3.11) have been plotted for the simulations. In all the figures the simulation ran for 14 periods. Doppler tomograms (figure 3.12) have also been produced from the simulations. We can derive the expected disc luminosity from equation (1.4).

Using the same mass transfer rate $10^{14.1}$ kg s^{-1} for U Gem as MVM gives 1.30×10^{27} W. Normalising the viscous energy dissipation rate of the non-magnetic simulation to this value determined $m_p = 1.31 \times 10^{16}$ kg. The magnetic simulations were thus carried out with secondary magnetic field strengths of $B_{L1} = 0.16$ T ($\mu_2 \approx 1.7 \times 10^{32}$ A m^2) and $B_{L1} = 0.016$ T ($\mu_2 \approx 1.7 \times 10^{31}$ A m^2). The 0.16 T simulation dissipated 1.81×10^{27} W from viscous interactions and 4.28×10^{26} W from magnetic. The 0.016 T simulation dissipated 1.16×10^{27} W from viscous interactions and 6.13×10^{26} W from magnetic. Again these values were calculated after the simulation had run for 14 periods. The magnetic dissipation from the 0.16 T
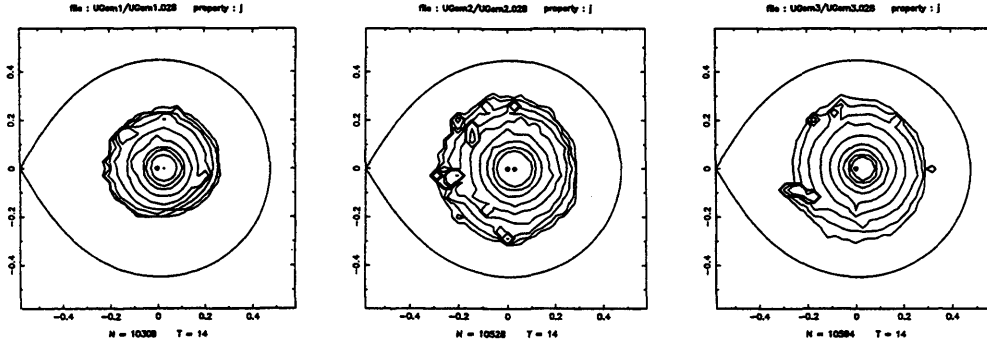
Figure 3.10: A contour plot (the contour levels following a logarithmic progression) of the energy dissipated by viscosity in the U Gem simulations during the previous 0.5 orbital periods.
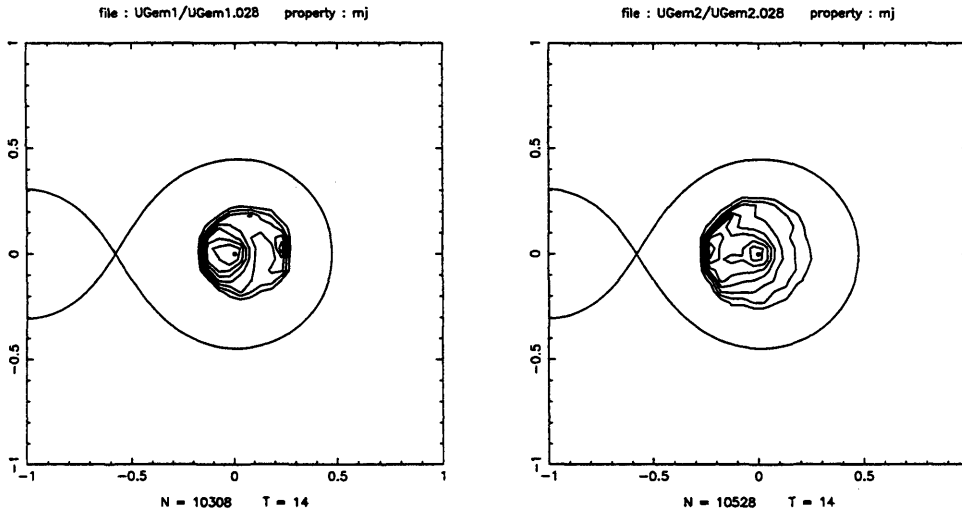
Figure 3.11: A contour plot of the magnetic dissipation in the previous 0.5 orbital periods for the magnetic U Gem simulations (the high-field on the left). The contour levels are scaled linearly from the peak value.

Figure 3.12: Simulated tomograms for the three simulations of U Gem. The magnetic simulations are plotted after 14.4 periods and the non-magnetic after 14.5. The secondary's Roche lobe is indicated along with the position of the WD.

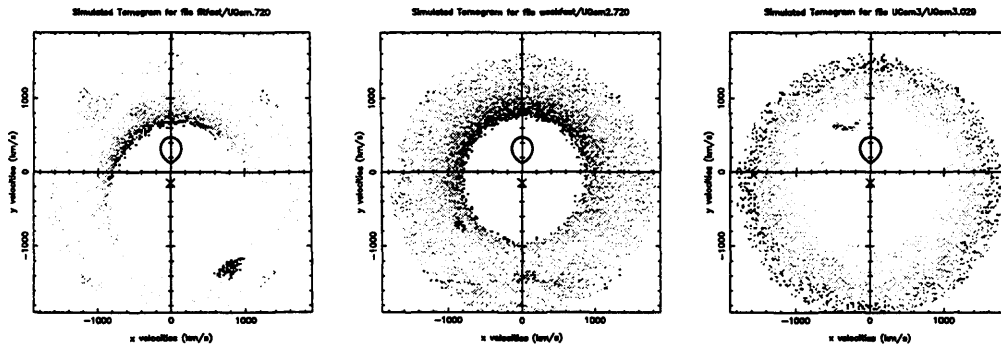simulation is less than that for the 0.016 T simulation. Examination of the plot of magnetic dissipation versus time in figures 3.16&3.17 shows that the higher field simulation has a larger variation. Both simulations are close to the minimum phase of magnetic dissipation, so that the high field simulation dissipates less energy via magnetic interactions at this instant.

3.3.2   Z Cha

The members of the SU UMa group of DN, with a single exception, all lie below the period gap. In addition to the usual DN outbursts, these systems show super-outbursts where the outburst luminosity is typically ~ 0.7 mag greater than usual and which last ~ 5–10 times longer. During superoutbursts these systems also show a photometric modulation at a period a few percent longer than the orbit, known as the superhump period. For any given system the time between superoutbursts is fairly regular, but the number of ordinary outbursts between superoutbursts can vary widely. The explanation for superhumps relies on the formation of tidal resonances in the disc (Whitehurst 1988a). These arise when material in orbits in the disc receive regular injections of energy from the orbital passage of the secondary. If the motion of the secondary past the disc material occurs at the same phase of the material orbits the disc can be driven eccentric. This is discussed in detail by a number of authors (e.g. Frank, King & Raine 1992; Warner 1995). The resonance condition requires a sufficiently large disc radius. In the SU UMa systems the disc radius allows the 3:2 resonance (3:1 orbital commensurability) to be excited. The eccentricity of the disc gives rise to modulations of the light curve on the beat period between the orbit and the (long) precession period of the disc. The period of these superhumps can be calculated theoretically (Hirose & Osaki 1990) and is in reasonable agreement with observations. If, however, these systems posses significant magnetic fields the mechanism described by MVM may shrink the disc such that the observed resonance condition cannot hold. These systems thus provide an important observational constraint on this model.
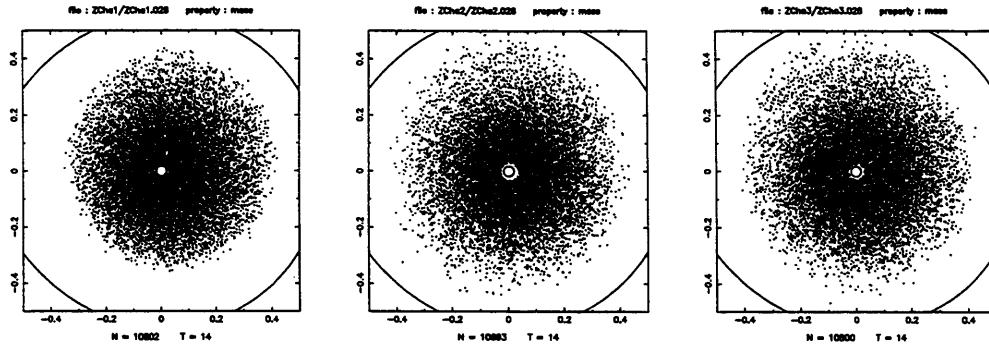
Figure 3.13: Plots of the particle positions for the high-field (left), low-field (centre) and non-magnetic (right) simulations of Z Cha. The 4:3 resonance has begun to appear in the high-field simulation. The usual 3:2 SU UMa resonance is not yet apparent in the other simulations.

Further simulations were carried out with parameters appropriate to Z Cha with $M_1 = 0.84 M_\odot$, $M_2 = 0.125 M_\odot$ and $P_{orb} = 1.788^h$ (Ritter & Kolb 1995) adding 9 particles per period. Again simulations were carried out without a magnetic field and with $\frac{B_{L_1}^2}{m_p}$ of 2.77×10^{-18} T^2 kg^{-1} and 2.77×10^{-20} T^2 kg^{-1}. The positions of the particles in the simulations are plotted in figure 3.13. The viscous dissipation patterns are plotted in figure 3.14 and the magnetic dissipation in figure 3.15. Using a mass transfer rate of 2×10^{12} kg s^{-1} (Warner 1995) gives an expected disc luminosity of 1.20×10^{25} W. Again normalising the dissipation rate in the non-magnetic simulations to this value we determined $m_p = 1.95 \times 10^{14}$ kg. The magnetic simulations were thus carried out with magnetic field strengths of 2.3×10^{-2} T ($\mu_2 \approx 9.8 \times 10^{29}$ A m^2) and 2.3×10^{-3} T ($\mu_2 \approx 9.8 \times 10^{28}$ A m^2) at the L_1 point. The 2.3×10^{-2} T simulation dissipated 1.55×10^{25} W from viscous interactions and 5.15×10^{24} W from magnetic. The 2.3×10^{-3} T simulation dissipated 1.38×10^{25} W from viscous interactions and 5.02×10^{22} W from magnetic. Since the superhump phenomena is a strong constraint on models of Z Cha tomograms are not presented for this systems.

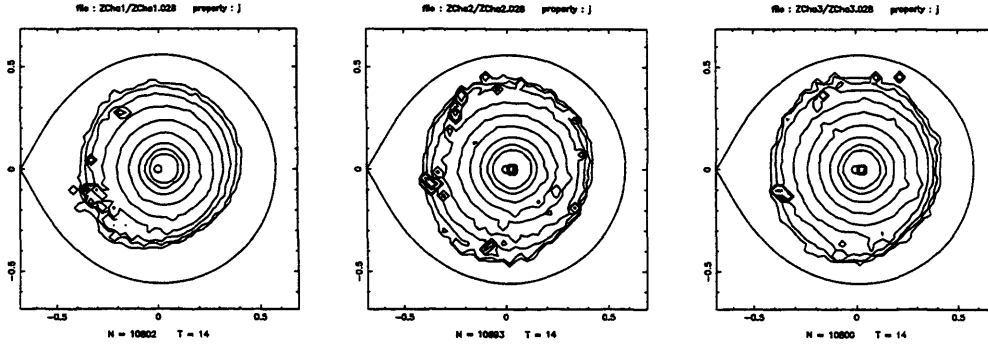Figure 3.14: A contour plot (the contour levels following a logarithmic progression) of the energy dissipated by viscosity in the Z Cha simulations during the previous 0.5 orbital periods.
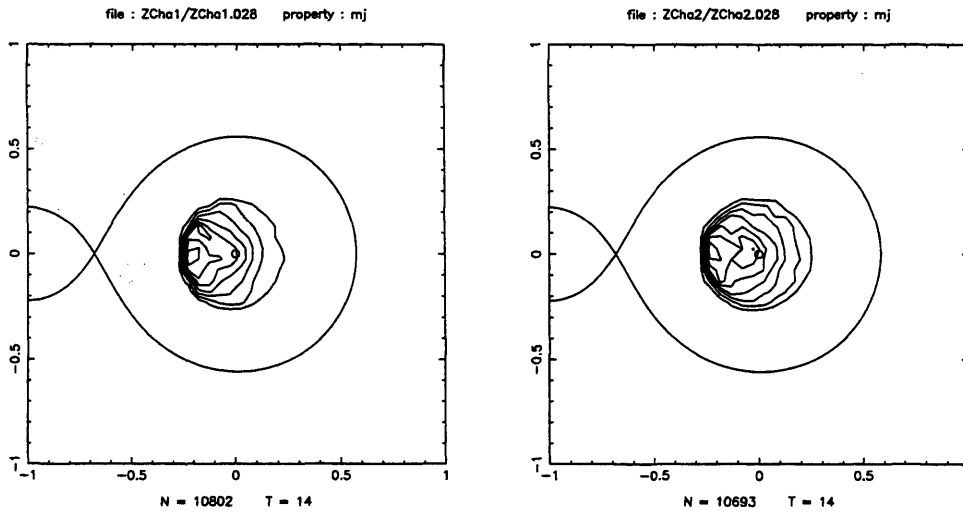

Figure 3.15: A contour plot of the magnetic dissipation in the previous 0.5 orbital periods for the magnetic Z Cha simulations (the high-field on the left). The contour levels are scaled linearly from the peak value.

3.4 Discussion

3.4.1 The 'Blob' model

The bright spot in the non-magnetic simulation is clearly visible in the outer regions of the disc. The more condensed nature of the magnetic simulations means that the stream does not impact on the disc with a large angle between the velocity vectors of the stream and disc material. This greatly reduces the amount of energy dissipated at the interface and makes the bright spot undetectable.

The Doppler tomograms of the two simulations are significantly different. The stream in the simulated tomograms is not visible. This arises from the discrete nature of the particles becoming apparent with such a low number of particles being injected per period. This leads to much less viscous interaction in the stream than would be expected. Once the material reaches the disc, however, this problem is resolved. The much smaller disc in the magnetic case means that the ring in velocity space has an inner edge at higher velocity. Comparing this tomograms with those observed by Marsh *et al.* (1990), we find that the non-magnetic case bears a much closer resemblance to the observations. Given that in MVM no cycles in the recurrence time were observed for U Geminorum this is not entirely unexpected. However, it does lead to the conclusion that either the secondary in this system has a peculiarly low magnetic field or else some other mechanism is preventing the magnetic field of the secondary from influencing the disc. In the other two systems considered by MVM: SS Cygni and SS Aurigae, cycles in the recurrence time were detected. If the proposal that this periodicity is produced by the magnetic cycle of the secondary star is indeed correct, tomograms of these systems should be markedly different from those produced by an undisturbed disc. It would be possible to confirm this by comparing tomograms of these systems during their long and short recurrence time phases.

The dwarf novae in the atlas of tomograms for CVs of Kaitchuck *et al.* (1994) do

not show the marked clearing of the centre of the tomogram that would be expected if the magnetic field were exerting an influence on it in this way. This suggests that this effect on the recurrence time is likely to be limited a subset of systems.

While we have allowed the magnetic field to interact with the whole disc, it is possible that the field only interacts with the outer regions of the disc. This may occur if, for example, the blobs lose their identity and amalgamate once in the disc. Alternatively, it is possible that the disc material acts to screen much of the disc from the field. If this scenario, or indeed any other coupling of the secondary's field to the disc is to produce the periodic recurrence times however, it will still need to condense the disc into a smaller volume with similar implications for the Doppler tomograms. As mentioned in the previous section, the disc material is probably only sufficiently inhomogeneous for the 'blob' model to be applicable in the accretion stream. However, it is interesting to compare the results which are obtained from a MHD approach with those of the blob model.

3.4.2   The Restricted MHD Model

U Gem

From figure 3.8 it is apparent that the magnetic field has resulted in a disc with an eccentric shape. This is very reminiscent of the superhump phenomena observed in SU UMa systems. However, the orbital radius for the 3:2 resonance excited by tidal interaction with the secondary in these systems lies outside the radius of the disc in U Gem. This suggests that the effect of the magnetic interaction has been to excite a higher resonance which is usually inaccessible. This is very reasonable as the strong radial dependence of the magnetic stresses ($f \propto r^{-6}$) must imply a resonant interaction with the disc orbits. The mean radius of various resonant orbits can be shown (e.g. Frank, King and Raine 1992) to be given by

$$\frac{R_{jk}}{a} = \left(\frac{j-k}{j}\right)^{\frac{2}{3}} (1+q)^{-\frac{1}{3}} \tag{3.33}$$

Resonance $j : k$	R_{jk} (separations)	Precession Period (orbital periods)
3:2	0.424	13.1
4:3	0.350	17.6
5:4	0.301	22.1
6:5	0.267	26.5
7:6	0.241	30.8
8:7	0.220	35.2
9:8	0.204	39.5

Table 3.1: Mean radii and theoretical precession periods of various resonant orbits for U Gem with $q = 0.461$

where q is the mass ratio of the binary and a is the separation. The radii of various resonances for U Gem parameters is given in table 1 along with predicted disc precession periods following the method of Hirose & Osaki (1990) and Warner (1995). It should be noted that these resonances are expected to be strongest for $k = j - 1$. Determining the nature of the excited resonance in each simulation is not easy since the mean radii of resonant orbits crowd closer together at higher orders. Notwithstanding this, estimates of the disc radii from figure 3.9 suggest that in the 0.016 T simulation the 6:5 resonance has been excited whereas in the 0.16 T simulation the resonance could be as high as 9:8.

The magnetic dissipation is highly concentrated in the part of the disc closest to the secondary. As the secondary passes the long axis of the disc on the beat period between the disc precession period and the orbital period, we would expect more energy to be dissipated. This will give rise to a variation in the magnetic dissipation on this period (analogous to the superhump period in SU UMa systems). The energy dissipated by the magnetic and viscous interactions and the total dissipation are plotted in figures 3.16&3.17. The total dissipation corresponds to the light curve which would be observed from a low-inclination system. Not included in the light curve is the effect of the bright spot variation. This will occur close to anti-phase with the magnetic dissipation, as the bright spot will dissipate more energy when the stream impacts on the disc along its short axis. This effect, however, is likely to be relatively slight. For higher-inclination systems aspect effects such
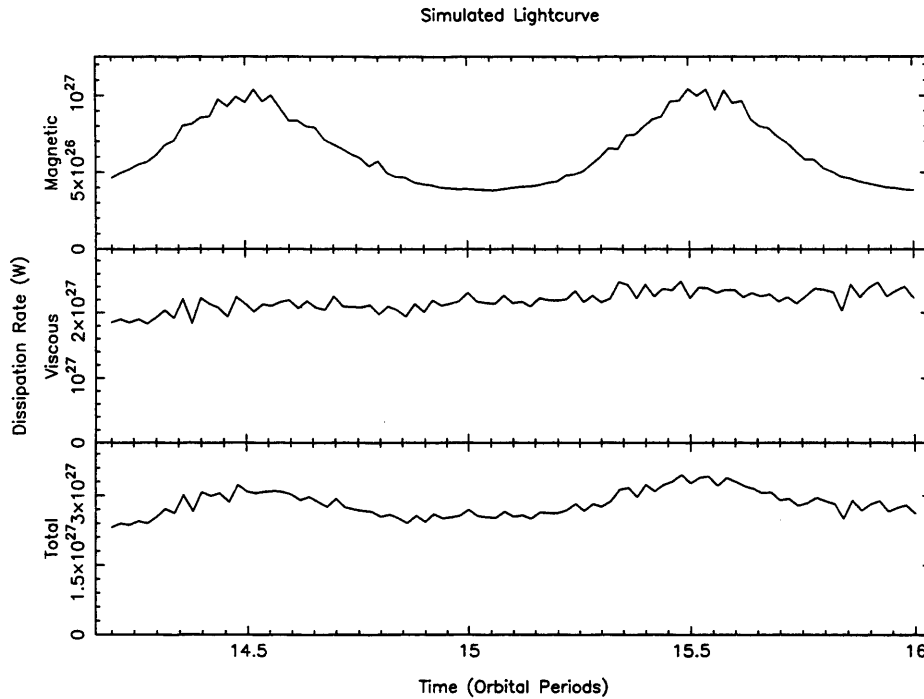
Simulated Lightcurve

Figure 3.16: A simulated lightcurve produced from the high-field magnetic simulation of U Gem. The panels show the magnetic dissipation (top), viscous dissipation (centre) and their total (bottom) plotted against time.

as shadowing of the bright spot by the disc would need to be included. The non-detection of modulations on this superhump period allows us to place a constraint on the magnetic moment of the secondary which will be discussed below.

The bright spot in the non-magnetic simulation is clearly visible in the outer regions of the disc. The more condensed nature of the disc in the magnetic simulations again leads to a reduction in the amount of energy dissipated at the disc-stream interface. The magnetic resistance to the motion of the disc elements is also greater in the part of the disc closest to the secondary. This is apparent from the magnetic dissipation rate shown in figure 3.11. The slowing of the motion on this part of the orbit gives rise to the extra viscous dissipation and the knotty structure apparent in the viscous dissipation for the magnetic simulations in figure 3.10. The eccentricity of the disc causes the radius at which the bright spot appears to vary on the superhump period. As the viscous dissipation is sum over the previous 0.5 orbital periods there will be a slight smearing effect which will tend to reduce the visibility of the bright spot.

The Doppler tomograms of the simulations are also significantly different from each
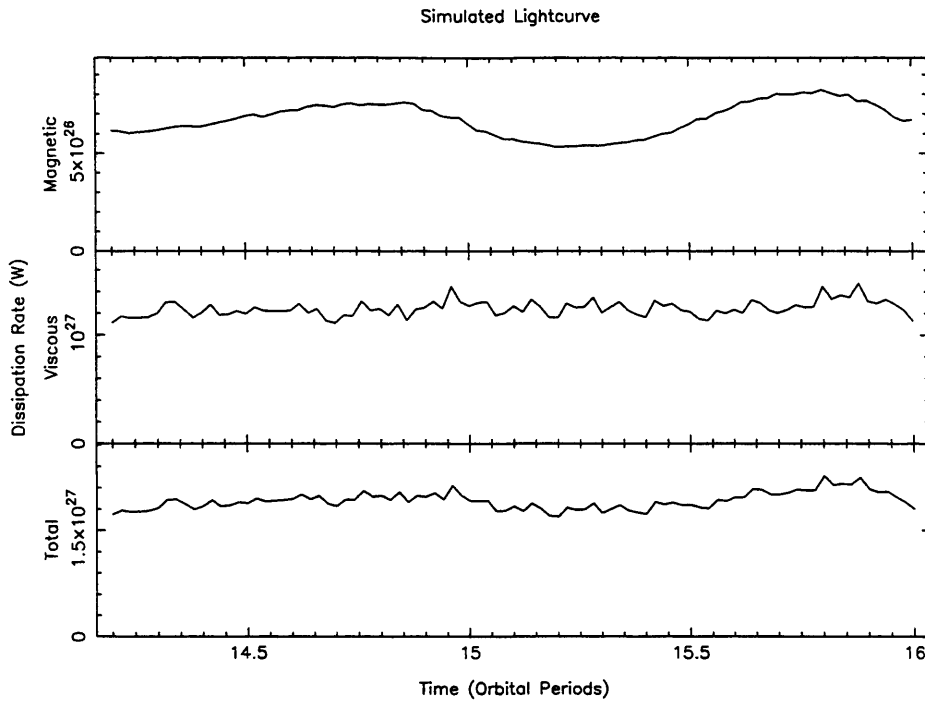
Simulated Lightcurve

Figure 3.17: A simulated lightcurve produced from the low-field magnetic simulation of U Gem.

other. These have been derived from the individual particle velocities in the simulation weighted by the total viscous and magnetic energy dissipation rate. In our simulated tomograms the stream is again not visible. This occurs because the mass in the stream is much less than that in the disc, as a result of the initial assumption of no losses from the disc. The relatively diffuse stream is, however, unlikely to have any significant effect on the disc dynamics. The much smaller disc in the strongly magnetic case gives a ring in velocity space with an inner edge at higher velocity. The asymmetry of the magnetically interacting discs is also apparent in the tomograms. The tomogram from the 0.16 T simulation shows a significant enhancement from the localised magnetic dissipation close to the secondary. This dissipation stands out significantly from the rest of the disc. The peak in the lower right quadrant is caused by a brief knot of viscous dissipation in the simulation and is not a general feature. The 0.016 T simulation produces a tomogram where the localised magnetic dissipation is not as dominant. There is, however, still a significant contribution to the tomogram from the disc material closest to the secondary. The only asymmetry apparent in the tomogram from the non-magnetic simulation is caused by the bright spot where the stream impacts on the disc material.

Comparing the tomograms with those observed by Marsh *et al.* (1990) and in the atlas of tomograms for CVs of Kaitchuck *et al.* (1994) we see again that the observations do not show the marked clearing of the centre of the tomogram that would be expected if the magnetic field were exerting an influence on it. This may be an effect of the limited resolution available to the observations. However, these and other authors (eg. Steeghs *et al.* 1996) do remark that the observed tomograms show asymmetries. These would arise from eccentric discs.

Z Cha

The possibility of exciting higher resonances in the discs of dwarf novae raises an important question for the SU UMa systems. The 3:2 resonance fits the superhump periods observed in these systems well. If the secondaries in these systems (which are all below the period gap) possess similar magnetic moments to those inferred for the secondaries in polars, the resultant shrinking of the disc might result in the 3:2 resonance being no longer available.

The disc in the $B_{L1} = 2.3 \times 10^{-2}$ T magnetic simulation has again been condensed to a smaller radius. The mean radius of this disc is less than $R_{32} = 0.459a$ but close to $R_{43} = 0.379a$. The fact that the resonance is now 4:3 can be confirmed from the precession period of the disc axis. Figure 3.18 shows the number of particles with $r > 0.3a$ plotted against azimuthal angle at various times in a co-ordinate system with an origin at the WD but a fixed orientation in the inertial frame. From these plots we can determine the precession period of the disc as $P_d \approx 2$ d for the non-magnetic and low field simulations and $P_d \approx 3$ d for the high field simulation. These compare to the theoretical periods of 2.19 d for the 3:2 resonance and 3.04 d calculated for the 4:3 resonance. The period deduced from the superhump and orbital periods of 2.0 d (Warner 1995) allows us to place an upper limit on $\mu_2 < 1 \times 10^{30}$ A m^2 for Z Cha.
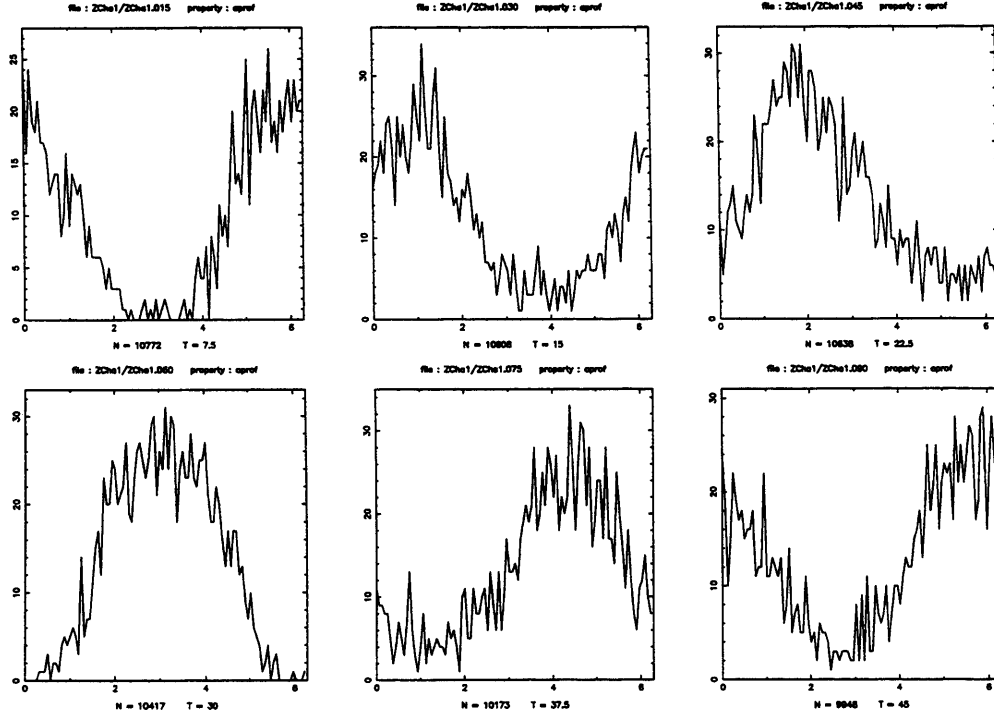
Figure 3.18: A plot of the number of particles with $r > 0.3a$ plotted against azimuthal angle at various times for the high-field simulation.

3.5 Conclusions

The fact that several authors have noted that DN tomograms appear to be asymmetric is potential support for the eccentric discs which appear in the restricted MHD simulations with significant secondary fields. The possibility of higher-order disc resonances in DN above the period gap could potentially be confirmed by photometry of these systems. However, even for the 6:5 resonance the disc precession period $P_d \approx 26.5 P_{orb}$. This implies that for U Gem the precession period is of the order of five days. The modulation of the light curves on the superhump period caused by the changing magnetic dissipation could have gone undetected if the secondary's magnetic moment $\mu_2 \lesssim 2 \times 10^{31}$ A m^2. The strong field simulation $\mu_2 \sim 2 \times 10^{32}$ A m^2 thus represents an upper limit to the magnetic moment of the secondary in U Gem. However, the typical field values considered by MVM would almost certainly produce a noticeable effect. The fact that these modulations are not observed argues against the strong field values $\mu_2 \sim 5 \times 10^{32}$ A m^2 which these authors considered. Even with the weaker fields which our simulations suggest, it may still be possible

to produce the variation in the recurrence time which these authors sought to explain. The weakest field MVM considered corresponded to a surface field of 0.25 T, which approximately halved the the recurrence time in their simulations. This is a dramatic effect which indeed appears excessively large compared to the observed variation in recurrence times for SS Aur. It may thus be possible to reconcile a secondary magnetic moment of $\mu_2 \sim 2 \times 10^{31}$ A m^2 with the required shortening of DN recurrence times.

It is interesting to note that the limit on the magnetic moment of the secondary star in Z Cha is at the lower end of that inferred from the locking condition of polar systems (King, Frank & Whitehurst 1990).

The blob and restricted MHD models have produced similar results despite the fundamental differences in their approaches. Both have resulted in a shrinking of the accretion disc and shortening of the recurrence time for reasonable secondary fields. The differences between the two sets of results can be ascribed to the difference in the radial dependence of the two force laws. The blob model, with its assumption of the inter-blob density following thin disc theory applied $f \propto B \propto r^{-3}$ whereas the restricted MHD approach applied $f \propto B^2 \propto r^{-6}$. This results in a lower field strength at L_1 in the blob approach have a more dramatic effect in shrinking the disc. Similarly, the shallower field strength profile in the blob model does not introduce a sufficient asymmetry into the potential to excite resonances in the disc. This similarity enables us to proceed with confidence with the simulations in chapter 5.

Chapter 4

The Evolution of Magnetic Cataclysmic Variables

4.1 Introduction

To describe a CV as magnetic is something of a tautology since, as we shall see below, the evolution of most CVs at some stage in their lifetimes is likely to depend on the magnetic field of the secondary star. The term magnetic CV is used to distinguish those CVs where the WD field is strong enough to play a significant role in the structure and evolution of the binary or in the dynamics of the accretion process. These systems are split into the high field 'polar' (or AM Her) systems and the lower field 'intermediate polars'. The fields in the polar systems are such that the primary and secondary stars are both held in synchronous rotation with the orbit. In this chapter we shall discuss the currently accepted general evolution of CVs and the particular case of how the polar systems come to be synchronous. We shall examine some of the outstanding problems in polar evolution and outline a model which attempts to address some of these.

In section 1.2 we outlined the structure and formation of CVs in general. In the

remainder of this section we shall examine the current understanding of CV evolution and the consequences of the mass transfer process.

The orbital angular momentum of a binary system is given by

$$J = (M_1 a_1^2 + M_2 a_2^2) M_\odot \omega \tag{4.1}$$

where the symbols have the same meanings as in section 1.2 and

$$a_1 = \frac{M_2}{M_1 + M_2} a \equiv \frac{M_2}{M} a \tag{4.2}$$

$$a_2 = \frac{M_1}{M} a \tag{4.3}$$

are the distances of each star from the centre of mass. Combining these three equations with (1.10) gives

$$J = M_1 M_2 \left(\frac{Ga}{M}\right)^{\frac{1}{2}} M_\odot^{\frac{3}{2}}. \tag{4.4}$$

Assuming $\dot{M}_1 + \dot{M}_2 = 0$, which is usually a good approximation, we can take the logarithm of (4.4) and differentiate to get

$$\frac{\dot{a}}{a} = \frac{2\dot{J}}{J} + \frac{2(-\dot{M}_2)}{M_2}\left(1 - \frac{M_2}{M_1}\right). \tag{4.5}$$

Under conservative mass transfer as well as the assumption of conservation of binary mass above, the total binary angular momentum is taken to be constant. Setting $\dot{J} = 0$ and noting that $\dot{M}_2 < 0$ it can be seen that the binary separation will increase if conservative mass transfer occurs from the less massive to the more massive component. This comes about as the transferred material is placed closer to the centre of mass by this process; consequently the remaining mass M_2 must move further away to compensate.

If we take equation (1.14) and substitute $q = \frac{M_2}{M_1}$ we can again take the logarithm and differentiate to get

$$\frac{\dot{R}_2}{R_2} = \frac{\dot{a}}{a} + \frac{\dot{M}_2}{3M_2} \tag{4.6}$$

which describes the response of the secondary's Roche lobe to the change in the mass of the secondary and the consequent change in separation. If we combine this

with (4.5) we have

$$\frac{\dot{R_2}}{R_2} = \frac{2\dot{J}}{J} + \frac{2(-\dot{M_2})}{M_2}\left(\frac{5}{6} - \frac{M_2}{M_1}\right). \tag{4.7}$$

From the terms in the final bracket we can see that two cases arise depending on whether $q > \frac{5}{6}$ or not. If $q > \frac{5}{6}$ then conservative mass transfer will cause the secondary's Roche lobe to shrink. This will be enhanced if there are any angular momentum losses from the system. Unless the star is able to contract rapidly enough to stay within its Roche lobe the mass transfer process will become unstable and proceed violently on the short timescale it takes for the star's envelope to respond to changes in structure. This will be the dynamical timescale if the envelope is convective or the thermal timescale if the envelope is radiative. This process must occur in CVs when the more massive component evolves off of the main sequence. However, this phase will be so short-lived as to be almost certainly unobservable. It is possible for some stars to readjust themselves quickly enough to meet the contraction criterion although the exact details of the stellar structure are important in this case, implying the limit might differ slightly from $\frac{5}{6}$.

If $q < \frac{5}{6}$ conservative mass transfer causes the Roche lobe to expand. Mass transfer can then only continue either if the star expands to keep in contact with its Roche lobe or the binary loses angular momentum. The first case can occur as the secondary evolves off of the main sequence. However, the secondary stars in CVs are generally of such low mass that their main sequence lifetimes exceed the Hubble time, so this mechanism cannot be operating. We are thus left with the situation that angular momentum must be being lost from the binary orbit in CVs in order for mass transfer to continue.

At short periods gravitational radiation is an effective mechanism for removing angular momentum from the orbit. At longer periods another process must be operating. Since tidal forces keep the secondary locked in synchronous rotation with the orbit in CVs any process which removes angular momentum from the secondary will also remove angular momentum from the orbit. The most likely reason why $\dot{J} < 0$ for longer period systems is magnetic braking of the secondary.

4.1.1   Magnetic Braking

Magnetic braking (MB) occurs as the wind from the secondary star exerts a torque on it via its magnetic field. As an example of how this operates, consider an isolated star in which wind material is forced to flow along magnetic fieldlines emanating radially from the star. This field forces the wind material to corotate with the star. As the wind material moves out to larger distances, the moment of inertia of the star is effectively increased. In the absence of any external torque the rotation rate of the star decreases in order to conserve angular momentum. Eventually, the wind decouples from the magnetic field and the secondary is left with a lower rotation rate and hence lower angular momentum. In the CV context this slowing of the secondary's rotation is prevented by tidal effects which force it to corotate with the binary. The coupling between the secondary's rotation and the orbit by the tides thus removes angular momentum from the orbit. As the orbit loses angular momentum the orbital period shortens and the tidally locked secondary's spin period also shortens. Paradoxically then, the effect of magnetic braking in a CV is to actually speed up the secondary's rotation.

If the mass transfer process is sufficiently gentle that the star is able to stay close to thermal equilibrium, the secondary will remain close to the main sequence as mass transfer proceeds. Since $R_2 \propto M_2$ is approximately true for the lower main sequence we can set

$$\frac{\dot{R_2}}{R_2} = \frac{\dot{M_2}}{M_2} \tag{4.8}$$

in equation (4.7) and derive

$$\frac{-\dot{M_2}}{M_2} = \frac{\frac{-\dot{J}}{J}}{\frac{4}{3} - \frac{M_2}{M_1}}. \tag{4.9}$$

This shows that the timescales for mass transfer and angular momentum loss are the same to within factors of order unity.

Further progress requires knowledge of the MB process. Detailed modelling of MB is difficult because there are several unknown components to the theory. Whilst the general principles of the dynamo action of stars are understood, good models

predicting the magnetic field strength of a star as a function of stellar parameters are not yet available. Similarly, the mechanisms giving rise to winds from stars are also generally understood but detailed predictions of mass loss rates are not yet reliably available. In spite of these difficulties several authors (Mestel & Spruit 1987, Tout & Pringle 1992 *inter alia*) have produced models for magnetic braking. These authors modelled the wind in two regimes. Inside the Alfvén radius r_A the material is forced to flow along the fieldlines of the secondary. For material close to the magnetic equator these fieldlines are closed and material is trapped in a 'dead zone' and unable to participate in magnetic braking. Material launched from higher magnetic latitudes will follow fieldlines which take it outside r_A. At this radius the material is assumed to decouple from the star and the wind assumed to exert no further braking torque on the star. The significance of r_A can be understood by comparing the kinetic energy density of the wind material to the magnetic energy density. Close to the star the field is strong and the magnetic energy density high dominating the flow. At large distances from the star the field is weak and the energy density drops below the kinetic energy of the wind material. The wind now dominates the field and distorts the field shape forcing the fieldlines to become effectively open. The bending of the fieldlines results in no reactive torque on the star. The Alfvén approach places the boundary between these two regimes at r_A defined by the equality of the kinetic energy density and the magnetic energy density

$$\frac{1}{2}\rho v_{\mathrm{w}}^2 = \frac{B^2}{2\mu_0} \tag{4.10}$$

where v_{w} is the wind velocity. If we know the spatial variation of B we can then determine r_A.

The usual approach, however, describing magnetic braking as applied to CVs follows the semi-analytic one of Verbunt & Zwaan (1981). These authors took the work of Skumanich (1972) and Smith (1979) who had fitted the observed equatorial velocity of a sample of G stars versus age with a function of the form

$$v_e = ft^{-\frac{1}{2}}10^{12} \text{ m s}^{-1} \tag{4.11}$$

where $f = 0.73$ for the earlier work and $f = 1.78$ according to the latter. By taking the derivative of this equation one can determine the braking rate. Verbunt & Zwaan

(1981) extrapolated this relation and applied it to the case of the M dwarfs which comprise the secondary stars in most CVs. This leads to the equation

$$\dot{J}_{2,\mathrm{MB}} = -1.8 \times 10^{30} f^{-2} k^2 M_2^2 \text{ kg m}^2 \text{ s}^{-2}. \tag{4.12}$$

Invoking magnetic braking as an angular momentum loss mechanism for CVs raises interesting questions for magnetic CVs. In the polar systems the magnetic moment of the WD is believed to be of at least the same strength as that of the secondary. If then, the wind material leaving the secondary is able to brake it and drive the CV evolution, will the wind material have a significant effect on the spin evolution of the WD ? Also, what effect does the altered field geometry caused by the presence of the WD's field have on the secondary's magnetic braking ? We shall attempt to answer these questions in the following chapter, but first we shall review the current theory of polar evolution.

4.2   The Evolution of Polars

In order to describe the spin evolution of the components of a CV we need to determine the initial conditions for the binary. The theoretical picture of the common envelope (CE) phase of evolution is still somewhat general with the secondary engulfed by the atmosphere of its higher mass companion as it becomes a red giant. The effect of the secondary orbiting inside the outer parts of its companion is to to reduce the orbital period and to cause the expulsion of the envelope. Since the WD emerges from the core of a primary star which would typically have had a rotation period of days, it is likely to have a spin period of a similar magnitude. The secondary, however, may well emerge from the CE with a rotation period brought close to the orbital period by the viscous drag of the primary's envelope. These assertions, while reasonable, are somewhat speculative given the present state of knowledge of the CE phase. It is probable that most magnetic CVs are born with short enough orbital periods to become polars almost immediately. An alternative scenario, however, is that the CVs are born as longer period, detached systems and

evolve under MB and GR. As angular momentum is removed from the system the secondary will come into contact with its Roche Lobe and mass transfer will begin. Depending on the field strength of the white dwarf a disc will form or material will circulate briefly and then be accreted before a disc can form. In either scenario, the spin period of the white dwarf will become shorter. As the system moves to shorter orbital periods and the stars become closer, other torques (see below) begin to play an important role, and eventually the system becomes locked in synchronous rotation and is classified as a polar.

The processes leading to synchronous rotation of the components in polars were discussed in a series of papers by Campbell (1983, 1984, 1985, 1986a, 1986b & 1989). Aside from magnetic braking and accretion other torques are important in the angular momentum evolution of the system. These are outlined below.

Tidal As with all CVs the secondary star is brought into synchronous rotation with the orbit via tidal interactions. The timescale for this process $t_t \sim 10^7$ y if the secondary emerges from the CE evolution far from synchronism ($\frac{\Delta\Omega}{\Omega} \gtrsim 0.1$. Close to synchronism the tidal interaction is extremely effective and operates on a timescale $t_t \sim 10^2$ y (Campbell & Papaloizou 1983). Van Paradijs (1986) showed that the tidal braking torque could be written as

$$\left(\frac{dJ_2}{dt}\right) = 1.46 \times 10^{28} M_2^4 (1 - \alpha)^{-1} \text{ kg m}^2 \text{ s}^{-2} \qquad (4.13)$$

for substantial deviation from corotation and

$$\left(\frac{dJ_2}{dt}\right) = 5.6 \times 10^{33} M_2^2 (1 - \alpha) \text{ kg m}^2 \text{ s}^{-2} \qquad (4.14)$$

close to corotation, where α is the ratio of the secondary's spin frequency ω_2 to the orbital frequency Ω.

Although formally the torque vanishes at synchronous rotation, it can be seen that tides are able to keep the secondary in close to synchronous rotation with the orbit.

Magnetic Dissipation Campbell (1983) considered the effect on the WD spin of its magnetic field being dragged through the envelope of the secondary. The

resulting dissipation removes angular momentum from the WD spin and brings it towards synchronism. The expressions he derived for the torque are complex but the timescale for bringing the WD to synchronous rotation was shown to be $t_{\text{diss}} = 6.5 \times 10^7$ y for $\frac{|\omega_1 - \Omega|}{\Omega} > 10^{-2}$ and $t_{\text{diss}} = 1.4 \times 10^2$ y for $\frac{|\omega_1 - \Omega|}{\Omega} < 10^{-5.5}$ for parameters appropriate to the polar prototype AM Her.

Dipole-Dipole Observations place tight constraints on the amount of asynchronism that may be present in polar systems. The fact that the magnetic dissipation and tidal torques both vanish at synchronous rotation implies that although they are able to bring the system close to synchronism they are not able to meet the locking condition implied by observations. The most obvious torque to keep the system locked is the interaction of the magnetic fields of the two stars. Campbell (1985) considered the effect of the dipole-dipole torque. The torque is strongly dependent on the separation ($\propto a^{-3}$) but for polars typically operates on a timescale of $t_{\text{dd}} \sim 10^2$ y. In non-synchronous systems this torque averages to zero over a synodic period and thus plays no role in bringing the system towards synchronism. However, for slight amounts of asynchronism this torque rapidly tries to move the two magnetic dipoles towards being colinear. This would be the equilibrium position of two isolated dipoles.

King, Frank & Whitehurst (1990) considered the combined effects of the accretion, magnetic dissipation, magnetic braking, gravitational radiation, tidal dissipation and dipole-dipole torques. They showed that the equilibrium configuration for the system was one where the system was synchronous with both dipoles lying in the orbital plane. The dipole of the WD is forced to lie at an angle leading the line of centres by the accretion torque. The secondary thus takes up a similar configuration with its pole nearest the WD also leading the line of centres such that the WD's dipole lies along one of the secondary's field lines.

This elegant picture is complicated by consideration of the source of the stellar magnetic fields. The WD field is likely to be an intrinsic fossil field (Bhattacharya & Srinivasan 1995). The source of the secondary's field is more problematic, being

presumably the result of some form of dynamo action in the star (Tout & Pringle 1992a). This will tend to result in a field with an axis lying along the rotation axis. If the timescale for generation of this field is similar to t_{dd} the competition between the dipole-dipole torque and the regeneration of the field may result in the effective dipole axis lying at some angle to the orbital plane. The WD would then have to take up an equilibrium position at a corresponding angle to the plane. Observations of the accretion region suggest that the spin axis is indeed at an angle to the magnetic axis (Warner 1995). This is not absolute proof of the picture outlined above, however, as it is possible the higher multipoles may dominate the accretion flow close to the WD allowing the coplanar dipole model to produce accretion out of the plane.

4.2.1 Reduced Magnetic Braking

It has been suggested (Wickramasinghe, Li & Wu 1996 and references therein) that the presence of the primary's field in a polar would reduce the effectiveness of MB by increasing the size of the dead zones. Figures 4.1, 4.2 and 4.3 show sample fieldlines of the resultant field from a secondary with a non-magnetic companion and with a magnetic companion at two different orientations. The fieldlines start from equally spaced positions around each star and are followed until they either leave the plotting area or cross a stellar boundary. The secondary has a surface field of 0.014 T and the magnetic primary has a surface field of 5 000 T. Precise examination of the implications of the dead zones is complicated since the Alfvén radius, where the material decouples from the field, depends upon the density of the wind material. However, it is clear from comparison of figures 4.1 and 4.2 that the effect of the primary's field in the configuration chosen by Wickramasinghe, Li & Wu (1996) is to increase the size of the dead zones dramatically. Figure 4.3 shows the field structure in a configuration similar to that derived by King, Frank & Whitehurst (1990). The dead zones in this configuration appear to occur for a larger range of magnetic latitudes than the single secondary field but smaller than the configuration of Wickramasinghe, Li & Wu (1996).
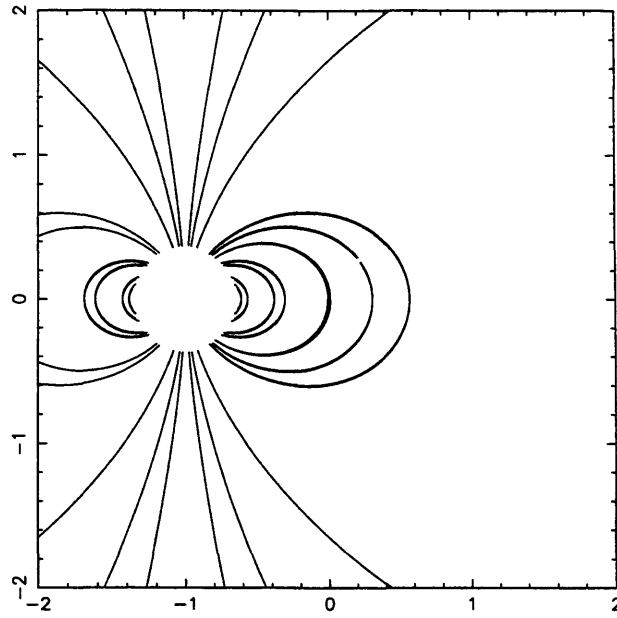
Figure 4.1: Sample fieldlines in cross-section for a spherical secondary star with a dipolar field.
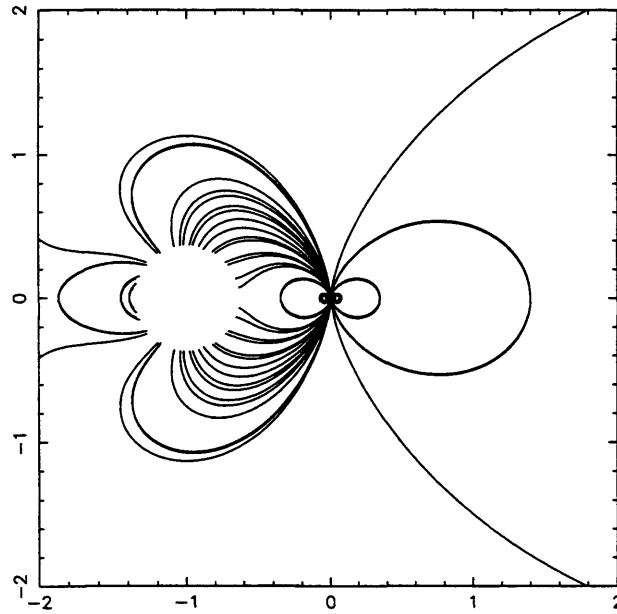

Figure 4.2: Sample fieldlines from the resultant field of two stellar dipoles. The secondary star has a 0.014 T surface field and a radius of 0.37 separations. The primary has a 5 000 T surface field and a radius of 0.01 separations. The dipoles are in the unstable equilibrium position considered by Wickramasinghe, Li & Wu (1996) with the dipoles anti-parallel and the system is shown edge on.
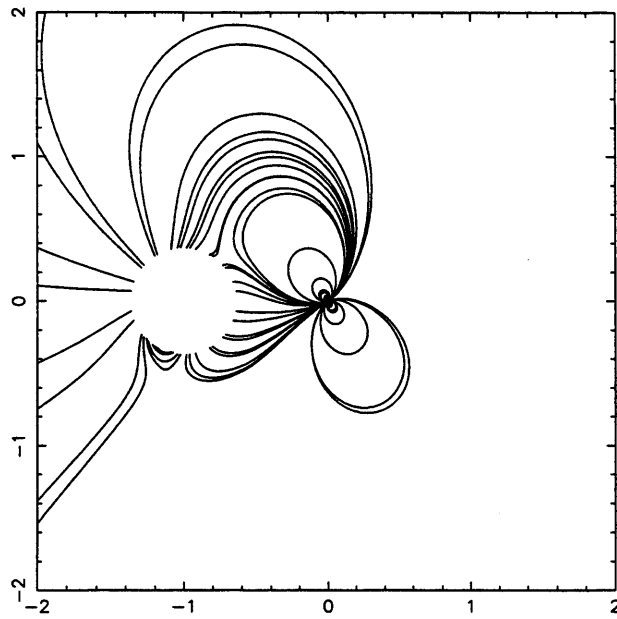
Figure 4.3: Sample fieldlines for the resultant field of two stellar dipoles with the same parameters as used previously. The dipoles are in a configuration similar to that suggested by King, Frank & Whitehurst (1990). The north pole of the WD leads the line of centres pointing away from the secondary by an angle of 30°. The secondary's north magnetic pole leads the line of centres pointing towards the primary by 30°. The system is viewed face on.

The scheme generally adopted in the Alfvén radius model assumes that material in the dead zones is trapped permanently and unable to contribute to MB. Implicit in this, however, is that over time the density of material in the dead zones will increase. One might expect that eventually the pressure exerted by this material would be enough to break open the fieldlines and allow the trapped material to participate in magnetic braking. The resultant field from the addition of the primary changes the nature of many of the dead zones. Instead of trapping material much of the wind material will be funnelled onto the WD and be accreted.

The efficiency of the reduced magnetic braking process depends on several factors. The relative field strengths of the two stars are important in determining the range of positions that material can be launched from the secondary and still participate in MB. The degree to which material is forced to flow along fieldlines is also important. If material is able to slip across the fieldlines the effectiveness of the funnelling of material onto the WD will be reduced.

Chapter 5

Magnetic White Dwarfs and Orbital Braking in Cataclysmic Variables

In this chapter we shall consider simulations which attempt to reproduce the magnetic braking behaviour of a single M dwarf. Having determined parameters giving an acceptable reproduction of this we shall attempt to answer three questions.

1. How does placing the secondary in a binary affect the braking process ?

2. What effect does the wind have on the spin evolution of the WD ?

3. What effect does a magnetic WD primary have on the angular momentum loss from the binary ?

Rather than develop a detailed model of the behaviour of the wind material and its interaction with the stellar magnetic field we shall consider simulations which reproduce the spin-down behaviour modelled by Verbunt & Zwaan (1981). The simulations assume that the magnetic field structure is purely dipolar and rotates rigidly with the star. The interaction between the field and the wind material is

assumed to follow a drag prescription similar to (2.4). The flow of the wind material is likely to be turbulent (Goldstein & Roberts 1995) which suggests that the 'blob' approach might be applicable in this case. However, the validity of the simulations do not rely on this being true. There are several reasons why it is appropriate to model the interactions in this way.

First, the behaviour of the drag force can be used to mimic the behaviour that one would expect from an MHD approach with a given field structure. The effect of a high value of k is to remove energy rapidly from the motion of the material as it crosses fieldlines. This forces the material to flow along the fieldlines. Similarly, relaxing k can allow material to slip through the fieldlines more easily.

The drag prescription is also extremely cheap to implement computationally as it involves only the addition of a single simple term to the equations of motion. Full MHD treatments of flows are extremely complex and time-consuming.

Last, the simulations are not intended initially to reproduce in detail the behaviour of the wind material; rather they are intended to determine a set of parameters which mimic the observed magnetic braking rates and which can then be applied to the components in a CV to study the angular momentum evolution of the system.

A difficulty arises in determining the behaviour of k as a function of position. We shall postpone a detailed discussion of the true behaviour of k until section 5.2 and consider simulations which use $k \propto B \propto r^{-3}$ with k specified at the stellar surface.

5.1   Simulating Magnetic Braking

Simulations of magnetic braking were carried out by adapting the version of Hy-Disc containing a full dipole structure described in section 3.2.1. The simulations assumed that the acceleration mechanism in the wind balanced gravity throughout the computational region. This approach is common in modelling wind phenomena

(*e.g.* Theuns & Jorissen 1993) and the code was modified to remove the gravitational force of the secondary. Particles were injected into the simulation from the surface of the secondary with an initial velocity composed of two components. The radial component was the nominal wind speed, parameterised as a multiple of the sound speed in the secondary's atmosphere. A tangential component was added to each particle according to the rotational velocity of the point at which it left the stellar surface. The radius of the secondary was determined from the main sequence mass-radius relation.

In order to test the changes made to the code a run was carried out with a wind launched from the equatorial plane from a $0.42M_\odot$ secondary in an 8^h binary with a $0.6M_\odot$ primary. The initial wind velocity was $2c_s$. The velocity vectors of the particles are plotted in figure 5.1. The resulting flow pattern is strikingly similar to that of Theuns & Jorissen (1993), plotted in figure 5.2, although these authors modelled a much longer period system containing two non-degenerate stars. These used a smooth particle hydrodynamics (SPH) method.

5.1.1 Braking of Single Stars

In single star simulations, particles were injected at random position on the surface of the star in three dimensions. Rather than change the binary nature of the code completely, these simulations were carried out in a binary which used, for the purposes of scaling, an extreme mass ratio $q = 6\,000$, a primary mass of $M_1 = 0.000\,07$ and $P_{orb} = 8^h$. The gravitational contribution of the primary was also removed from the long-range forces. The simulations thus followed the evolution of an isolated $0.42M_\odot$ star, typical of CV secondaries, in a frame rotating about a point close to the centre of the star.

In order to examine the braking torque the angular momentum of each particle was calculated before and after the integration of the long-range forces (see section 1.4.1). Assuming no deformation of the fieldlines occurs the angular momentum gain of the

file : windtest.006   property : v
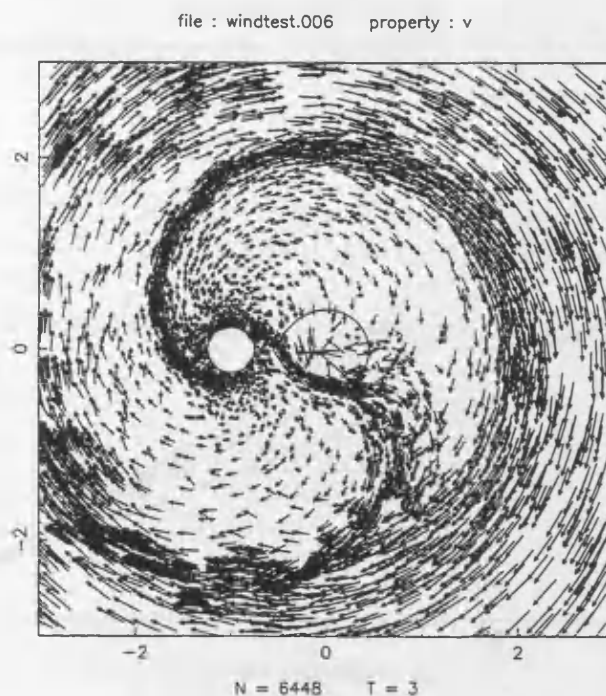

N = 6448   T = 3

Figure 5.1: Plots of the velocity vectors in the co-rotating frame, of particles in a non-magnetic, pre-CV simulation. The stellar radii are marked along with the Roche lobe of the primary. The Roche lobe of the secondary has been removed for clarity.
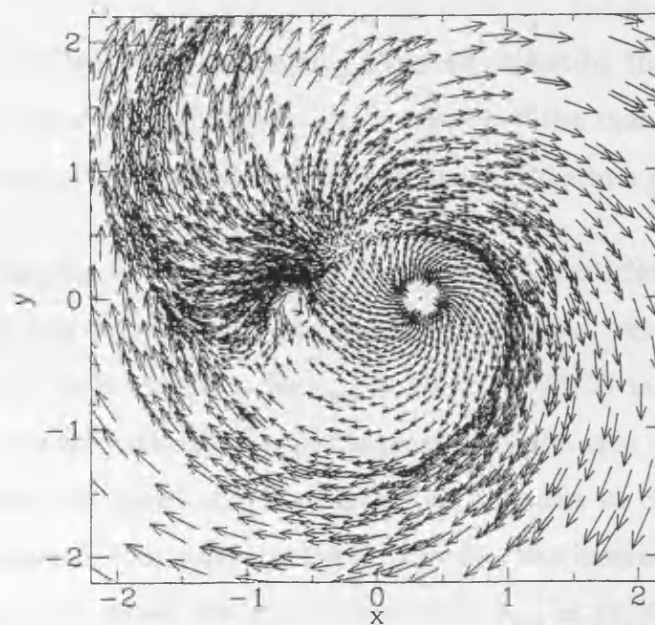

Figure 5.2: Velocity vectors of particles in the adiabatic simulation of Theuns & Jorissen (1993). $M_1 = 3.0 M_\odot$, $M_2 = 1.5 M_\odot$, $R_1 = 200 R_\odot$, $R_2 = 1.0 R_\odot$, $P_{\rm orb} = 895^{\rm d}$, $v_w = 15$ km s^{-1}. In this simulation the wind comes from the more massive, giant star centred at (0.33,0). The companion is centred at (-0.66,0).
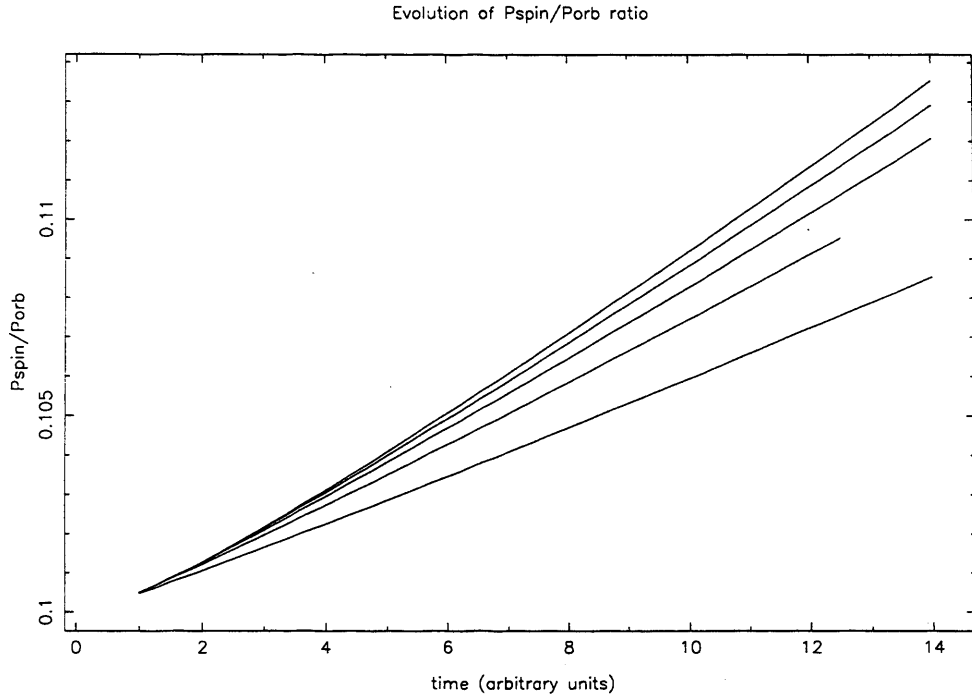
Evolution of Pspin/Porb ratio

Figure 5.3: Spin evolutions examining the effect of varying the outer radius for removal of particles. The evolutions were carried out for $r_{\text{out}} = 10, 20, 30, 40, 50$ in dimensionless units of the separation for a dipole aligned with the spin axis and with $v_{\text{w}} = 10c_{\text{s}}$ and $k = 1$ in dimensionless units. The speed of the evolution steadily increased with r_{out}.

particle must be balanced by the angular momentum lost by the star. The spin rate of the star was adjusted accordingly. As in chapter 2 the moment of inertia of the evolving star was artificially reduced to keep the runtime to a manageable length.

The effect of varying the outer radius r_{out} at which particles were removed, the strength of the drag parameter k, and the wind speed v_{w}, were all examined. Figure 5.3 shows the spin evolution for $r_{\text{out}} = 10, 20, 30, 40, 50$ in dimensionless units (see section 1.4.2) with the dipole axis aligned with the spin axis. Increasing r_{out} steadily increased the speed of the evolution and appears to converge at large r_{out} where the decrease in the magnetic field overcomes the increased lever arm of the particles. Figure 5.4 shows the spin evolution for $r_{\text{out}} = 10, 20, 30, 40, 50$ with the dipole axis perpendicular to the spin axis. For both sets of simulations $k = 1$ in dimensionless units and $v_{\text{w}} = 10c_{\text{s}}$.

These figures suggest that, at least for this rotation period, the braking rate is
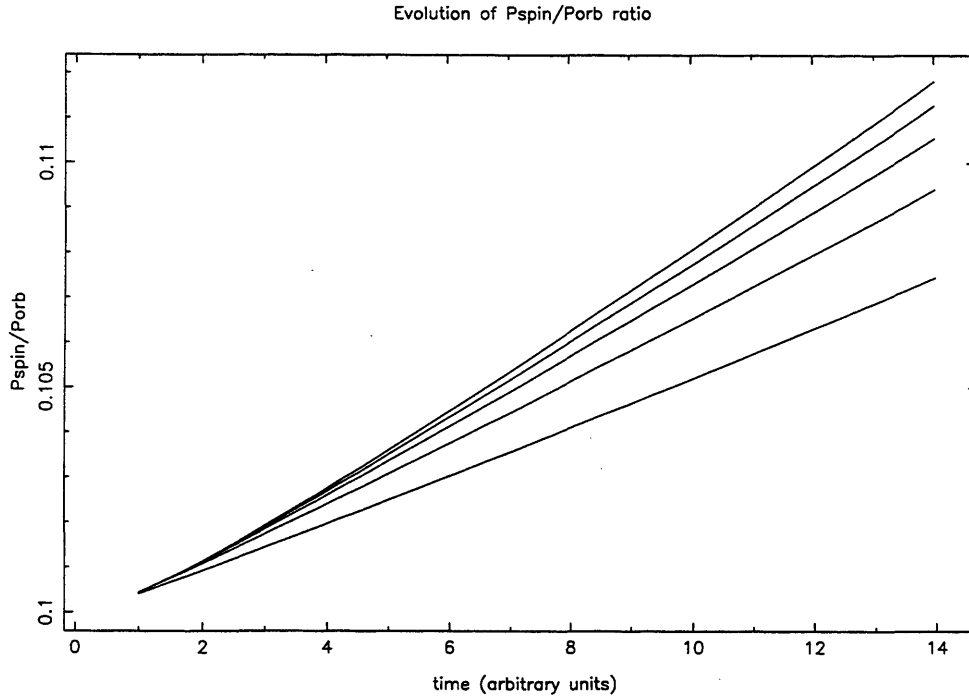
Evolution of Pspin/Porb ratio

Figure 5.4: As figure 5.3 but for a dipole perpendicular to the spin axis. The speed of the evolution steadily increased with r_{out}.

relatively insensitive to the alignment of the dipole axis. This is slightly counter-intuitive since it is easier for material to escape along fieldlines emerging at high magnetic latitudes. The perpendicularly oriented dipole might thus be expected to move material to larger lever arms more effectively than the parallel dipole. The exact effect of this on the braking rate is not obvious, but given a different flow pattern we might naively have expected a different braking rate. The subsequent simulations were all carried out with the magnetic dipole axis aligned with the spin axis of the star.

Figure 5.5 shows the spin evolution for $v_w = 2c_s$, $5c_s$, $10c_s$ with the dipole axis parallel to the spin axis. For this set of simulations $k = 1$ in and $r_{out} = 50$.

Figure 5.6 shows the spin evolution for $k = 1$, 10, 100 with the dipole axis parallel to the spin axis. For this set of simulations $v_w = 10c_s$ and $r_{out} = 50$. This figure suggests that the timescale for the evolution is approximately proportional to k.

Figure 5.7 is a plot of $\dot{\omega}$ against ω for a $k = 50\,000$, $v_w = 2c_s$, $r_{out} = 100$ simulation
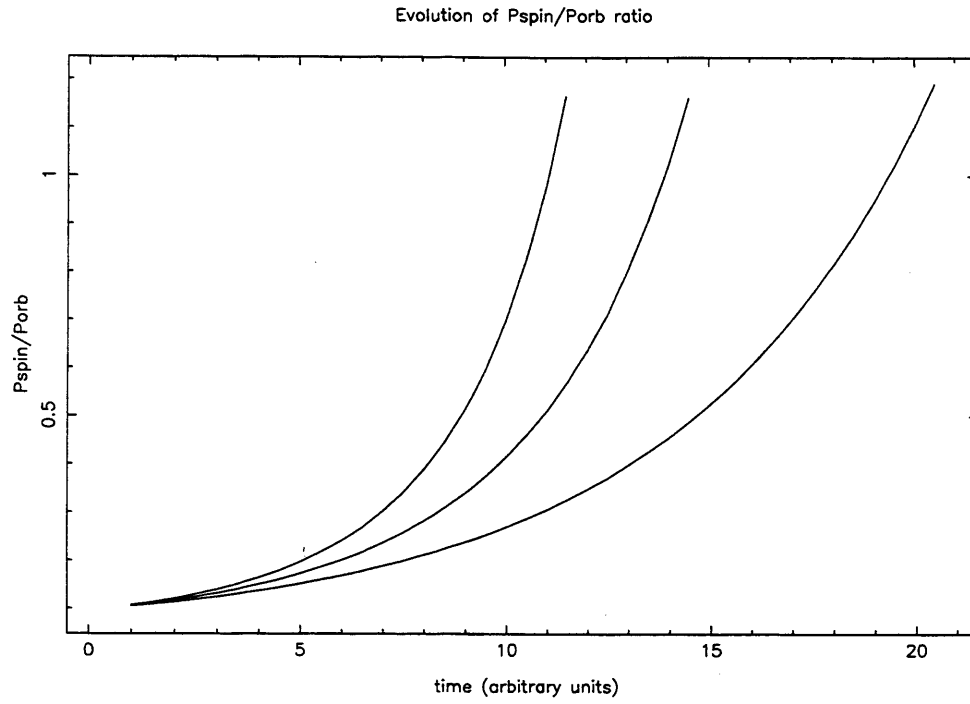
Evolution of Pspin/Porb ratio

Figure 5.5: Spin evolutions examining the effect of varying the initial wind speed $v_w = 2c_s$, $5c_s$, $10c_s$ with a dipole parallel to the spin axis. The speed of the evolution steadily decreased with increasing v_w.
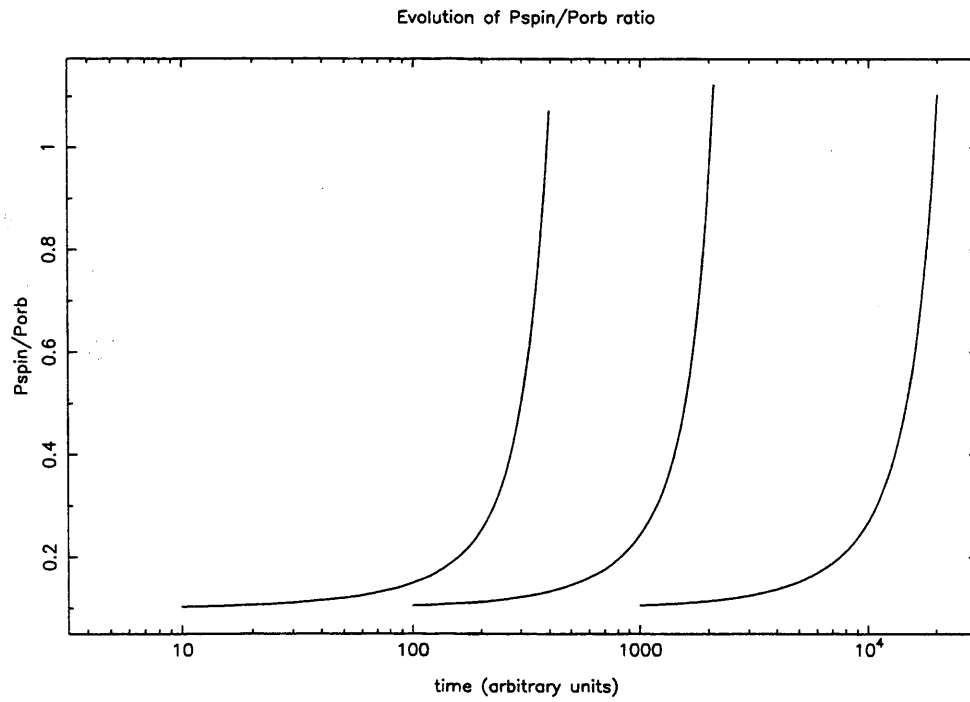
Evolution of Pspin/Porb ratio

Figure 5.6: Spin evolutions examining the effect of varying the drag parameter $k = 1$, 10, 100 in dimensionless units with a dipole parallel to the spin axis. The speed of the evolution steadily increased with increasing k.
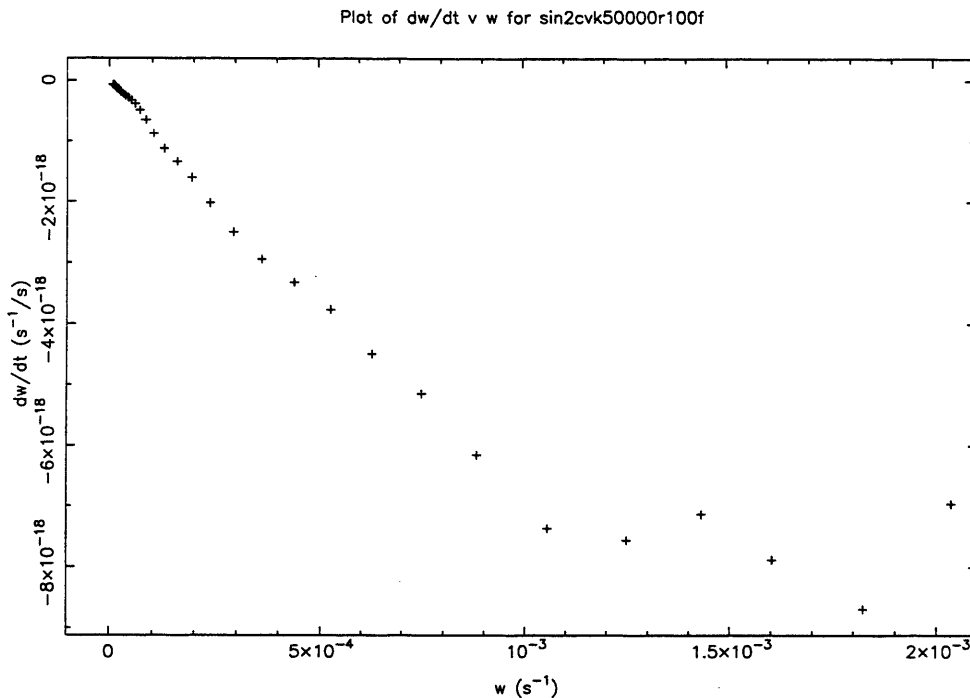
Plot of dw/dt v w for sin2cvk50000r100f

Figure 5.7: A graph of $\dot{\omega}$ against ω from a $k = 50\ 000$, $v_w = 2c_s$, $r_{out} = 100$ simulation.

assuming a mass loss rate $\dot{M} = 10^{-10}\ M_\odot\ \text{y}^{-1}$. This graph may be compared to that derived from the braking rate derived by Verbunt & Zwaan (1981, hereafter VZ) in figure 5.8 (see equation (4.12)) and that of Mestel & Spruit (1987, hereafter MS) in figure 5.9. Figures 5.8 and 5.9 show that the behaviour of the braking laws of MS and VZ are similar. Two differences between the drag simulations and the work of these previous authors are immediately apparent however. Firstly, the curve of the graph from the drag simulations is in a different sense. Also the magnitude of the braking rate implied by $\dot{\omega}$ is too low from these simulations to match the previous works.

The parameters used in this simulation were extreme. The value of k in the simulation was extremely high and forced virtually all the escaping material to come from the poles of the star (see figure 5.10). This is in contrast to the solar wind where we know that there is some wind material in the ecliptic plane. The surface magnetic fields of these stars, while stronger than that of the sun ($B_\odot \sim 10^{-4}$ T compared to $B \sim 10^{-1}$ T), are unlikely to be able to enforce such an extreme flow pattern
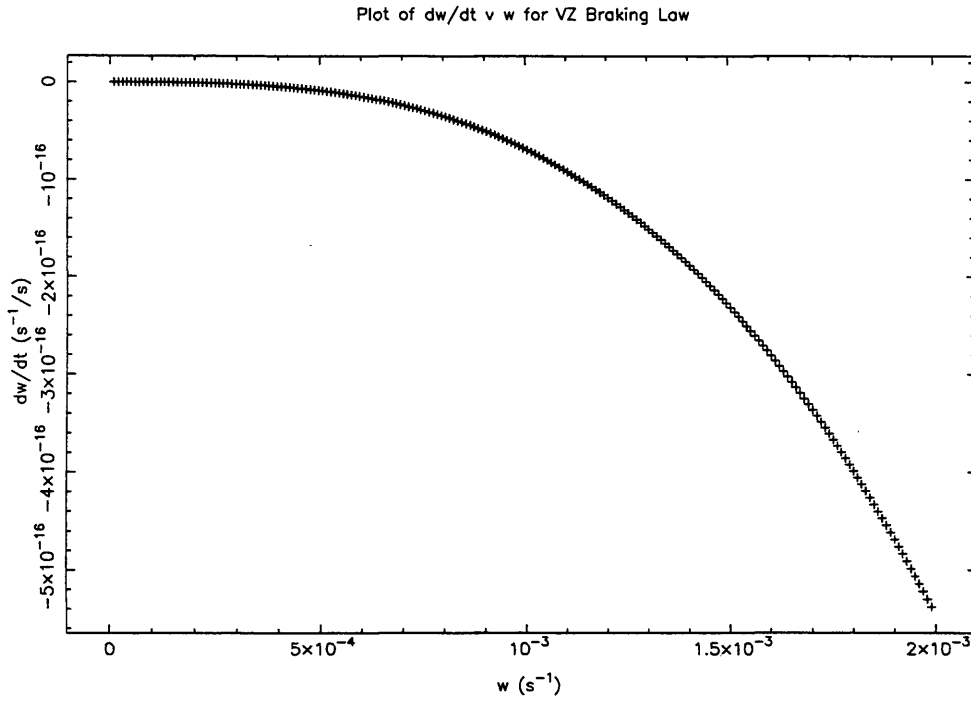
Plot of dw/dt v w for VZ Braking Law

Figure 5.8: A graph of $\dot{\omega}$ against ω derived from the braking rate of Verbunt & Zwaan (1981) for a $0.42M_\odot$ star.
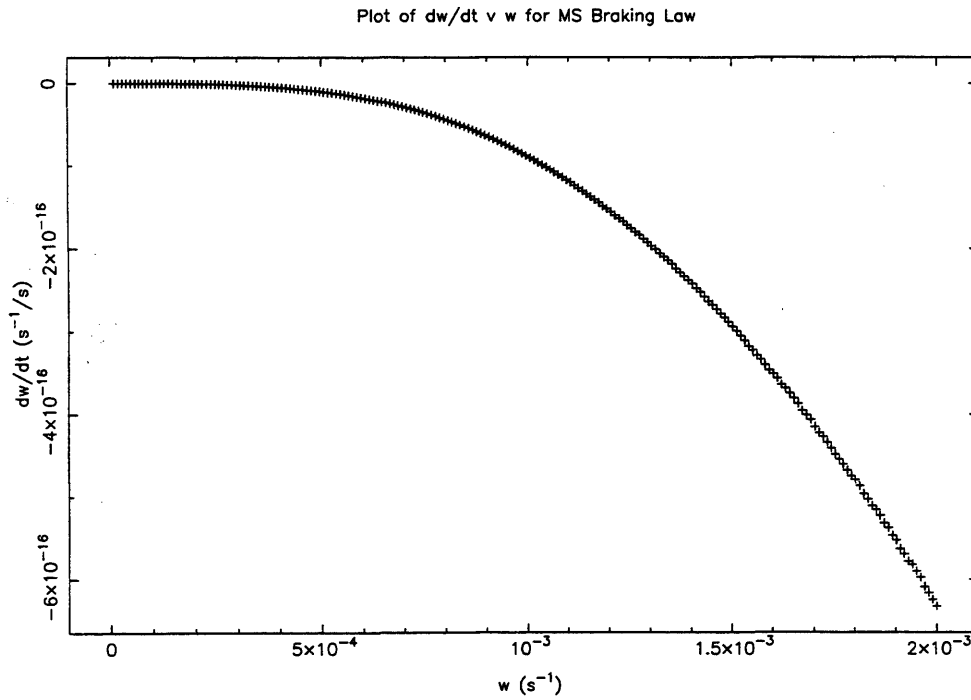
Plot of dw/dt v w for MS Braking Law

Figure 5.9: A graph of $\dot{\omega}$ against ω derived from the braking rate of Mestel & Spruit (1987) for a $0.42M_\odot$ star with $v_w = 2c_s$ and model index parameters $n = p = 1$.
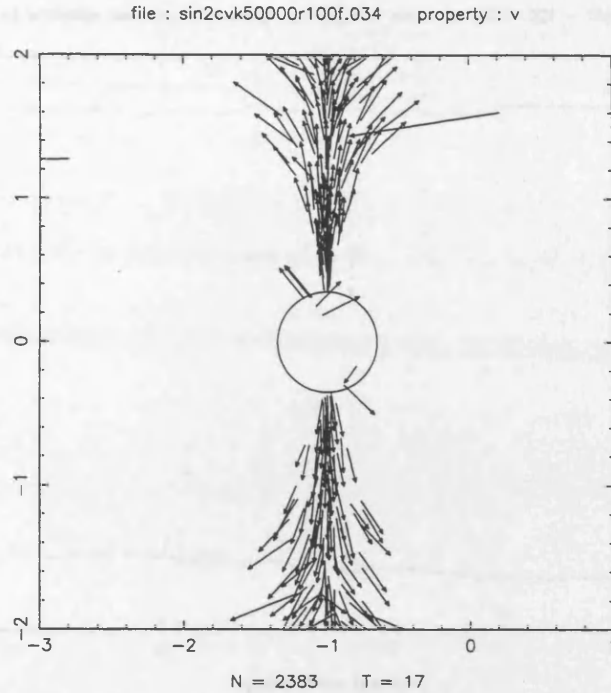
file : sin2cvk50000r100f.034   property : v

N = 2383   T = 17

Figure 5.10: A plot of the velocity vectors (in the rotating frame) of the particles in the $k = 50\,000$, $v_{\mathrm{w}} = 2c_{\mathrm{s}}$, $r_{\mathrm{out}} = 100$ simulation in the x-z projection.

with such large dead zones. The mass loss rate used in the derivation of the particle mass, and hence the determination of $\dot{\omega}$, is high. Mullan *et al.* (1992) claimed that $\dot{M} \sim 10^{-10}\ M_{\odot}\ \mathrm{y}^{-1}$ could be derived from their observations of a sample of isolated M dwarfs. This extreme mass loss rate can just enable the $\dot{\omega}$ from the simulations to match those of MS and VZ if the number of particles presumed to make up the wind excludes those which are rapidly reaccreted. Figure 5.11 shows a plot of the number of particles which escape from the simulations and are reaccreted by the star. Approximately 1 400 particles are rapidly reaccreted by the star every half period, out of 1 500 injected. If the difference of 100 particles is taken to represent the mass in the wind, the increased particle mass gives a factor 15 which brings the derived $\dot{\omega}$ into closer agreement with VZ and MS. The work of Mullan *et al.* (1992) has been criticised, however, in a recent paper by Lim & White (1996) who derive instead $\dot{M} \sim 10^{-13}\ M_{\odot}\ \mathrm{y}^{-1}$ from a reappraisal of the same observations. Such a mass loss rate renders the $\dot{\omega}$ derived even using the most favourable set of parameters for the simulations at least 3 orders of magnitude too low.
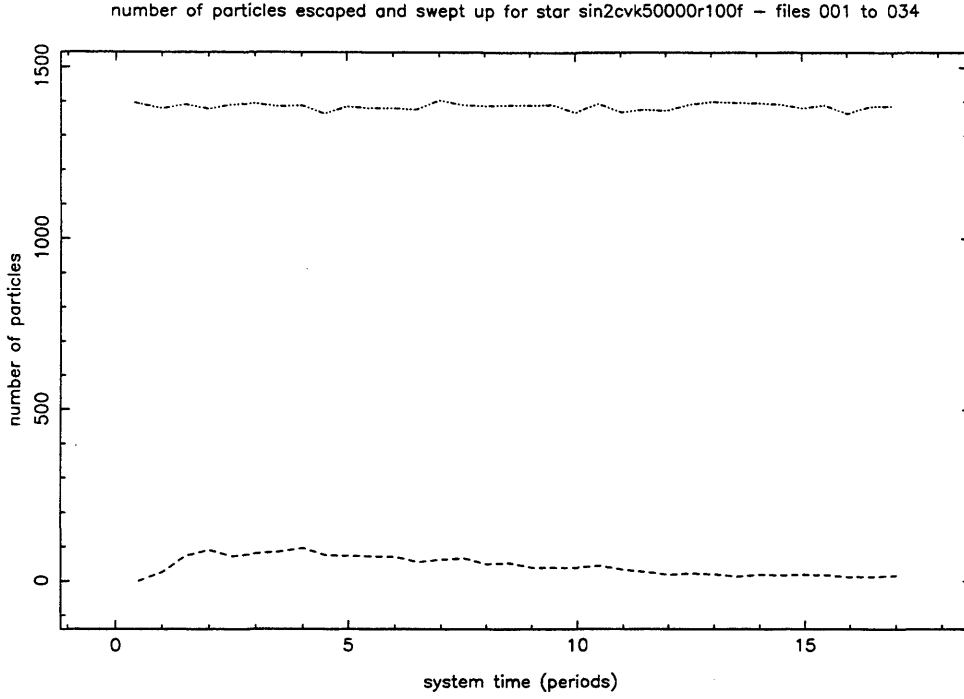
number of particles escaped and swept up for star sin2cvk50000r100f — files 001 to 034

Figure 5.11: A plot of the number of particles which escaped (dotted line) and were re-accreted by the star (dot-dashed line) in the $k = 50\ 000$, $v_{\mathrm{w}} = 2c_{\mathrm{s}}$, $r_{\mathrm{out}} = 100$ simulation.

This comparison of the drag simulations with the works of the previous authors suggests that some modification of the force law we have employed to describe the wind-field interaction might be appropriate. The problem of a conductor moving in a magnetic field which was considered by Drell, Foley & Ruderman (1965) was reexamined by Dobrowolny & Veltri (1986) who derived a power radiated by the conductor differing by a factor $(\frac{v}{c})^2$ from the original work. Accordingly, a new drag parameter k_{n} can be defined such that

$$k_{\mathrm{n}} = \frac{k}{c^2} \qquad (5.1)$$

and the force per unit mass written as

$$\mathbf{f}_{\mathrm{drag}} = -k_{\mathrm{n}} v_{\perp}^2 \mathbf{v}_{\perp} \qquad (5.2)$$

where

$$\mathbf{v}_{\perp} = [\mathbf{v}' - (\mathbf{v}'.\hat{\mathbf{b}})\hat{\mathbf{b}}] \qquad (5.3)$$

Simulations using (5.2) were carried out. The effects of varying v_{w}, k and r_{out} were again examined and similar results to those for the original force law were found.

Consideration was given to choosing an appropriate r_{out} for the simulations. The field structure has been presumed to rotate rigidly with the star. It may be possible that in reality, at some radius analogous to r_A, the pressure exerted by the wind material will overcome the magnetic pressure holding the field shape fixed. It is certainly true that the field and material will decouple at the light-cylinder where the magnetic field is rotating at the speed of light. Setting,

$$r_{\text{out}}\omega = c \tag{5.4}$$

shows that for a typical period of 8^{h} ($\omega \sim 2 \times 10^{-4}$ s^{-1}), $r_{\text{out}} \sim 1 \times 10^{12}$ m. In dimensionless units this gives $r_{\text{out}} \sim 10^3$.

Figure 5.12 shows a plot of $\dot{\omega}$ against ω for a simulation carried out using the revised force law, $v_{\text{w}} = 10c_{\text{s}}$, $k_{\text{n}} = 3$ and $r_{\text{out}} = 1\,000$ assuming $\dot{M} = 10^{-12}M_{\odot}$ y^{-1}. The braking laws of VZ and Mayor & Mermilliod (1991, hereafter MM) are plotted on the same diagram for comparison. MM suggested an alternative function fitting the observed rotation rates of stars of the form

$$\frac{1}{v_2} - \frac{1}{v_1} = a(t_2 - t_1) \tag{5.5}$$

where $a = 0.023$ if v, the rotational velocity, is measured in km s^{-1} and t, the age, in Gy. It can be seen from this graph that there are still reasonably large uncertainties in the magnetic braking rate derived from observations. Bearing this in mind it can be seen that this simulation is in comfortable agreement with these functions.

The results from the same simulation are plotted in figure 5.13 in the form of the timescale for magnetic braking t_{mb} versus ω. This shows $t_{\text{mb}} \sim 10^5$–10^6 y.

The velocity vectors of particles inside a cube of side 4 centred on the star are plotted in figures 5.14 and 5.15 when the star had a spin period of 0.8^{h} and 4.6^{h} respectively. These show that when the star is rotating rapidly material is rapidly centrifugally expelled if it emerges away from the rotational poles. At longer periods the material is able to escape from all latitudes without dramatic acceleration, although there appears to be a slight enhancement close to the poles.
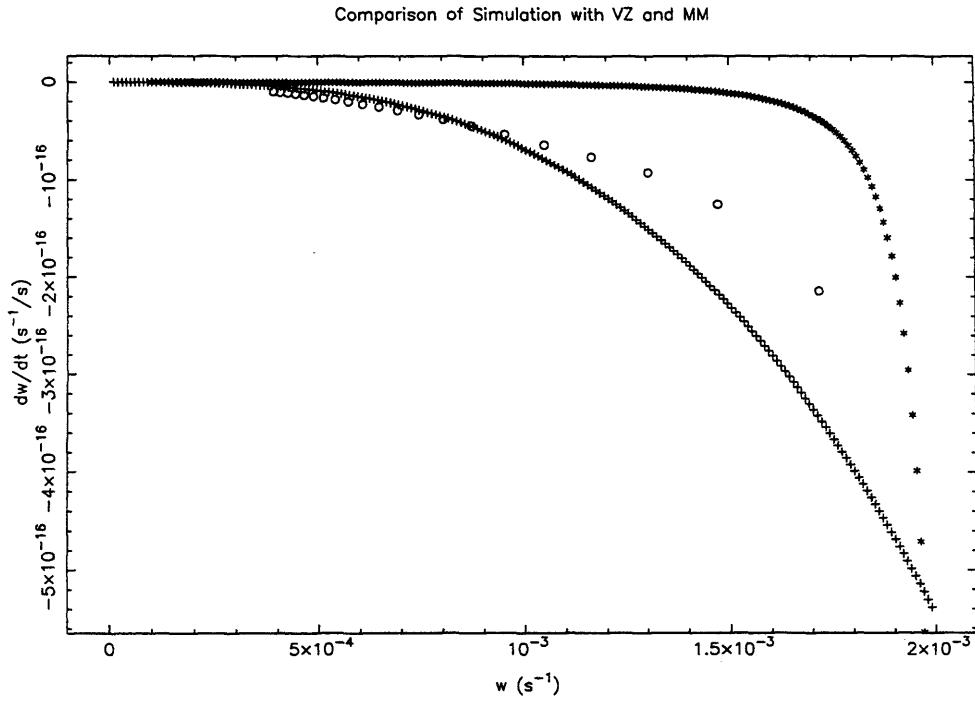
Comparison of Simulation with VZ and MM

Figure 5.12: Plots of $\dot{\omega}$ against ω for a simulation using the revised force law, $v_{\rm w} = 10c_{\rm s}$, $k_{\rm n} = 3$ and $r_{\rm out} = 1\,000$ assuming $\dot{M} = 10^{-12}M_\odot$ y^{-1} (circles) and the braking laws of VZ (crosses) and MM (stars).

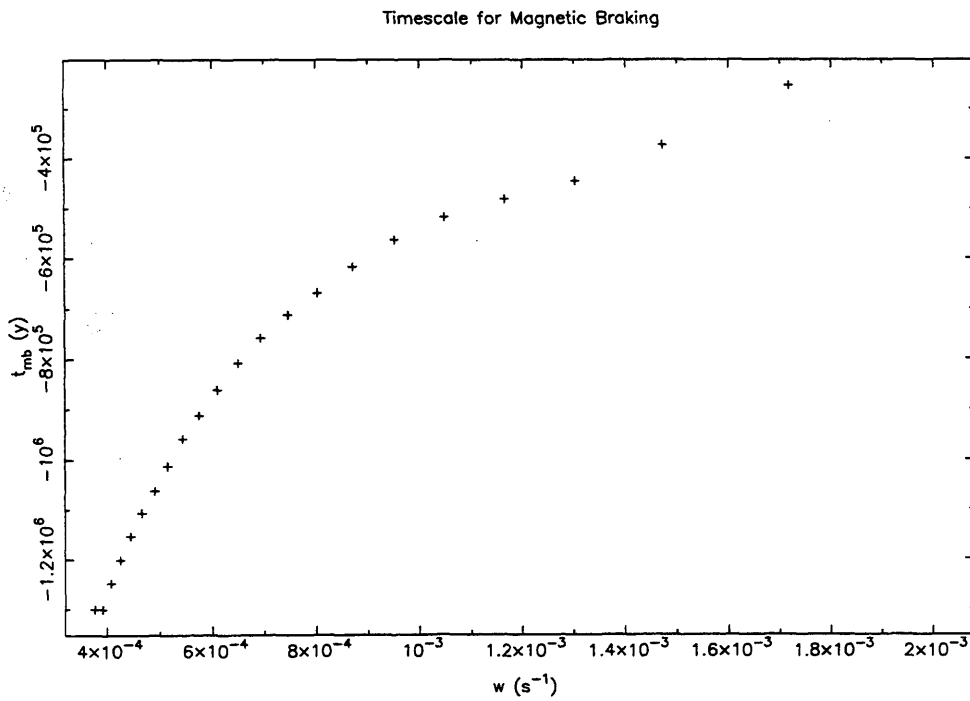Timescale for Magnetic Braking

Figure 5.13: Plot of $t_{\rm mb}$ against ω for a simulation using the revised force law, $v_{\rm w} = 10c_{\rm s}$, $k_{\rm n} = 3$ and $r_{\rm out} = 1\,000$ assuming $\dot{M} = 10^{-12}M_\odot$ y^{-1}.

file : sinvk3e0r1000v3ws.006   property : v

N = 3725   T = 3

Figure 5.14: Plot of the velocity vectors of particles inside a cube of side 4 centred on the star for a simulation using the revised force law, $v_w = 10c_s$ and $k_n = 3$. The spin period of the star 0.8^h.

file : sinvk3e0r1000v3ws.028   property : v
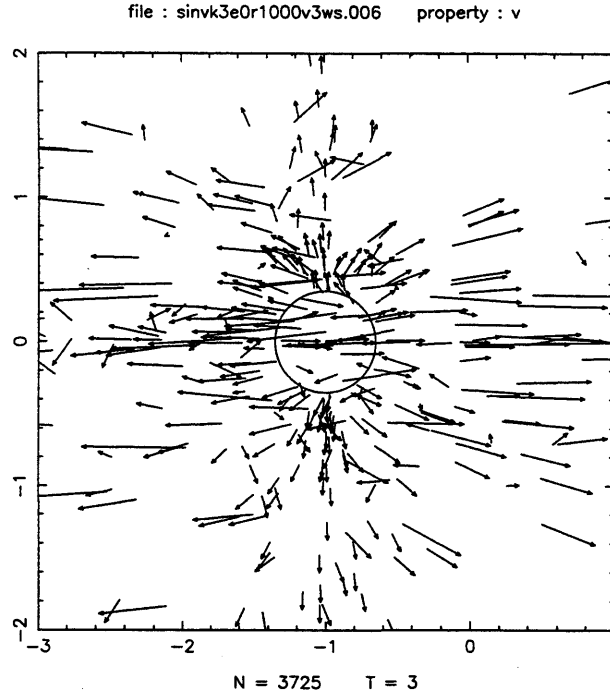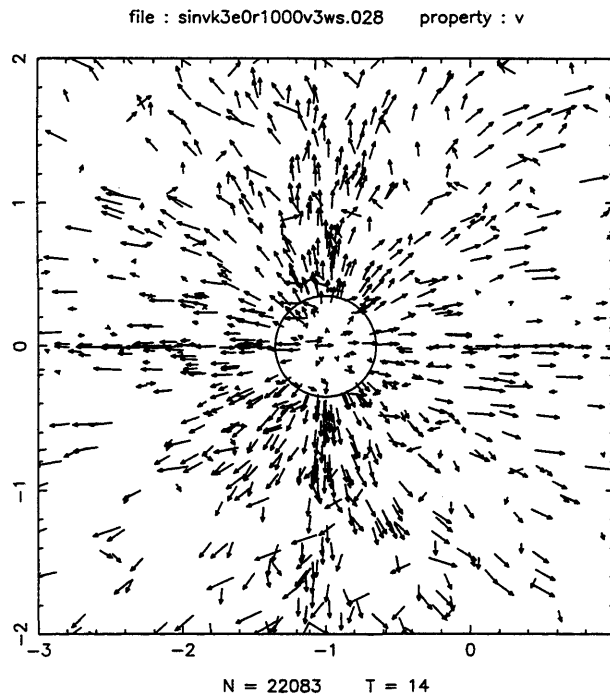

N = 22083   T = 14

Figure 5.15: Plot of the velocity vectors of particles inside a cube of side 4 centred on the star for a simulation using the revised force law, $v_w = 10c_s$ and $k_n = 3$. The spin period of the star 4.6^h.

5.1.2   Braking of the Secondary in a pre-CV

Simulations of magnetic braking of the secondary star in a pre-CV were carried out with $M_1 = 0.7$, $M_2 = 0.42$, $P_{orb} = 8^h$, $v_w = 10c_s$ and $r_{out} = 1\,000$ using the force law described by (5.2). The gravitation of the primary was restored to the long range forces. The secondary was still assumed to be spherical and had a radius determined by the main sequence mass-radius relation.

Figure 5.16 shows a plot of ω versus time for a simulation with no magnetic fields present. This tests the consistency of the angular momentum calculations. In previous spin evolution applications of HyDisc, material has been orbiting in such a way that the star under examination could be considered to be an inertial point. This can either be because material was orbiting well inside the Roche lobe of the primary when considering the spin evolution of IPs (Wynn & King 1995) or because parameters were chosen such that the star was very close to the centre of mass (eg. section 5.1.1 above). Since angular momentum is only conserved about a fixed point in an inertial frame this figure estimates the error introduced by taking moments about the secondary star. It can be seen that during the simulation ω has only drifted by $\sim 3 \times 10^{-7}$ s^{-1}. A more modest $\dot{M} \sim 10^{-12} M_\odot$ y^{-1} which was successful in modelling the magnetic braking of single stars above would reduce this drift still further to $\sim 3 \times 10^{-9}$ s^{-1}. The timescale for this effect to become significant is thus extremely long compared to t_{mb}. The oscillatory nature of the angular momentum drift will also become apparent if the error it introduces becomes important. We can therefore proceed with confidence knowing that the resulting error is negligible.

A simulation was carried out with the same parameters which were successful in modelling the magnetic braking of a single star ($v_w = 10c_s$, $k_n = 3, r_{out} = 1\,000$ and $\dot{M} = 10^{-12} M_\odot$ y^{-1}). Figure 5.17 shows a plot of t_{mb} versus ω for the simulation along with that from the single star simulation for comparison. It is apparent that placing the star in a binary has not had a significant effect on the braking rate despite the introduction of the secondary's orbital motion.

Spin Frequency for star secvk0r1000v3s — files 001 to 020
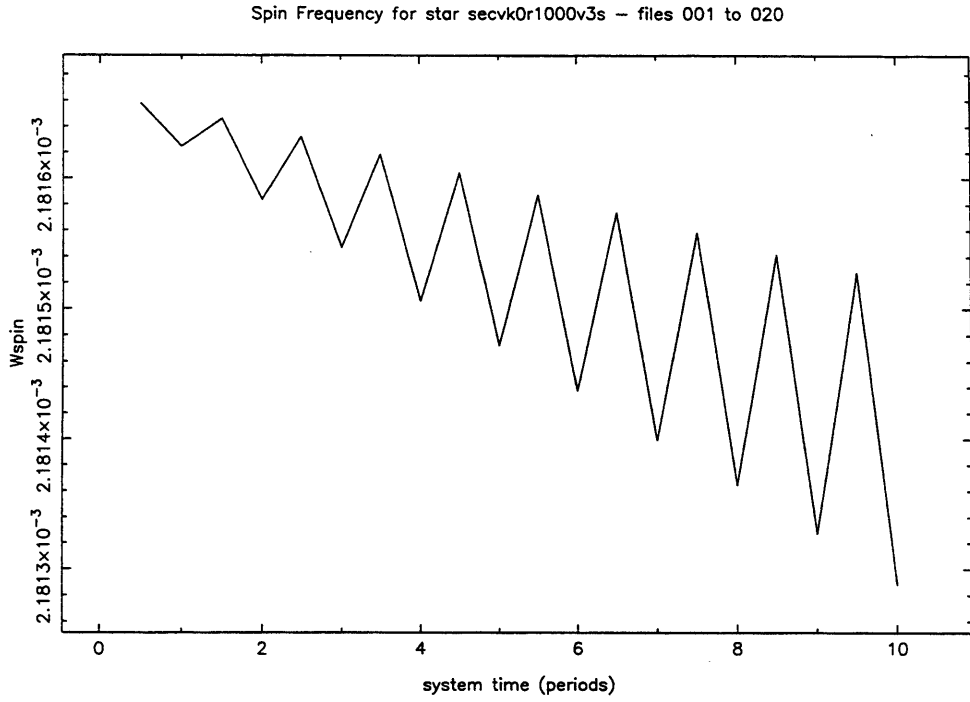
Figure 5.16: Plot of ω against t for a secondary star in a pre-CV using the revised force law, $v_{\mathrm{w}} = 10c_{\mathrm{s}}$, $k_{\mathrm{n}} = 0$ and $r_{\mathrm{out}} = 1\,000$ assuming $\dot{M} = 10^{-10}M_\odot$ y^{-1}.

Timescale for Magnetic Braking

Figure 5.17: Plot of t_{mb} against ω for a secondary star in a pre-CV (circles) and a single star (crosses) using the revised force law, $v_{\mathrm{w}} = 10c_{\mathrm{s}}$, $k_{\mathrm{n}} = 3$ and $r_{\mathrm{out}} = 1\,000$ assuming $\dot{M} = 10^{-12}M_\odot$ y^{-1}.

total number of particles removed from simulation for star secvk3e0r1000v3ws — files 001 to 039

Figure 5.18: Plot of the total number of particles removed from the simulations for the magnetic secondary star simulations.
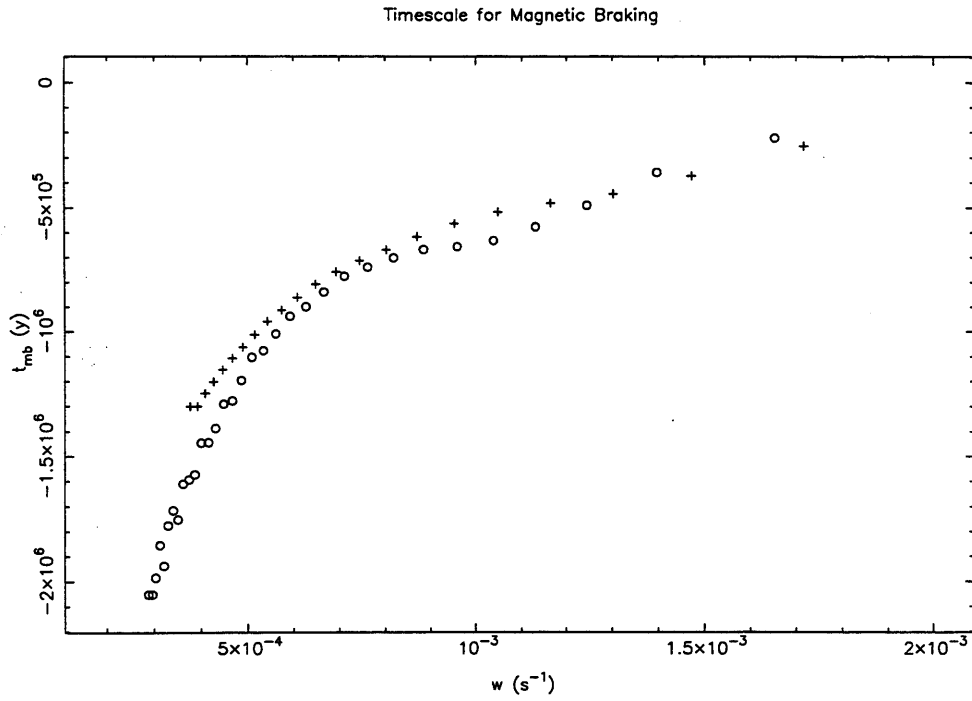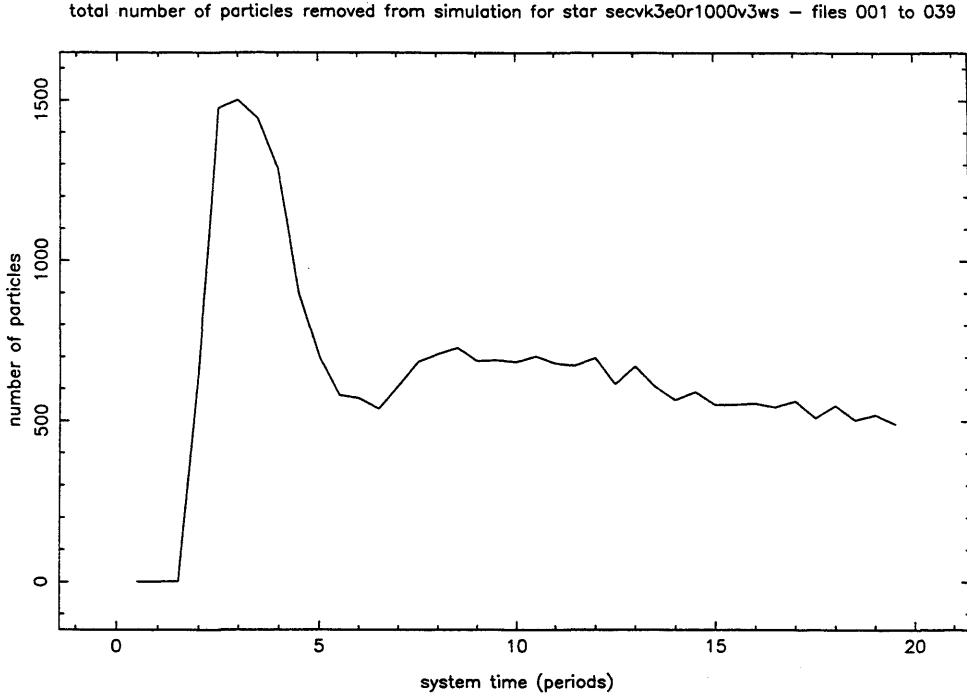
The total number of particles removed from the simulation, ie. the sum of the number accreted by the WD, swept up by the secondary or escaping from the system, is plotted in figure 5.18. This figure shows an initial burst caused by particles centrifugally ejected at early, high rotation rates. The number removed then slowly declines but settles at $\approx$ 6000. This implies that the number of particles is the simulation is gradually increasing and material is building up in a cloud around the binary. The simulations have thus been carried out in a non-steady state. Steady state would be achieved with a larger number of particles in the simulation and we would thus expect the derived braking rates to underestimate the true timescale slightly.

5.1.3 Braking of the Primary in a pre-CV

We can estimate the effect of the secondary's wind on a magnetic primary by considering the behaviour of material at large distances from the binary. In such a

situation the material will experience two magnetic force terms: one arising from the secondary and one from the primary. At such large distances, if the magnetic moments of the two stars are approximately equal the force exerted by each on the material will also be approximately equal. Similarly, the reaction on the rotation of each star will be closely comparable. We can thus estimate the timescale for spindown of the WD from the ratio of the moments of inertia of the two stars.

$$\frac{t_{\rm WD}}{t_{\rm MB}} \sim \frac{I_{\rm sec}}{I_{\rm WD}} \tag{5.6}$$

$$\sim \frac{M_2 R_2^2}{M_1 R_1^2} \tag{5.7}$$

$$= q\frac{R_2^2}{R_1^2} \tag{5.8}$$

$$\sim 1000 \tag{5.9}$$

Hence, we would expect $t_{\rm WD} \sim 10^2$–10^3 y.

The error introduced by taking moments about the WD rather than the centre of mass was examined as for the secondary simulations and again found to be negligible.

An appropriate surface value of $k_{\rm n}$ can be obtained by scaling from that used for secondary by the factor $\left(\frac{R_2}{R_1}\right)^3$. Hence a WD surface value of $k_{\rm n} \approx 150\ 000$ would correspond to a primary with a magnetic moment equal to the secondary's.

Simulations were carried out using a version of HyDisc with the addition of a second dipolar field centred on the WD. Figure 5.19 shows $t_{\rm WD}$ plotted against ω for the same binary parameters as used above, and with $k_{\rm n} = 88\ 000$, appropriate to a relatively weakly magnetic WD and with no secondary field.

Figure 5.19 shows that $t_{\rm WD} \sim 2 \times 10^3$ y, which is slightly longer than the crude estimate made earlier, but still extremely rapid in evolutionary terms.
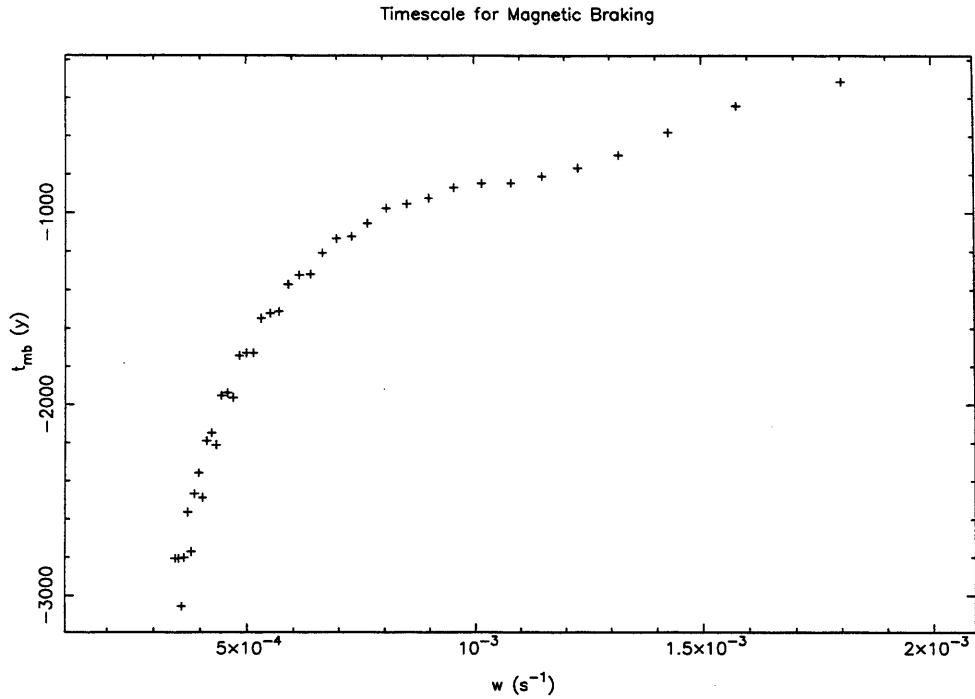
Figure 5.19: Plot of t_{WD} against ω for a magnetic WD star in a pre-CV (circles) using the revised force law, $v_w = 10c_s$, $k_n = 88\,000$ and $r_{out} = 1\,000$ assuming $\dot{M} = 10^{-12} M_\odot$ y^{-1} in the wind of the secondary.

5.1.4 Reduced Magnetic Braking

The possibility of reduced magnetic braking suggested by Wickramasinghe, Li & Wu (1996) and described in section 4.2.1 was investigated by carrying out simulations with a synchronously rotating white dwarf and secondary. The angular momentum gain of the particles was subtracted from the orbital angular momentum calculated using a nominal orbital period. The orbital parameters used for the scaling and in the calculation of the forces were held fixed. Comparison of the resulting braking rates with and without a primary magnetic field could then be carried out in a model polar system. Since the drag prescription couples the binary to material at large distances it is important to consider the environment in which the polar is evolving. If the system has evolved from a longer period, material which took part in the earlier phase of magnetic braking may be circulating in the cloud implied by figure 5.18. As a result the simulations were started with a notional orbital

number of particles accreted, escaped and swept up for star totalsecws — files 040 to 044
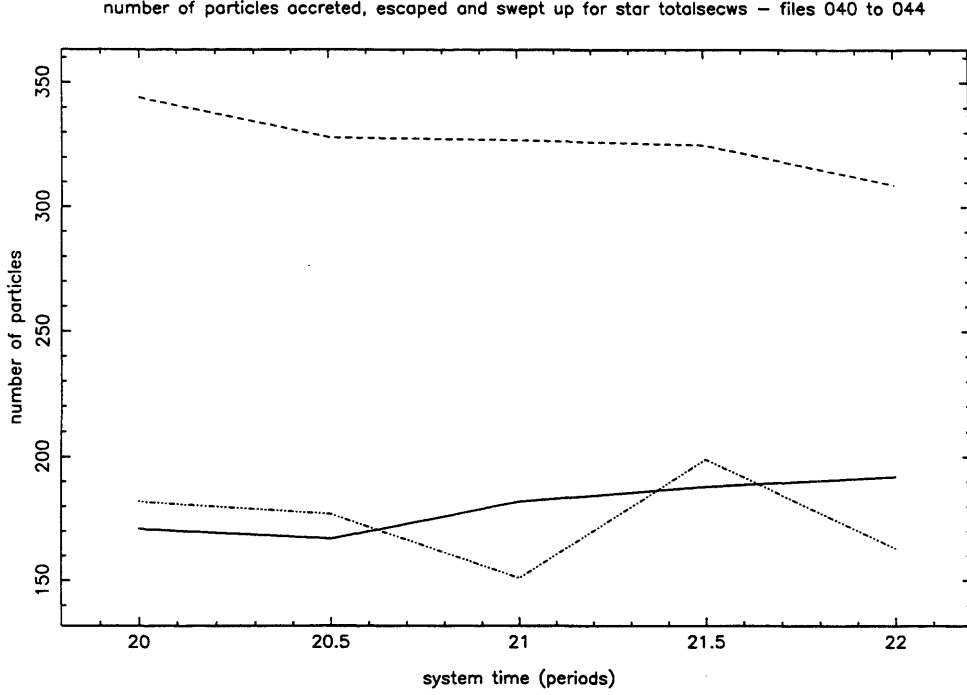

Figure 5.20: Plot of the number of particles accreted by the WD (solid), escaping (dashed) and swept up by the secondary (dot-dashed) for a synchronously locked pre-CV. The simulation used the revised force law, $v_w = 10c_s$, $k_n = 0$ for the primary, $k_n = 3$ for the secondary, and $r_{out} = 1\ 000$.

rotation rate close to 8^h using the flow pattern produced by the magnetic secondary simulation in section 5.1.2.

Figure 5.20 shows the number of particles accreted by the WD, escaping and swept up by the secondary for a simulation with $v_w = 10c_s$, $k_n = 0$ for the primary, $k_n = 3$ for the secondary and $r_{out} = 1\ 000$, assuming $\dot{M} = 10^{-12}M_\odot$ y^{-1}. Since the orientation of the stars was held fixed in the simulations the braking rate is strictly only applicable to a synchronously rotating system at 8^h. The braking timescale derived from the simulation for this period was 3.6×10^8 y. The increase in the braking timescale over that for the secondary is caused by the the larger moment of inertia of the binary compared to that of the secondary alone.

A second simulation was carried out for similar parameters but with a strong primary field of $k_n = 880\ 000$ appropriate to a polar system placed anti-parallel to the
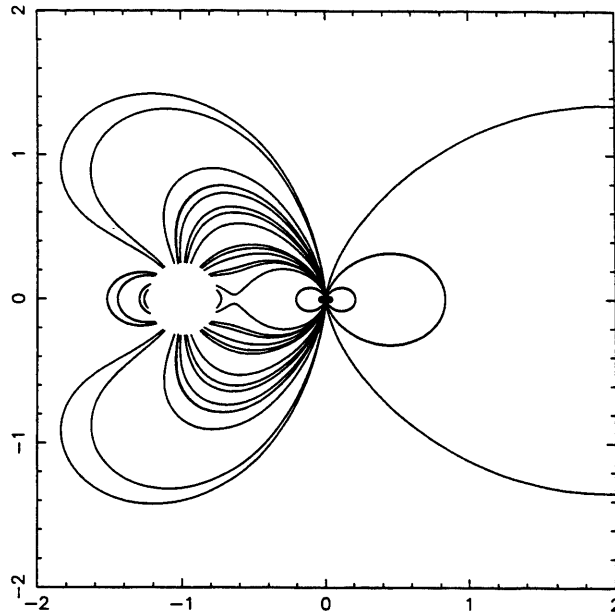
Figure 5.21: Sample fieldlines from the field produced from the same orbital parameters as used in the polar simulation, with $k_n = 880\ 000$ for the primary and $k_n = 3$ for the secondary, oriented anti-parallel in the binary. The system is viewed edge-on.

secondary's dipole. This corresponds to the orientation proposed for reduced magnetic braking with both dipoles perpendicular to the orbital plane and anti-parallel. The field structure for this simulation is plotted in figure 5.21. The resulting graph of the number of particles accreted, escaped and swept up is shown in figure 5.22. The derived braking timescale was 8.3×10^7 y. Figures 5.20 and 5.22 show that the introduction of the WD field increases the number of particles accreted by the WD, while leaving the escaped and swept up rates essentially unaffected. This is confirmation of the increased size of the dead zones between the two stars.

5.2   Discussion

We have seen in section 5.1.1 that a simple drag prescription for the interaction of the stellar magnetic field with wind material is able to give an accurate representation of the magnetic braking behaviour of single stars. The parameters used for the

number of particles accreted, escaped and swept up for star totalsecws — files 040 to 044
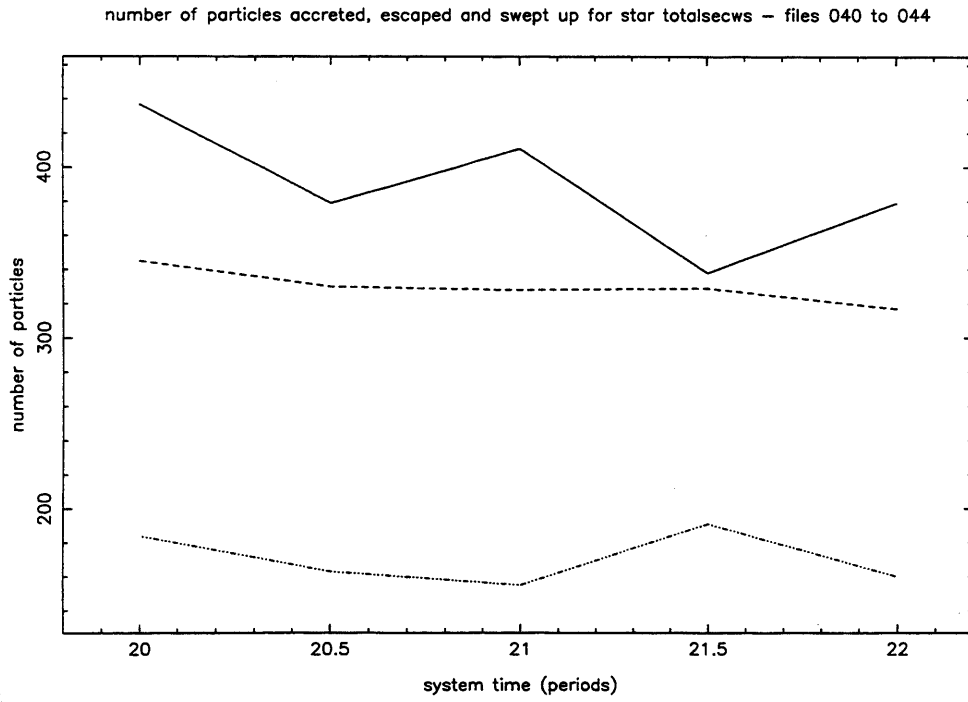

Figure 5.22: Plot of the number of particles accreted (solid), escaped (dashed) and swept up (dot-dashed) by the secondary for a synchronously locked pre-CV. The simulation used the revised force law, $v_{\mathrm{w}} = 10c_{\mathrm{s}}$, $k_{\mathrm{n}} = 880\ 000$ for the primary, $k_{\mathrm{n}} = 3$ for the secondary, and $r_{\mathrm{out}} = 1\ 000$.

simulations were modest in that the strength of the magnetic field did not enforce corotation of the wind material and the mass-loss rate required was reasonable. The mass loss in the wind could be reduced by coupling material more tightly to the field by increasing the strength of k.

Using these parameters in a binary configuration in section 5.1.2 appeared to leave the braking rate essentially unaffected for fixed parameters, answering the first of the three questions posed at the start of the chapter. This is not entirely surprising when we consider that the material is coupled to distances $r \gg a$. The motion of the secondary around the binary orbit is relatively inconsequential compared to the distance and relative velocities at large r. Material built up in a cloud of material about the binary through which the magnetic field was dragged, producing the braking torque.

In section 5.1.3 the timescale for the spindown of the WD in a CV due to the secondary's wind was calculated. This was in agreement with the estimate made from considering material to be coupled to large distances, if allowance is made for the weaker WD magnetic moment which was used in the simulation. This answers the second question posed earlier. The timescale is much shorter than that for the dissipation torque described in section 4.2 and may play an important role in bringing the WD towards synchronism. It almost certainly implies that the WD is unlikely, whatever its initial spin rate, to be rotating rapidly when the secondary comes into contact with its Roche lobe. The simulation did not include a secondary field. Including this would make the situation much more complex as the two time-varying forces cannot be considered independently. Firstly the two field vectors would have to be computed and added to find a total field vector. The motion of this fieldline would also have to be computed in order to calculate the relative velocity of the field and particle. The angular momentum calculation would also be complicated by the need to determine to which star each end of the fieldline was coupled.

These complexities are mitigated in the situation simulated in section 5.1.4. In a

polar configuration both the components are locked in synchronous rotation with the orbit. As a result any angular momentum loss by either component will be transmitted to the orbit. This means that we need not determine which star is losing angular momentum and driving the orbital braking as we can remove the angular momentum from the orbit directly. The simulations show that by adding a WD magnetic moment $\approx$ 6 times greater than that of the secondary, the timescale for magnetic braking has been reduced by a factor of $\approx$ 4.3. Rather than reducing the magnetic braking, the presence of the WD has enhanced it. Again, this can be understood by considering the behaviour at large r. For $r \gg a$ the resultant field will approximate that of two coincident dipoles. The strength of the total dipole will be the sum of two separate magnetic moments, remembering of course that they have been placed anti-parallel. The resultant field will thus be approximately $6 - 1 = 5$ times stronger than the secondary field on its own. The configuration considered was the most favourable for reduced magnetic braking to operate with the magnetic fields tending to oppose each other. This situation also increases the size of the regions of the secondary which connect to the primary. The simulations thus do not support the suggestion of reduced magnetic braking operating in polars; rather they support enhanced magnetic braking. The orientation derived by King, Frank & Whitehurst (1990) would result in the stellar fields tending to mutually reinforce each other and increase the magnetic braking rate still further for the same field strengths. This answers our third question.

The above conclusions have all been drawn assuming that the parameters which were successful in mimicking the braking rate of single stars are applicable to the binary case as well. The parameters themselves are certainly not unique, since we can trade off an increase of k against a decrease of $\dot{M}$. Given the current ignorance of the true $\dot{M}$ highlighted by the difference of 3 orders of magnitude derived from the same observations by Mullan *et al.* (1992) and Lim & White (1996), this is not a serious ambiguity. More subtly, however, it might be possible to perform simulations with a different behaviour for $k(\mathbf{r})$ (to be discussed below) or for a smaller r_{out}. The latter parameter has been derived conservatively assuming that the material can produce a torque on the binary out to the light cylinder. This is in contrast to the

Alfvén radius approach which decouples the material completely at r_A. The drag prescription can be used to mimic this approach, however, with a high value of k. It would be interesting to explore the same situations considered in this chapter using a constant, high value for k which dropped off sharply at an appropriately determined r_A. The effect of the magnetic geometry described by Wickramasinghe, Li & Wu (1996) in producing magnetic braking could then be examined self-consistently.

The simulations have assumed throughout that $k \propto B \propto r^{-3}$. If the diamagnetic treatment is valid and not a parameterisation of the problem we can derive the behaviour of $k(\mathbf{r})$ under different assumptions. We shall consider for simplicity only the radial dependence of k and assume that the blob mass and the inter-blob Alfvén speed is constant. From (2.1) we have

$$k \propto \frac{B^2 l^2}{m c_A} \tag{5.10}$$

If we assume that the material is in the form of 'solid' blobs that maintain their shape and identity then we can set

$$l = \text{const} \tag{5.11}$$

and derive

$$k \propto B^2 \propto r^{-6}. \tag{5.12}$$

If we assume the material behaves as if the blobs expand to fill the region of space into which they move, we can write

$$V \propto r^3 \tag{5.13}$$

$$\Rightarrow l \propto r. \tag{5.14}$$

Hence,

$$k \propto B^2 r^2 \propto r^{-4}. \tag{5.15}$$

Alternatively, if the blob is constrained by magnetic pressure, then equating the ram pressure to the magnetic pressure gives

$$\rho \propto B^2. \tag{5.16}$$

Since

$$l \propto \rho^{-\frac{1}{3}} \propto B^{-\frac{2}{3}} \qquad (5.17)$$

then

$$k \propto B^{-\frac{2}{3}} \propto r^{-2} \qquad (5.18)$$

Which of (5.12), (5.15) or (5.18) is correct is not clear although (5.18) would seem the most reasonable. The r^{-3} dependence used in the simulations is thus a compromise between a magnetically confined blob and an amorphous volume-filling blob. Initial experimentation with r^{-2} and r^{-3} dependencies for k showed little discernable difference in the character of the results, although the absolute values of k had to be chosen appropriately.

There are two main areas which it would be interesting to investigate further in the light of the results presented above. As mentioned earlier, investigations could be undertaken to examine the braking behaviour with a simulated Alfvén radius, particularly for the case of a polar. The drag approach with a weak k models the wind-field interaction with a fixed field shape and allows material to slip across the field. The Alfvén radius approach uses a fixed field shape and forces material to flow along the fieldlines. The true behaviour probably lies somewhere between these two extremes. The compromise used in chapter 3 which specified a fixed but distorted field shape which exerted a force on the material is not as useful in this situation. The more complex three dimensional geometry of the field is important when considering the wind. This complexity is increased by the addition of a second field to the problem and the distortion caused by the wind material to this shape is not clear. It would still be instructive, however, to carry out simulations which mimic the r_A prescription by using a high value of k over a suitably defined region.

Further development could investigate the possibility of ascribing the angular momentum losses of wind material to either component in a non-synchronous magnetic CV. These torques could be compared to those described in section 4.2. Conditions could then be derived for q, a and the magnetic moments of the stars which enable them to lock and form a polar. This offers the prospect of being able to describe

completely the spin and angular momentum evolution of a magnetic pre-CV into polar.

Chapter 6

Conclusions

We have seen that magnetic fields can have important effects in a variety of situations. In chapter 2 we saw how the drag model can reproduce the braking behaviour of YSOs. The coupling of the star to the disc used the dissipated rotational energy from the star to drive outflows with mass loss rates and velocities consistent with the observed molecular outflows. It would be interesting to examine the effect of replacing the localised magnetic loop with a global dipolar field. Such a field would be likely to brake the star similarly to the loop models but may well produce a different outflow behaviour due to the new field geometry.

In chapter 3 we examined two sets of simulations investigating the effect of the secondary's magnetic field of the behaviour of DN systems. A pure drag model produced much smaller discs with the secondary's field present, and confirmed the suggestion of Meyer-Hofmeister, Vogt & Meyer (1995) of a shortened recurrence time. More detailed models using HyDisc to simulate the system with a restricted MHD approach also produced shorter recurrence times. These simulations also produced eccentric accretion discs for systems above the period gap similar to those seen in SU UMa systems. The variability which would be produced by these eccentric discs enabled us to place limits on the magnetic moment of the secondaries in U Gem

and Z Cha. These results offer interesting observational challenges in detecting the possible lightcurve variations.

In chapter 4 we reviewed the evolution of CVs in general and in the particular case of those containing strongly magnetic WDs. In chapter 5 we examined simulations using a revised drag model which could reproduce the braking behaviour of the secondaries in cataclysmic variables deduced from observations. The same parameters were used to model the behaviour of a magnetic WD in a situation where it dominated the magnetic field of the secondary. The resultant braking of the WD in the secondary's wind occurred on a timescale shorter than that given by the dissipation torque. The same parameters were also used in examining the braking behaviour of synchronous (polar) systems. These systems actually lost angular momentum faster with the addition of a primary field. The simulations resulted in an enhancement of the braking rate even for the configuration where the stellar dipoles tended to oppose each other. Other orientations would increase the rate at which the angular momentum was lost from the orbit still further. These simulations can be improved upon. In particular it would be interesting to examine situations where material is forced to follow the magnetic fieldlines until it reaches the Alfvén radius. These simulations offer the prospect of being able to describe the angular momentum history of magnetic CVs by comparing the braking torques deduced in a variety of configurations with those described in chapter 4.

References

Aly, J. J. & Kuijpers, J., 1990. *A&A*, **227**, 473.

Ambartsumian, J. A., 1947. *Stellar Evolution and Astrophysics*, Erevan: Acad. Sci. Armen. SSR.

Applegate, J. H. & Patterson, J., 1987. *ApJ*, **322**, L99.

Balbus, S. A. & Hawley, J. F., 1992. *BAAS*, **181**, 7105.

Baliunas, S. L. & Vaughn, A. H., 1985. *Ann. Rev. Astr. Astrophys.*, **23**, 379.

Baliunas, S. L., 1990. In: *Formation and Evolution of Low Mass Stars*, 319, eds Dupree, A. K. & Lago, M. T., Kluwer Academic Publishers.

Basri, G. & Bertout, C., 1989. *ApJ*, **341**, 340.

Bastian, U., Finkenzeller, U., Jashek, C. & Jashek, M., 1983. *A&A*, **126**, 438.

Bence, S. & Padman, R., 1996. In: *Disks and Outflows Around Young Stars*, ed. Beckwith, S., Springer-Verlag. in press.

Bertout, C., 1989. *Ann. Rev. Astr. Astrophys.*, **27**, 351.

Bhattacharya, D. & Srinivasan, G. *X-ray Binaries*, chapter 12, 495. C.U.P., 1995.

Bianchini, A., 1990. *Astron. J.*, **99**, 1941.

Bodenheimer, P. *Star Formation in Stellar Systems*, chapter 1, p. 1. C.U.P., 1992.

Bouvier, J. & Bertout, C., 1989. *A&A*, **211**, 99.

Cameron, A. C. & Campbell, C. G., 1993. *A&A*, **274**, 309.

Campbell, C. G. & Papaloizou, J., 1983. *MNRAS*, **204**, 433.

Campbell, C. G., 1983. *MNRAS*, **205**, 1031.

Campbell, C. G., 1984. *MNRAS*, **211**, 83.

Campbell, C. G., 1985. *MNRAS*, **215**, 509.

Campbell, C. G., 1986a. *MNRAS*, **219**, 589.

Campbell, C. G., 1986b. *MNRAS*, **221**, 599.

Campbell, C. G., 1989. *MNRAS*, **236**, 475.

Cannizzo, J., 1993. In: *Accretion Disks in Compact Stellar Systems*, 6, ed. Wheeler, J. C., World Sci. Publ. Co., Singapore.

Czerny, M., 1986. *MNRAS*, **221**, 55p.

Dendy, R. O., 1990. *Plasma Dynamics*, O.U.P.

Dobrowolny, M. & Veltri, P., 1986. *A&A*, **167**, 179.

Drell, S. D., Foley, H. M. & Ruderman, M. A., 1965. *J. Geophys. Res.*, **70**, 3131.

Frank, J., King, A. R. & Lasota, J. P., 1988. *A&A*, **193**, 113.

Frank, J., King, A. R. & Raine, D. J., 1992. *Accretion Power in Astrophysics*, C.U.P., 2nd edition.

Goldstein, M. L. & Roberts, D. A., 1995. *Ann. Rev. Astr. Astrophys.*, **33**, 283.

Hameury, J. M., King, A. R., Lasota, J. P. & Ritter, H., 1988. *MNRAS*, **231**, 535.

Hameury, J. M., King, A. R. & Lasota, J. P., 1986. *MNRAS*, **218**, 695.

Hartigan, P., Edwards, S. & Ghandour, L., 1995. *ApJ*, **452**, 736.

Hawley, J. F. & Balbus, S. A., 1991. *ApJ*, **376**, 223.

Herbig, G. H., 1962. *Adv. Astron. Astrophys.*, **1**, 47.

Herbig, G. H., 1977. *ApJ*, **214**, 747.

Hirose, M. & Osaki, Y., 1990. *PASJ*, **42**, 135.

Horne, K. D. & Marsh, T. R., 1986. *MNRAS*, **218**, 761.

Joy, A. H., 1942. *PASP*, **54**, 15.

Joy, A. H., 1945. *ApJ*, **102**, 168.

Joy, A. H., 1949. *ApJ*, **110**, 424.

Kaitchuck, R. H., Sclegel, E. M., Honeycutt, R. K., Horne, K., Marsh, T. R., White II, J. C. & Masperger, C. S., 1994. *ApJS*, **93**, 519.

Kenyon, S., Hartmann, L., Strom, K. & Strom, S., 1990. *Astron. J.*, **99**, 869.

King, A. R. & Regev, O., 1994. *MNRAS*, **268**, 69p.

King, A. R., Frank, J. & Whitehurst, R., 1990. *MNRAS*, **244**, 731.

King, A. R., 1988. *QJRAS*, **29**, 1.

Kuijpers, J. & Pringle, J. E., 1982. *A&A*, **114**, L4.

Lada, C. J., 1985. *Ann. Rev. Astr. Astrophys.*, **23**, 267.

Lada, C. J., 1991. In: *The Physics of Star Formation and Early Stellar Evolution*, p. 329, eds Lada, C. J. & Kylaftis, N. D., Kluwer Academic Publishers.

Li, J., 1996. *Publ. Astron. Soc. Aust.*, **11**, 194.

Lim, J. & White, S. W., 1996. *ApJ*, **462**, L91.

Lovelace, R. V. E., Romanova, M. M. & Contopoulos, J., 1992. *ApJ*, **403**, 158.

Maceroni, C., Bianchini, A., Rodono, M., van't Veer, F. & Rio, R., 1990. *A&A*, **237**, 395.

Marcy, G. W., 1984. *ApJ*, **364**, 637.

Marsh, T. R., Horne, K., Schlegel, E. M., Honeycutt, R. K. & Kaithchuck, R. H., 1990. *ApJ*, **364**, 637.

Mayor, M. & Mermilliod, J.-C., 1991. In: *Angular Momentum Evolution of Young Stars*, 143, eds Catalano, S. & Stauffer, J. R., Kluwer Academic Publishers.

Mestel, L. & Spruit, H., 1987. *MNRAS*, **226**, 57.

Meyer, F. & Meyer-Hofmeister, E., 1981. *A&A*, **104**, L10.

Meyer-Hofmeister, E., Vogt, N. & Meyer, F., 1995. *A&A*, **310**, 519.

Mullan, D. L., Doyle, J. G., Redman, R. O. & Mathioudakis, M., 1992. *ApJ*, **397**, 225.

Mundt, R., Brugel, E. W. & Bührke, T., 1987. *ApJ*, **319**, 275.

Ottmann, R., 1994. *A&A*, **286**, L27.

Paczynski, B. E., 1971. *Ann. Rev. Astr. Astrophys.*, **9**, 183.

Pearson, K. J. & King, A. R., 1995. *MNRAS*, **276**, 1303.

Priest, E. R., 1982. *Solar Magnetohydrodynamics*, Kluwer Academic Publishers.

Pudritz, R. E. & Norman, C. A., 1986. *ApJ*, **301**, 571.

Ritter, H. & Kolb, U. *X-ray Binaries*, chapter 15, 578. C.U.P., 1995.

Shafter, A. W., Reinsch, K., Beuermann, K., Misselt, K. A., Buckley, D. A. H., Burwitz, V. & Schwope, A. D., 1995. *ApJ*, **443**, 319.

Shu, F. H., Adams, F. C. & Lizano, S., 1987. *Ann. Rev. Astr. Astrophys.*, **25**, 23.

Skumanich, A., 1972. *ApJ*, **171**, 565.

Smith, M. A., 1979. *PASP*, **91**, 737.

Soderblom, D. R., Stauffer, J. R., Macgregor, K. B. & Jones, B. F., 1993. *ApJ*, **409**, 624.

Stauffer, J. R. & Hartmann, L. W., 1987. *ApJ*, **318**, 337.

Steeghs, D., Horne, K., Marsh, T. R. & Donati, J. F., 1996. *MNRAS*, **281**, 626.

Strom, S. E., 1972. *PASP*, **84**, 745.

Theuns, T. & Jorissen, A., 1993. *MNRAS*, **265**, 946.

Tout, C. A. & Pringle, J. E., 1992a. *MNRAS*, **256**, 269.

Tout, C. A. & Pringle, J. E., 1992b. *MNRAS*, **259**, 604.

van Paradijs, J., 1986. *MNRAS*, **218**, 31p.

Verbunt, F. & Zwaan, C., 1981. *A&A*, **100**, L7.

Verbunt, F., 1984. *MNRAS*, **209**, 227.

Wang, Y.-M., 1996. *ApJ*, **465**, L111.

Wardle, M. & Königl, A., 1992. *ApJ*, **410**, 218.

Warner, B., 1995. *Cataclysmic Variable Stars*, C.U.P.

Whitehurst, R., 1987. *PhD thesis*, University of Oxford.

Whitehurst, R., 1988a. *MNRAS*, **232**, 35.

Whitehurst, R., 1988b. *MNRAS*, **233**, 529.

Wickramasinghe, D. T., Li, J. & Wu, K., 1996. *Publ. Astron. Soc. Aust.*, **13**, 81.

Wilking, B. A., Lada, C. J. & Young, E. T., 1989. *ApJ*, **340**, 823.

Wu, K., Wickramasinghe, D. T., Bailey, J. & Tennant, A. F., 1996. *Publ. Astron. Soc. Aust.*, **11**, 198.

Wynn, G. A. & King, A. R., 1995. *MNRAS*, **275**, 9.

Wynn, G. A., 1993. *PhD thesis*, University of Leicester, Leicester, England.